DEVELOPMENT, DESIGN, AND CONSTRUCTION OF A HUMAN-BUILDING INTERACTIONS LABORATORY

by

Sourabh D. Yadav

A Thesis

Submitted to the Faculty of Purdue University

In Partial Fulfillment of the Requirements for the degree of

Master of Science in Mechanical Engineering

School of Mechanical Engineering

West Lafayette, Indiana

May 2022

THE PURDUE UNIVERSITY GRADUATE SCHOOL
STATEMENT OF COMMITTEE APPROVAL

Dr. James E. Braun, Co-Chair

School of Mechanical Engineering

Dr. Davide Ziviani, Co-Chair

School of Mechanical Engineering

Dr. William Travis Horton

School of Civil Engineering

Dr. Panagiota Karava

School of Civil Engineering

Approved by:

Dr. Nicole Key

Dedicated to my friends, family, my teachers and loved ones

ACKNOWLEDGMENTS

A venture such as this is ostensibly credited to a single individual, but behind this individual stand mentors, peers, friends, and family, without anyone of whom the undertaking would only be half the experience it can be. I am immensely indebted to my co-advisors, Dr. James E. Braun, and Dr. Davide Ziviani, for their patient guidance throughout my program, for readily providing their expertise whenever needed, and for their valuable feedback in preparing this document. I thank Prof. Travis Horton and Prof. Panagiota Karava for serving on my committee and their constant guidance and support as fellow PIs of this project. To Parveen Dhillon, who provided the source code of his initial models, which helped me make significant early headway, followed by continuous mentoring in LabVIEW, EES, prototype testing, and all the intricate tasks of this project, I express my immense gratitude. I am deeply grateful to Dr. Orkan Kurtulus for his constant support and mentoring during experimental testing and modeling. I am also very grateful to Feng Wu for assisting me in research and testing, specifically on the side of the controls, and Sarah Alkandari for assisting and taking over the project installation. I thank the Herrick shop staff-Frank Lee, Charles Baxter, Jose Romero, Dean Smoll, and Rob Hubert, for all their assistance with the experimentation on the test setup and HBIL hydronic system installation and for their generous camaraderie. I would also like to thank Dr. Eckhard Groll, Dr. Davide Ziviani, and Dr. Vatsal Shah for trusting me with the opportunity to start at Herrick Labs as an independent study student in Fall 2019. Without this, I would not have had the opportunity to further work at Herrick Labs and on this project. Also, the staff, present, and past, of Herrick Laboratories – Cindy, Robin, Sarah, Maralee, Dr. Rhoads- thank you for all the tangible and intangible ways you have helped me with my work here at Herrick Laboratories. Finally, I would like to thank my parents, my sister, and my close friends, both here and back in India, for being there whenever needed, and supporting me in all possible ways.

TABLE OF CONTENTS

LIST OF TABLES

LIST OF FIGURES

NOMENCLATURE

Symbols

T	Temperature (K)
R	Thermal resistance (K/W)
R_C	Thermal contact resistance (K-m^2/W)
C	Thermal capacitance (J/kg-K)
$\dot{Q}_{loss}$	Heat transfer rate between heat spreader panel and outdoor air through insulation (W)
$\dot{Q}_{in}$	Heat transfer rate between water and heat spreader panel through copper tubes (W)
$\dot{Q}_{front}$	Heat transfer rate between heat spreader panel and the interior surface (W)
$\dot{Q}_{edge}$	Heat transfer rate between support panel and indoor air (W)
A	Surface area of panel (m^2)
$\dot{m}_w$	Mass flow rate of water (kg s^{-1})
C_{pw}	Specific heat capacity of water (J/kg-K)
D_i	Tube internal diameter (m)
q'_u	Heat rate per unit length of the tube (W/m)
C_b	Bond conductance (W/m-K)
h_{fi}	water-to-tube inside wall heat transfer coefficient (W/m^2-K)
h_c	Surface-to-indoor convective heat transfer coefficient (W/m^2-K)
h_r	Surface-to-indoor radiative heat transfer coefficient (W/m^2-K)
h_{edge}	Panel edge to indoor combined (radiative+convective) heat transfer coefficient (W/m^2-K)
A_{edge}	Surface area of panel frame (m^2)
ΔT	The difference in water inlet and outlet temperature (K)
ε_{Gp}	Emissivity for gypsum surface (-)
σ	Stefan-Boltzmann constant (W/m^2 K^4)
Et	End time of performance test (minutes)
$T_{W\,in}$	Water inlet temperature (K)
$T_{W\,out}$	Water outlet temperature (K)
$Error_{SS}$	Steady State Error (°C)
$Error_{TR}$	Transient Error (°C)
MAE	Mean Absolute Error (°C)
PD	Pressure drop (psi)
EQL	Equivalent length (m)
$P_{loss\,factor}$	Pressure drop per unit length of pipe in ft of water (ft-H2O)
ΔP	Differential pressure (psi)
Cv	Valve/Fitting flow coefficient (-)
N	Number of fittings (-)
h_f	Fluid heat loss (ft)
f	Darcy-Weisbach friction factor (-)
L	Length of pipe (ft)

g	Gravitational acceleration constant (ft s^{-2})
Re	Reynolds number (-)
Ra_L	Rayleigh number (-)
Nu	Nusselt number (-)
ν	Kinematic viscosity of water ($m^2 s^{-1}$)
V	Velocity of water (ft s^{-1})
e	Absolute roughness of pipe (mm)
D	Diameter of pipe (ft)
L'	Length of vertical plate (m)
β	Volumetric thermal expansion coefficient (1/K)
α	Thermal diffusivity ($m^2 s^{-1}$)
k	Thermal conductivity (W/m-K)

Subscripts

Pn	Heat Spreader Panel
Al	Aluminum Back Panel
Sp	Support Panel
Gp	Gypsum Panel
Ins	Insulation Panel
W	Water
ID	Indoor Air
OD	Outdoor Air
Edge	Panel Frame/Edge
Surface	Panel Surface
SS	Steady State
TR	Transient

ABSTRACT

The evolution of existing building construction is envisioned as modular construction. Instead of on-site construction, buildings can be assembled on-site using prefabricated modular elements. These modular elements could integrate intelligent building technologies to enable autonomous, occupant responsive, scalable, cost-effective, and sustainable features. On-site assembly of modular construction elements would offer better quality control, decrease material waste and resources, with more predictable schedules. These building elements would allow more cost-effective integration of new intelligent sensors, adaptive interfaces, renewable energy and energy recovery technologies, comfort delivery, and resiliency technologies, making high-performance buildings more affordable. To explore and evaluate these modular and intelligent comfort delivery concepts and advanced approaches for interaction with occupants, a new Human-Building Interactions Laboratory (HBIL) has been designed and is under development. The facility has a modular construction layout with thermally active panels, and the interior surface temperature of each panel can be individually controlled using a hydronic system. Such configuration allows us to emulate different climate zones and building type conditions and perform studies such as the effect of different kinds of active building surfaces on thermal comfort, localized comfort delivery, and occupant comfort control. Moreover, each panel is reconfigurable to investigate different interior surface treatments for thermal, visual, and acoustic comfort conditions. In this MS thesis work, the overall design approach of the facility is presented. Development, experimental investigation of thermal performance, and aligned design modifications of a prototype thermo-active wall panel are explained in detail. Detailed development of a 1-D transient numerical model for the prototype wall panel and its tuning and validation are also presented. Furthermore, the design and installation plan of the hydronic system for the HBIL facility are also presented with an initial commissioning plan.

1. INTRODUCTION

1.1 Background and Motivation

The development of the HBIL was motivated by a desire to investigate advanced building concepts that address sustainability, modularity, and embedded intelligence. As per U.N. Environment Program Global Alliance for Buildings and Construction, (2020), the building and construction sectors are responsible for the largest proportion of both final (end-use) energy use (36%) and energy-related CO_2 emissions (39%). The development of high-performance equipment embedded in modular building elements with the desire to improve upon the existing approach of typical building construction is one of the prime driving factors for this research work. On-site construction is currently the most common approach to build residential and commercial buildings. A typical residential building takes approximately 7-8 months to be constructed according to the survey conducted by U.S. Census Bureau in the year 2018 and can lead to a significant waste of material. Hence, the modular construction approach is envisioned as the future of building construction. Modular construction has shown to facilitate reduction in material waste, construction time and other resources along with improving the quality of construction. In addition, modular construction could enable cost-effective integration of intelligence throughout the building that includes advanced occupant interfaces. The current state of the art involves IoT-based intelligent building automation systems where occupants play a minor role. Most commonly used IoT-based home automation systems involve smart voice assistants like Google Home and Amazon Alexa that connect smart devices with the cloud. For example, smart thermostats are connected to cloud servers, and users can control these using their smart devices (Hu, 2021). However, Lassen et al., (2021) argued that although today's high-performance buildings are technologically complex and automated, users are not invited to interact with buildings in fear of disturbing automation setpoints, and as a result of this, these buildings do not meet their design goals in terms of energy performance, occupant satisfaction, and maintenance.

In the future, it is envisioned that high-performance buildings will feature modular construction with intelligent, localized, and energy-efficient comfort delivery systems that will allow advanced human-building interactions. However, before these innovative building technologies are implemented in the field, they need to be engineered and evaluated both from technology and

occupant perception points of view. Radiant heating and cooling systems are one of the possible ways to provide local thermal comfort with modular wall or floor elements and thermo-active surfaces.

Rhee & Kim, (2015) reviewed developments in radiant heating and cooling systems over the past fifty years and suggested future research areas to improve these technologies. These include designing a system that can provide heating, cooling with multi-zone control, developing practical and straightforward technology to sense surface temperatures, optimizing hydronic equipment for radiant systems, and integrating radiant systems with building envelopes. The concept of a Human-Building Interactions Laboratory (HBIL) with thermo-active wall panels was conceived to study modular construction, localized thermal comfort delivery, development of radiant heating and cooling systems with multi-zone control, application of intelligent sensors and advanced control approaches, and different novel comfort delivery technologies embedded in walls such as micro heat pump systems, thermoelectric devices, among others. Figure 1.1 illustrates the HBIL concept where an occupant inside a space equipped with thermally active panels communicates with an integrated intelligent voice assistant for control. The occupant provides a command stating that they are feeling hot. In turn, the voice assistant sends a command to the controller to provide localized space cooling around the occupant with thermo-active panels to provide the desired thermal environment.

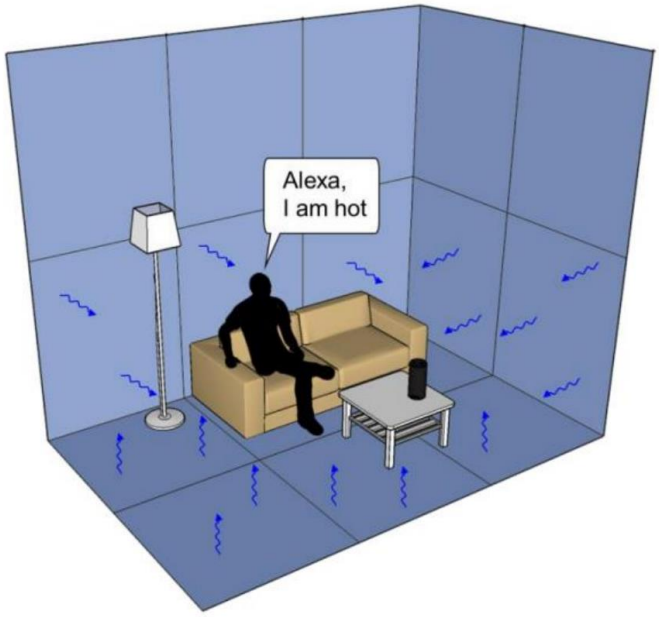

Figure 1.1 HBIL concept-localized comfort delivery with voice control

1.2 Literature Review

An extensive literature review was conducted to understand the current state-of-the-art in modular construction, high-performance building technology, and radiant heating and cooling systems. This section discusses some of the relevant literature directly pertinent to this dissertation and aims at identifying research gaps and new research directions.

Ferdous et al., (2019) performed a critical review of modular buildings, including recent advancements, mechanical performance, and future directions. The review stated that modular construction is gaining popularity in Australia and China and is used in other countries such as the UK and USA. Based on their study, employing modular construction techniques can reduce material usage and waste, transport activities, noise and disruption, accidents, safety hazards, and even equivalent carbon emissions. Prefabricated components demonstrated satisfactory performance under the static, dynamic impact, cyclic, seismic, blast, fire, and sustained loading conditions. Nevertheless, despite these positive attributes, the growth of modular construction is slower than anticipated, mainly due to the lack of logistical support. Development of design guidelines, training workers, and increasing interest of investors will help unlock the potential growth of prefabricated modular buildings. In addition, composite materials have emerged as alternatives to conventional building materials that may further improve overall cost-effectiveness through reduced maintenance and longer life.

Abdelmageed & Zayed, (2020) studied the literature related to "Modular integrated Construction" (MiC) in detail and presented some future directions for research in this area. MiC is a method of construction that involves prefabricated, 3-D volumetric fully finished modules that are built off-site and transported and installed on-site. The study identified the lack of quantitative analysis to assess the benefits of various innovative design proposals as a gap in MiC research. Testing innovative MiC building design ideas in large-scale applications and actual trials with new construction materials are some of the future directions that this study provides.

Additive manufacturing is another emerging technology in building construction and has the potential to revolutionize the construction industry. Bhardwaj et al., (2019) reviewed additive manufacturing processes for infrastructure construction. Authors envisioned that the applications of additive manufacturing processes in infrastructure construction could bring in significant developments in various aspects like productivity, quality, and safety. This study reviewed various existing additive manufacturing techniques and presents process specific gaps. For example,

material extrusion which is a most common type of additive manufacturing process is shown to require significant studies in material characteristics, composition, etc. Other additional gaps presented include creating new materials, improving process knowledge, and developing standards to system level integration, and rethinking the building design approach to incorporate functionality and performance into the structural design of buildings. On the same lines, Delgado Camacho et al., (2018) also reviewed applications of additive manufacturing in construction industry. The study claims that based on literature, additive manufacturing technologies have the potential to decrease labor cost, reduce material waste and create customized complex geometries with precise dimensions based on design drawings which is important for modular construction.

An experimental study performed by Li et al., (2021) involved the evaluation of an indoor thermal environment with modular radiant wall panels for heating in low-energy buildings. Figure 1.2 shows the size, orientation of the room, location of panels, and the points at which the temperature was measured. Six tests were conducted with different installation positions summarized in Table 1.1. The authors stated that the modularity scheme provided critical practical advantages, such as less material and capacity requirements, improved indoor space design and flexibility, and convenient installation. They found that their radiant heating system could satisfy the heating demand by meeting required thermal comfort standards as presented in Figure 1.3, but the overall application still needed optimization. Most importantly, they concluded that the performance of a similar modular system for radiant cooling needs to be explored and evaluated, especially considering hot and humid conditions during the summer season.

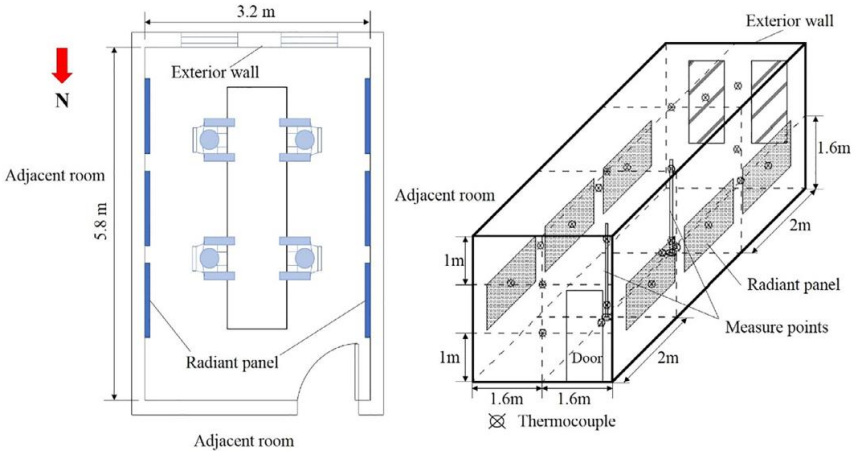

Figure 1.2 (Li et al., 2021) Experimental room for evaluation of an indoor thermal environment with modular radiant wall panels for heating in low-energy buildings, showing the location of radiant heating panels inside the space, their height from the ground, the type of wall (exterior or interior) and thermocouple locations that were measuring points in the room

Table 1.1 (Li et al., 2021) in the experimental study for evaluation of an indoor thermal environment with modular radiant wall panels for heating in low-energy buildings, showing siz types of tests conducted which had different radiant module area and corresponding location of the module in the room and its height from the floor level

Test	Area of the radiant module (m^2)	Installed position
1	1.5 (single module)	0 m above the floor and in the middle of the wall
2	1.5 (single module)	1 m above the floor and in the middle of the wall
3	3 (two modules)	0 m above the floor and close to the external wall
4	3 (two modules)	0 m above the floor and close to the door
5	3 (two modules)	0 m above the floor and in the middle of the wall
6	3 (two modules)	1 m above the floor and in the middle of the wall

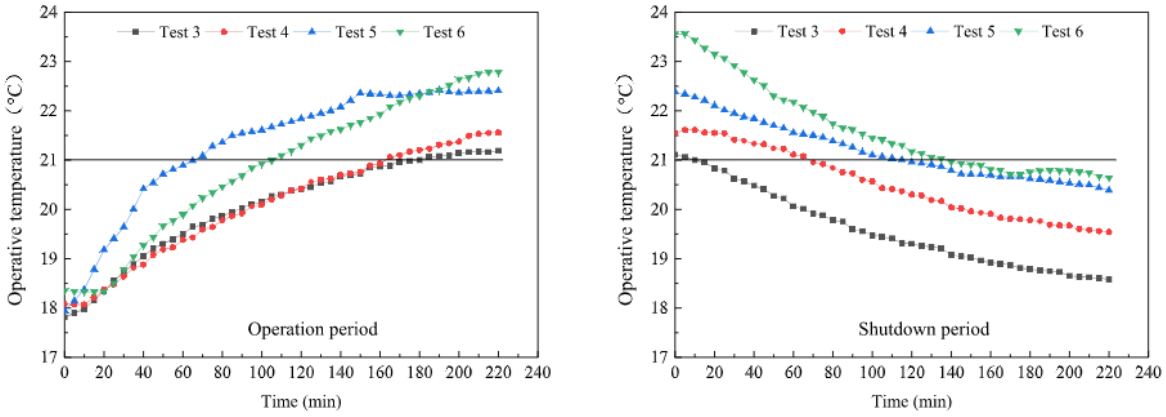

Figure 1.3 (Li et al., 2021) Experimental results-indoor operative temperature vs. time in the experimental study for evaluation of an indoor thermal environment with modular radiant wall panels for heating in low-energy buildings. Plots show that the panels can achieve the required operative temperature in heating mode

According to the U.S. Energy Information Administration, (2021) report on energy efficiency trends in residential and commercial buildings, buildings account for more than 40% of primary energy use in the US. The U.S. Energy Information Administration (EIA), (2020) report predicts that by 2050, the delivered energy for air-conditioning in the building sector will increase more than any other sector, while energy consumption for space heating will decline. However, the total primary energy consumption by the buildings sector is predicted to increase by 7% by the year 2050. High-performance building designs have started becoming more crucial. The Energy Policy Act of 2005, (2005) stated that a high-performance building has attributes that include energy efficiency, durability, life-cycle performance, and occupant productivity. Brager & Arens, (2015) presented various aspects of developing high-performance buildings focusing on lower energy requirements

and better comfort delivery. They claimed that strategies such as natural ventilation and personal comfort systems (PCS) have improved indoor environmental quality and occupant satisfaction and are sustainable strategies with energy-saving potential.

Esrafilian-Najafabadi & Haghighat, (2021) reviewed occupancy-based HVAC control systems in buildings. One of their key recommendations was to employ or develop different testbeds rather than existing research offices and residential buildings to evaluate occupancy-based control systems. That is because testbeds offer the flexibility to emulate a variety of spaces, in addition to just offices and residential environments. Localized thermal comfort delivery, also categorized as Personal Comfort Systems (PCS), is another promising area of research in high-performance buildings. PCS aims to condition occupied zones in the space as per the occupant's interest while maintaining the rest of the space at relatively under-conditioned or standard setpoints. PCS is claimed to have many benefits over conventional HVAC systems, for example, improved productivity and health, potential energy savings (Godithi et al., 2019), and relatively greater satisfaction due to the rapid adjustment of the local indoor environment offered by personalized control (Kim et al., 2019). Based on these benefits, Rawal et al., (2020) studied the comfort, energy, and economics of PCS. One of their key avenues that could be researched included a study of PCS devices that utilize radiative and conductive modes and their combination as the mode of heat transfer. Based on this, it is clear that there is a lack of study with radiant heating and cooling systems in high-performance buildings in terms of occupant control and personalized comfort delivery.

Radiant systems are perceived differently as compared to air-based systems. Hence, thermal comfort standards for radiant systems are different. Halawa et al., (2014) studied the impact of thermal radiation fields on thermal comfort, control strategies, and energy consumption in buildings. They argued that the average radiant temperature (often assumed to be equal to the room air temperature) and the radiant asymmetry due to the thermal radiant field are essential parameters in evaluating thermal comfort. The literature states that existing thermal comfort standards do not adequately address the issues resulting from thermal radiation fields, and more work is needed to better understand, quantify, and evaluate these parameters. Although energy-saving and comfort delivery potentials of radiant systems have been demonstrated, further work needs to be carried out in terms of system design, configuration, and control.

Karmann et al., (2017) performed a critical literature review to assess if radiant systems (mainly for cooling purposes) provided better, equal, or lower thermal comfort than all-air systems.

They mainly focused on comparative studies rather than studies that focused on either radiant or all-air systems alone. As shown in Table 1.2, three out of eight reviewed studies showed thermal comfort preferences for radiant over force-air systems, whereas the remaining five concluded there was no preference. Although there is suggestive evidence that radiant systems may provide equal or better thermal comfort than all-air systems, authors argued that further studies are needed to confirm this.

Table 1.2 (Karmann et al., 2017) Summary of literature review from eight different studies comparing thermal comfort preferences for radiant vs. all-air systems, showing preference towards radiant systems

Publication	Method	Cond. mode	Radiant system	Convective (all-air) systems	Preferred system
Niu and Kooi [55]	BPS	Cooling	Radiant ceiling panels with DV	DV, ceiling "air panels"	No preference found
Olesen et al. [64]	Lab testing (measurements)	Heating	Radiant ceiling, radiant floor	Convectors, Mixing ventilation (air supplied from the top and down nearby the façade)	No preference found
Kulpmann [65]	Lab testing (measurements)	Cooling	Radiant ceiling panels with DV	DV	Radiant
Mustakallio et al. [69]	Lab testing (measurements)	Cooling	Radiant ceiling panels with chilled beams	Mixing ventilation, chilled beams	No preference found
Schellen et al. [76]	Lab/Human subject testing	Cooling	Radiant ceiling panels with mixing	Mixing ventilation	No preference found
Schellen et al. [75]	Lab/Human subject testing	Cooling	Radiant ceiling panels with DV and mixing ventilation	Mixing ventilation, DV (multiple conditioning strategies)	No preference found
Imanari et al. [47]	Occupant surveys	Heating and cooling	Radiant ceiling panels combined with mixing ventilation	Mixing ventilation	Radiant
Sastry and Rumsey [77]	Physical measurements and occupant surveys	Cooling	TABS	Mixing ventilation	Radiant

Dawe, (2019), based on their field evaluation of LEED-certified buildings with radiant systems, presented slightly contrasting results. Post-occupancy assessment of occupant satisfaction and energy performance indicated that both radiant and all-air spaces had similar overall indoor environmental quality and acoustic satisfaction but that the radiant systems had higher thermal satisfaction. The critical factors for temperature discomfort were lack of control over temperature, air movement, and slower response time due to higher thermal mass. An optimum radiant design or control scheme that maximized thermal comfort was not found. Future study recommendations included developing strategies to improve acoustic satisfaction in radiant buildings and high thermal mass radiant systems that can be resilient against uncertain weather conditions.

Fabrizio et al., (2012) did a numerical comparison study of energy performance and comfort of radiant heating and cooling systems with respect to air systems. The radiant systems coupled with a suitable primary energy system (e.g., heat pumps) to provide heating/cooling water reduced predicted energy costs and carbon dioxide emissions. Similarly, a study conducted by Higgins & Carbonnier, (2017) assessed the real-world energy usage of buildings with radiant heating and cooling compared to standard benchmarks for building energy performance. Forced-air systems are predominant in the US. However, designers striving for low energy and green building outcomes

prefer radiant systems. Additionally, radiant systems were selected by 74% of the buildings that were targeting the highest levels of LEED certifications.

Rhee et al., (2017) studied radiant heating and cooling systems and addressed a range of questions about these systems, starting from their definition and standards to their controls and challenges. They provided evidence in the form of both simulation and field test results to show that radiant systems with dedicated outdoor air systems perform better than conventional forced-air systems in terms of energy performance and thermal comfort. Developing improved designs and control methods for radiant systems that serve both heating and cooling; implementation of advanced control strategies into multi-zone control; and optimization of hydronic network systems in terms of pressure, flow rate, and pumping energy are the key points that were presented as research gaps in this study.

Zhang et al., (2020) performed a systematic review of integrated systems with a radiant heating or cooling system (on either ceiling or floor) coupled with different ventilation approaches. The system performances were evaluated based on thermal comfort and indoor air quality. One of the key findings was that radiant floor or ceiling systems coupled with displacement ventilation do not behave similarly to forced air systems in terms of temperature stratification and indoor air quality. However, the impact of mixing flow pattern ventilation is relatively less significant when coupled with radiant systems. Because of intensive interactions between the two sub-systems (radiant and ventilation), achieving thermal comfort and air quality was found to be challenging. Moisture condensation is also another risk that was highlighted, especially if there is stratification, improper or low mixing of indoor air. Future recommendations include studies that consider energy performance, convective and radiative heat transfer processes, control strategies, and renewable energy applications. Also, the interaction of systems providing radiant heating or cooling through walls and different ventilation modes remains a research gap.

A wide range of publications in modular construction, high-performance buildings, occupant-building interaction, personal comfort systems, and radiant heating and cooling systems were reviewed. From the literature review, the following key points can be derived:

- Modular construction is a promising approach for high-performance buildings.
- Personal comfort delivery systems and occupant-building interactions can make high-performance buildings more energy-efficient and sustainable.

- Radiant heating and cooling systems are common in high-performance buildings and have a good potential of achieving improved thermal comfort with energy savings if coupled with DOAS.
- A few studies showed that radiant and all-air systems had equal performance when evaluated for occupant satisfaction and energy use but needed optimization in terms of operation and control.
- Work needs to be done to design radiant heating and cooling systems with optimum ventilation systems to handle the latent loads and indoor air contaminants.
- There is a lack of occupant perception studies with personalized thermal comfort via radiant systems.
- Additional work is needed to develop systems capable of providing heating and cooling with multi-zone control and optimized hydronic networks.

1.3 Thesis Goals and Approach

To be able to experimentally study many of the identified research gaps in the future, the overarching goal of the work described in this thesis was to develop a Human Building Interactions Laboratory (HBIL) capable of providing localized thermal comfort delivery using thermo-active panels for walls, floor, and ceiling. The facility is a reconfigurable test space designed to evaluate the feasibility of the 'modular buildings' concept with local thermal comfort control via occupant interaction using smart voice assistants. The thesis work included the design, construction, and performance assessment of prototype thermo-active panels for delivering localized radiant heating and cooling. Different approaches for controlling the panel interior surface temperature were evaluated. A decision was made to employ hydronic loops and to control the water temperature with mixing valves. During the design phase, a transient numerical heat transfer model of a single panel was developed, tuned, and validated using experimental results and was used as a reference for selecting final interior panels. The manufacturing of modular-thermo-active panels for the facility was outsourced to a third-party company specializing in modular construction. The design of the HBIL facility with all the panels and provision for ventilation and lighting, among others, was finalized after multiple iterations. A hot and cold water hydronic system was designed to control heating and cooling for all the panels within the HBIL facility. The thesis includes all details of the facility design along with plans for commissioning.

1.4 Thesis Organization

The thesis is organized in 5 chapters. Chapter 1 provides an overview of the background and motivation of this study along with a comprehensive literature review and outlines the main objectives of the study. Chapter 2 presents goals and target specifications for the HBIL, followed by a detailed review of different design approaches that were investigated for thermo-active panel surface temperature control. It ends with an overview of the HBIL facility design.

Chapter 3 includes details about the prototype panel design, performance assessment tests, and modifications involved. It also presents the numerical modeling details and its validation and compares the test and model results. Furthermore, it covers the final thermo-active panel design with testing results based on the initial design and model.

In Chapter 4, the final HBIL envelope construction and installation details are presented. It also includes the design and installation descriptions of the hot and cold water hydronic system for the HBIL facility. This chapter includes initial commissioning plans to demonstrate simple heating and cooling of the facility.

Chapter 5 provides a summary of the work, lessons learned, an overview of possible experiments that this facility can support, and some tests planned for the immediate future.

The appendix includes the steady-state and transient model EES (Klein, 2021) code, and pressure drop calculation results.

2. OVERVIEW OF HBIL FACILITY DEVELOPMENT AND DESIGN

2.1 Overview of HBIL Facility Goals and Target Specifications

The HBIL is a reconfigurable test space designed to facilitate laboratory research for residential and commercial buildings. The envisioned overall dimensions are 6.1m × 3.65m × 3.04m (20' × 12' × 10') (length x width x height). The main research goals for the application of the HBIL facility are to study:

- human interactions with new smart technologies, such as smart thermostats, home energy management systems, and visual and voice interaction systems;
- impacts of local radiant cooling/heating comfort delivery on human comfort and energy usage;
- innovative and modular comfort delivery systems for buildings, such as new heating/cooling devices (e.g., micro heat pumps) that are embedded in walls and new approaches for controlling local comfort delivery.

The fundamental elements of the HBIL are a series of thermo-active panels with radiant heating or cooling capabilities. The target surface temperature range was one of the first design choices to make. To this end, the U.S. DOE reference small-office building model (Deru et al., 2011) was used to simulate energy flows for typical year-round weather conditions in Chicago, IL. The simulation results are shown in Figure 2.1. Based on the findings and practical experience of the investigators, it was decided that a surface temperature range between 15.5°C and 26.7°C (60°F to 80°F) of the internal wall surface was suitable to ensure sufficient flexibility in conducting research in the HBIL.

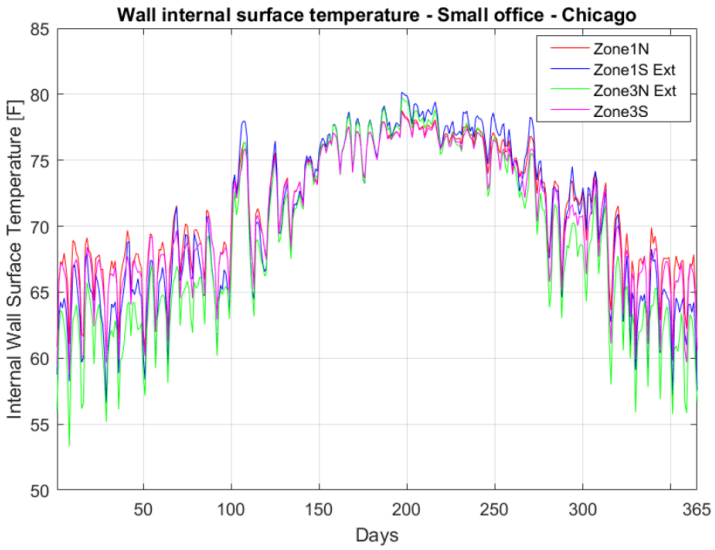

Figure 2.1 Internal wall surface temperature variation (EnergyPlus simulation)

With the thermo-active panels, the HBIL will enable the evaluation of localized thermal comfort and will help generate initial data on occupant interactions with modular comfort delivery systems using novel visual and audio interfaces. The HBIL will be able to emulate conditions for one or two exterior walls with a glazing area on one wall to enable a realistic representation of a house or a perimeter office space. The HBIL is designed so that it will allow individual control of the interior surface temperature of each panel. This design will facilitate studies of the effects of surface temperature on thermal comfort, localized occupant comfort control, among others. As mentioned earlier, the reconfigurable design will allow the testing of interior surface treatment panels with different materials and their occupant perception in terms of thermal, acoustic, and visual comfort. In addition, the facility will also have air comfort delivery capabilities to tackle latent loads, as illustrated in Figure 1.1 in Section 1.1. The facility was constructed by Bridgewater Studio that specializes in modular construction.

2.2 Investigation of Design Approaches for Panel Surface Temperature Control

Four different system design approaches were investigated to control panel surface temperature for heating and cooling in a temperature range between 15.5°C and 26.7°C (60°F to 80°F). Each approach was evaluated based on its potential to provide both heating and cooling to satisfy the design conditions, ease of individual panel temperature control, and overall cost.

2.2.1 Thermoelectric based system

Since a surface temperature control system is required to have both heating and cooling capabilities, the first system considered was based on utilizing thermoelectric modules. Figure 2.2 shows a sample module and its assembly with fins. Thermoelectric modules could be embedded into the test room wall surfaces, floor, and ceiling. Each module could be controlled as a simple small variable heat pump providing heating and cooling based on a DC voltage input signal amplitude and polarity. Figure 2.3 shows a representative thermoelectric module integrated into the test room wall.

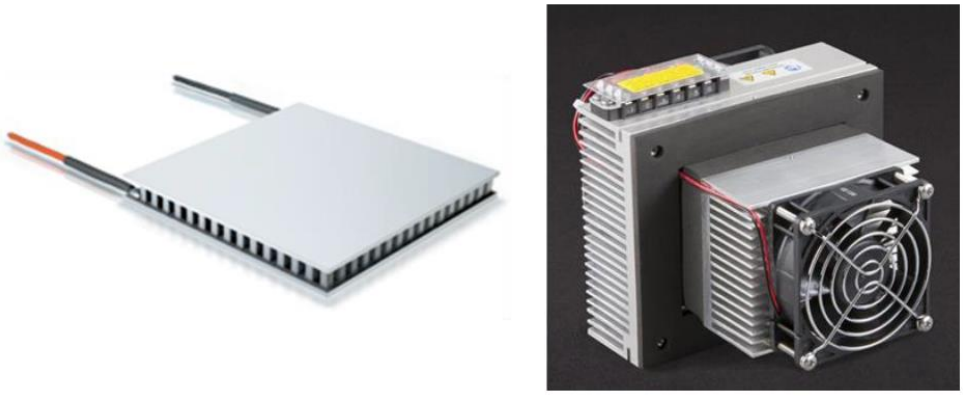

Figure 2.2 Thermoelectric module and assembly for heating and cooling

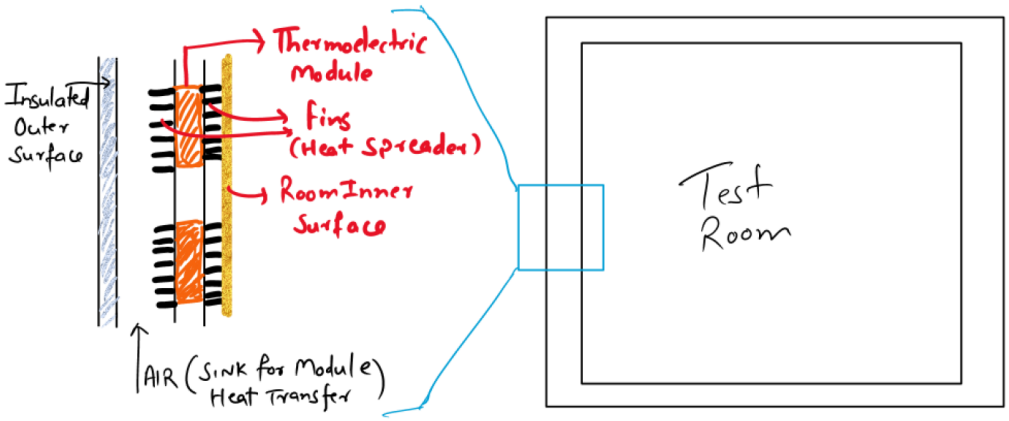

Figure 2.3 Approach 1-Thermoelectric module assembly in test room wall

Based on the load estimation and surface area requirements, an estimate of the required number of thermoelectric modules and cost was determined for two different possible layouts of thermoelectric modules in the wall. The first layout is a case where the entire interior surface area is covered with thermoelectric modules. The second layout spreads the modules uniformly over the

internal surface, with some reasonable spacing between the modules, and uses a heat spreader to maintain a relatively constant temperature over the wall surface.

Although the thermoelectric modules can easily satisfy the required heat flux specifications and the capability to heat and cool the surfaces, the costs were found to be prohibitively expensive because of the small sizes of the currently available modules in the market and a large number of required modules. Also, controlling these individual modules within the required accuracy to maintain constant wall surface temperatures would require more hardware (e.g., controller, wiring, sensors) and software capabilities, further increasing the cost. Therefore, it was decided not to use thermoelectric modules for this application.

2.2.2 Air cooling and electric heating element-based system

An alternative approach investigated for controlling the wall surface temperatures was to provide heating using an electric heating element and cooling using cold air that is supplied from the building conditioning system, such as an air handing unit (AHU) at about 55°F. Figure 2.4 shows the construction layout of a wall using this air-based concept. An air velocity of 1 ms^{-1} was chosen since higher values could cause excessive noise in the test room, affecting comfort research studies.

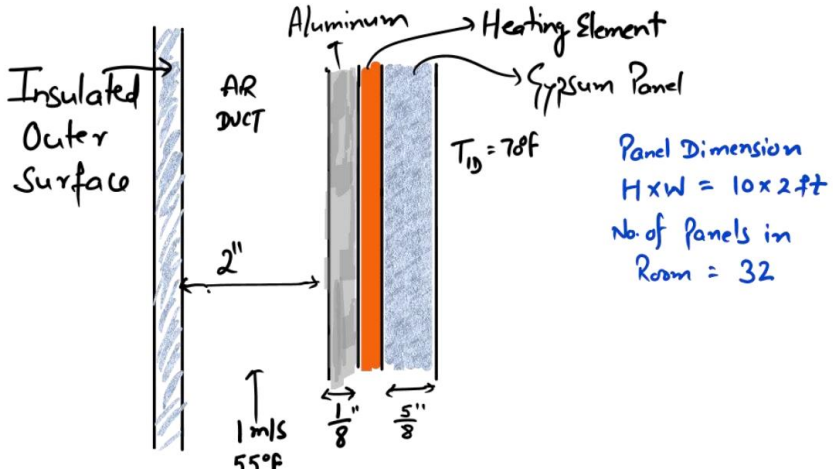

Figure 2.4 Approach 2-Air cooling and electric heating element-based system layout

To study the steady-state and transient behaviors of the air-based concept under cooling conditions, a finite volume model of the wall was constructed with the following simple assumptions.

- Indoor Air Temperature = 70°F
- Target Interior Surface Temperature = 60°F

- Velocity of Supply Air = 1 ms^{-1}
- Negligible vertical conduction, contact resistance, and air node capacitance.

Steady-state analysis was performed to check whether the forced air system concept could maintain the wall temperature by assuming that the heater was off. Based on simulation results of Figure 2.5, the outside duct airflow at the given air inlet temperature ($T_{o,air}$) of 55°F and 1 ms^{-1} was not enough to maintain the internal surface temperature ($T_{gypsum,5}$) at 60°F. This can be achieved by increasing the air velocity, but as mentioned before, that could lead to noise issues. Therefore, another alternative was to use chilled water instead of air as a cooling medium, which is discussed in the following sub-section.

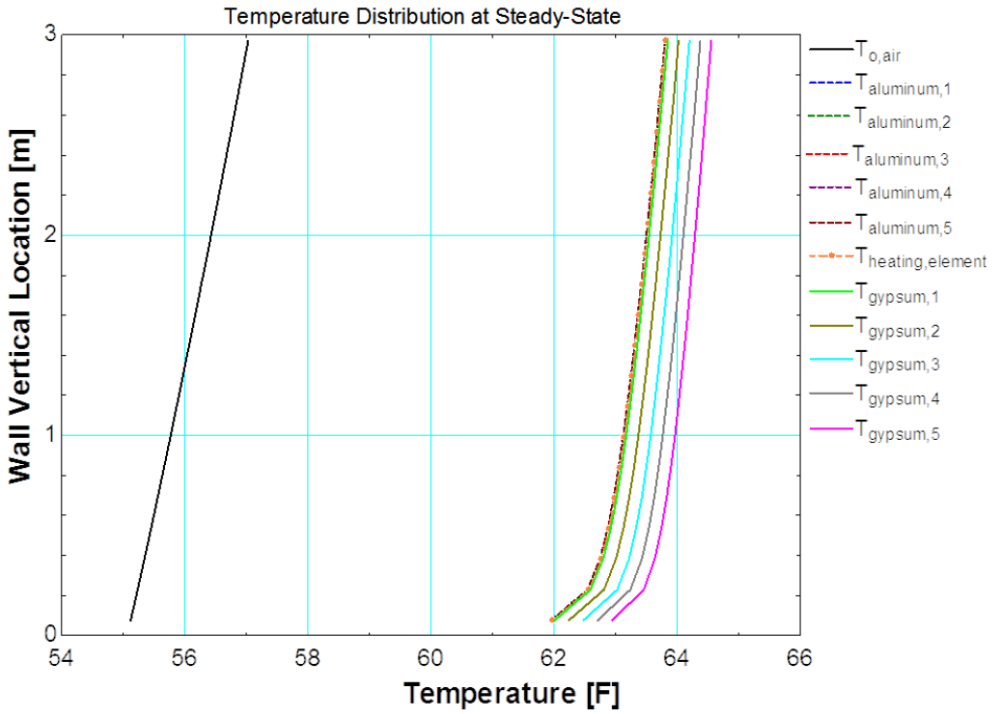

Figure 2.5 Steady-State simulation -Internal surface temperature vs. wall height for Approach 2

2.2.3 Chilled water and electric heating element-based system

Figure 2.6 shows a wall construction layout of the chilled water-based surface temperature control approach combined with a electric heat elements.

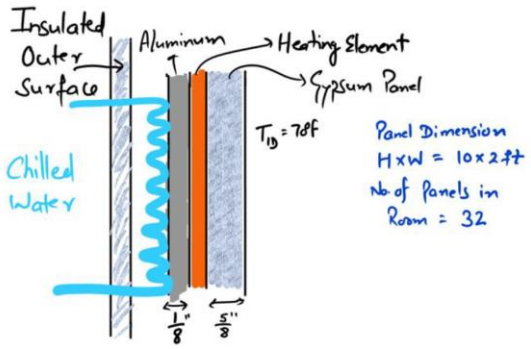

Figure 2.6 Approach 3-Chilled water and electric heating element-based system

As the transient response of the wall temperature control is also important, a transient study of the proposed wall in heating mode was carried out. Initially, it was assumed that the heater was off, and that the internal wall surface temperature was equal to 64°F, after which the heater was turned ON at a heat flux of 120 W/m^2. Figure 2.7 shows simulation results where the interior wall temperature increased by about 12°F over 3 hours. This duration was thought to be a reasonable response for the expected purposes of this test room. However, in this design configuration, the thermal resistance between the heating element and the chilled water loop is significantly lower than the thermal resistance between the heating element and the indoor air. It was determined that this difference in thermal resistance could lead to control issues and substantial cooling requirements when the system operates in the transition between cooling and heating mode. Hence this approach was ruled out. As an alternative, instead of a heating element, it was decided to use a hot water loop in addition to the chilled water loop. This approach is discussed in the next section.

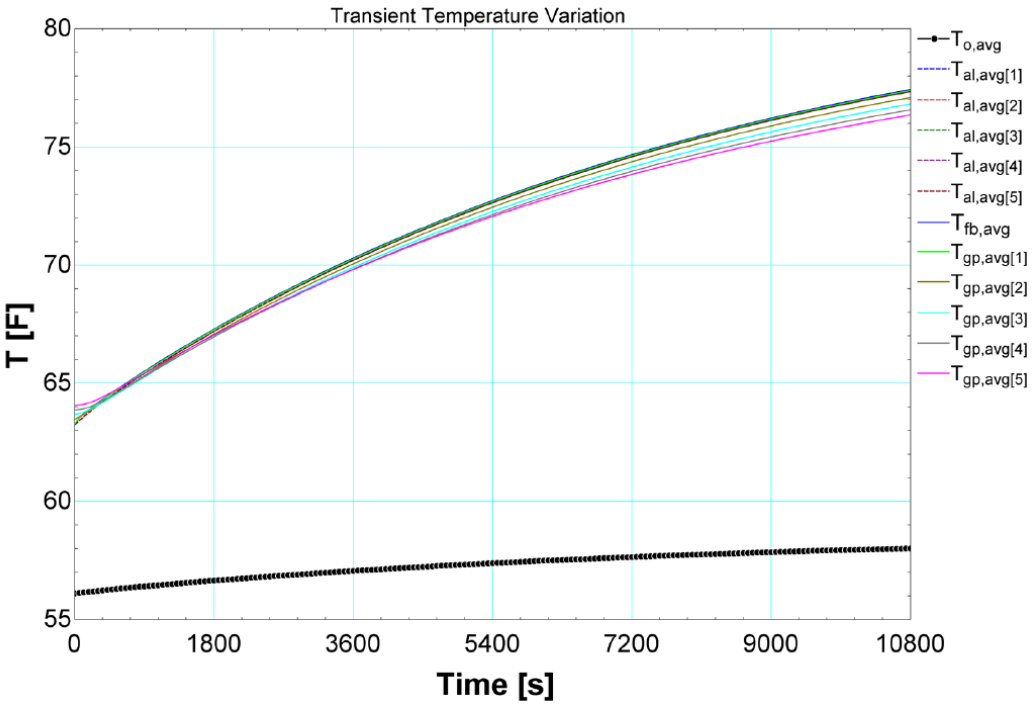

Figure 2.7 Heating mode transient analysis for Approach 3

2.2.4 Chilled and hot water based system

This approach controls the panel interior surface temperature by mixing chilled and hot water to achieve a desired target mixed water temperature that would depend on feedback control of the indoor surface temperature (dictated by the experiment). The idea is to have two parallel chilled and hot water loops and utilize a 3-way mixing valve to change the mixed water inlet temperature to each panel to maintain a desired interior surface temperature. The water flow rate for each panel is kept constant to reduce the overall system cost and control complexity. Figure 2.8 illustrates this approach.

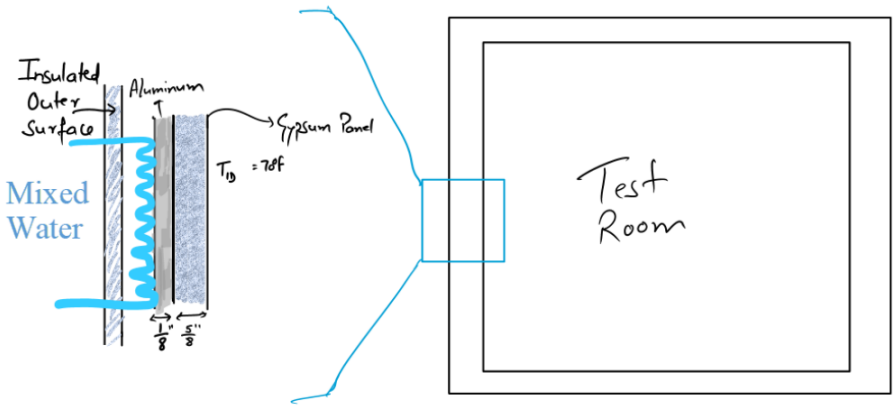

Figure 2.8 Approach 4-Chilled and Hot Water based system

Preliminary steady-state simulations were performed in EES (Klein, 2021) using a finite volume model of the panel to determine a water flow rate to achieve an acceptably uniform temperature distribution over the panel surface. In the simulation, the inside air temperature (T_{ID}) was assumed to be 21.11°C (70°F), and the outside air temperature was 23.33°C (74°F) (as the facility will be located in an indoor environment).

Figure 2.9 shows the steady-state temperature distribution across the panel height for a cooling case, with a water inlet temperature of 12.77°C (55°F) and a flow rate of 0.95 GPM. Figure 2.10 shows simulation results with the same flow rate for a heating case, with a water inlet temperature of 29.44°C (85°F). For the cooling case, the surface temperature is between about 59 and 60°F, whereas in heating, the range is between about 80 and 81°F. It can be seen from both the plots that the water flow rate results in a temperature change in water (black line) across the panel height of around 0.6°C (1.2°F) and a temperature difference along the panel surface (green line) of around 0.7°C (1.4°F). These are within acceptable limits. Based on the analysis results and 3-way mixing valve selection constraints, the water flow rate for each cooling circuit of a panel was specified to be 1 GPM.

This system suits the design requirements for the surface temperature target range and should be relatively easy to control to achieve a fast dynamic response.

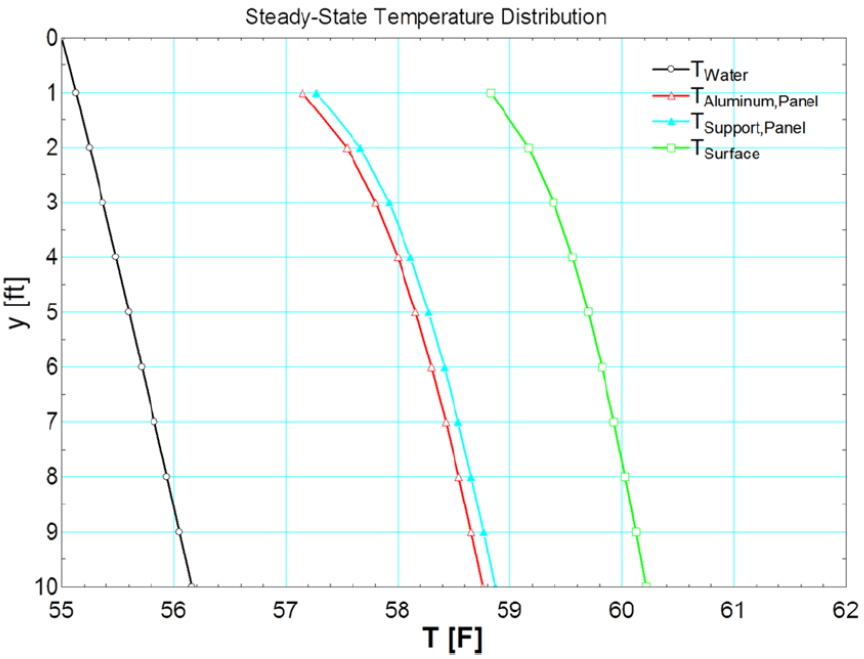

Figure 2.9 Panel steady-state simulation results for cooling

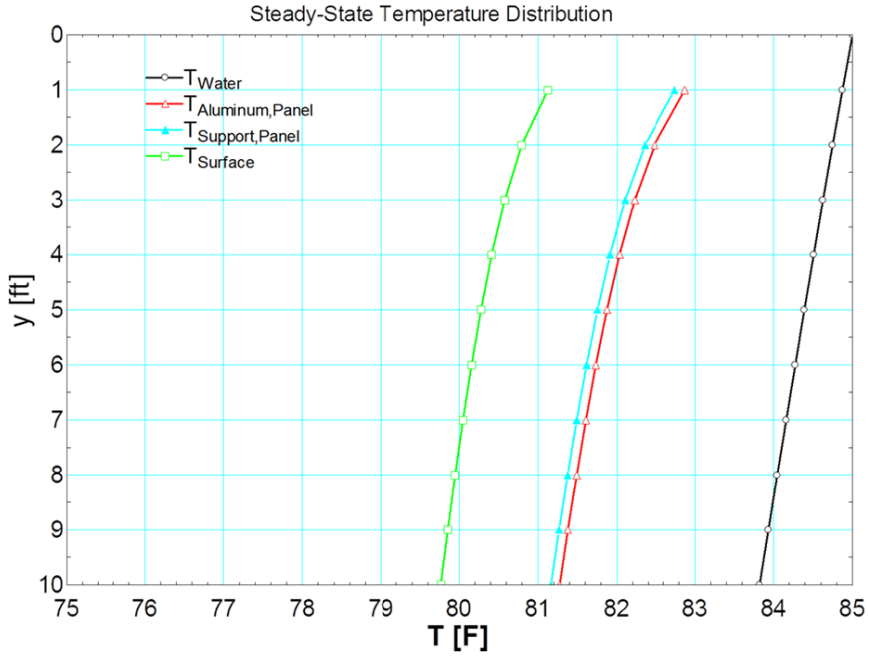

Figure 2.10 Panel steady-state simulation results for heating

2.3 HBIL Design Overview

The HBIL is located inside the Perception Based Engineering (PBE) lab at Ray W. Herrick Labs. The PBE laboratory enables occupant response testing under controlled conditions. Lighting, acoustics, vibrations, air quality, temperature, humidity, and visual stimuli inside this space can be manipulated to examine individual or combined effects of this. Hence, it is an excellent space to house the HBIL.

Figure 2.11 Location of HBIL - exterior view of Ray W. Herrick Laboratories building

Considering the target requirements outlined in Section 2.1 and the complexity involved in the HBIL design, it was decided to outsource the construction of this facility to a third-party firm specializing in modular construction. The following design features provide a good overview of the HBIL:

- Modular, 4'×5' size, thermo-active for walls, floor, and ceiling.
- Each panel can readily allow changes in the interior surface treatment. It was decided to use magnets to attach the interior finish panel to the aluminum base panel.
- The interior panels are embedded with a temperature sensor and a typical interior surface finish.
- Exterior insulation panel with R-value in range of R-20 to R-25 to check heat loss or gain.
- Design with aluminum T-channel in the middle of each panel to provide structural strength.
- Steel tube frames for attaching individual panels and for structural support to the entire facility

- Design using a screw jack with cross braces to provide access to the facility's bottom, support, and structural strength.
- Diffuser slots for air supply and standard lighting slots for lighting on the ceiling panels
- Symmetric design-two doors and two windows placed with an idea of dividing the facility into two identical spaces for future research.
- Hydronic system for providing hot and cold water to all the HBIL thermo-active panels.

Figure 2.12 illustrates the exploded view of the thermo-active panel layers. The insulation panel and aluminum base panel are screwed onto the standard support frame. The base panel has hydronic piping attached to the exterior side using the heat spreaders. The reconfigurable interior finish panel is mounted using magnets on the aluminum base panel. Figure 2.13 and Figure 2.14 show steel structure and exploded views of all the panels of the HBIL, respectively. Figure 2.15 exhibits an isometric view of the HBIL facility.

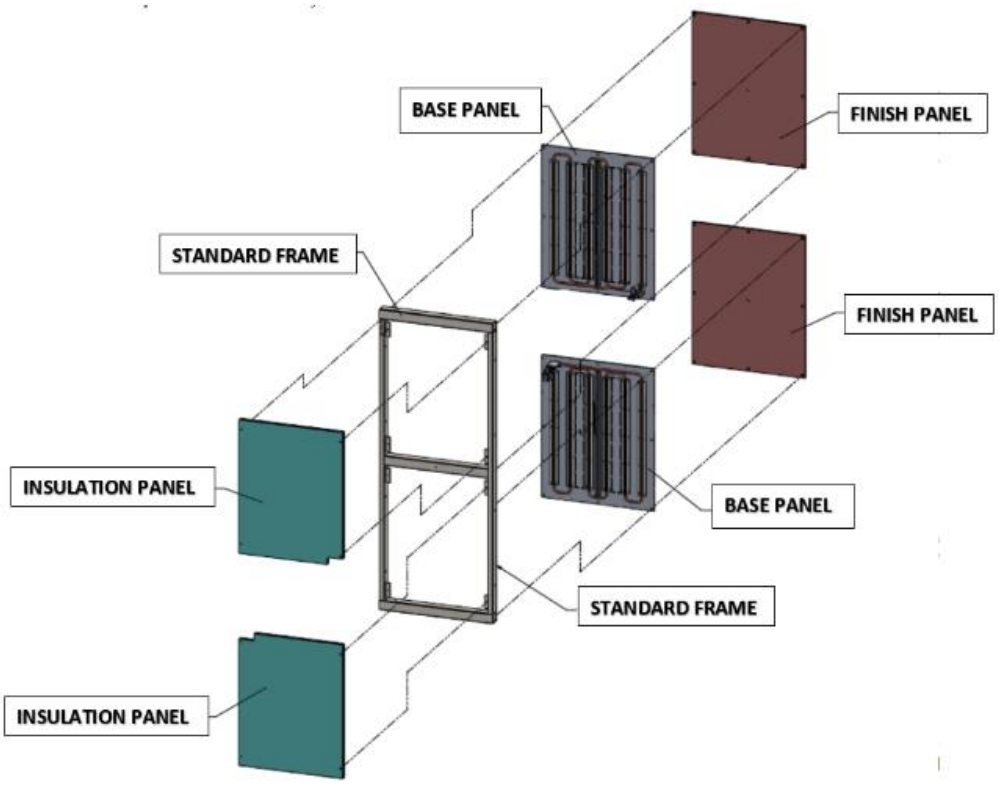

Figure 2.12 Exploded view - thermo-active panel

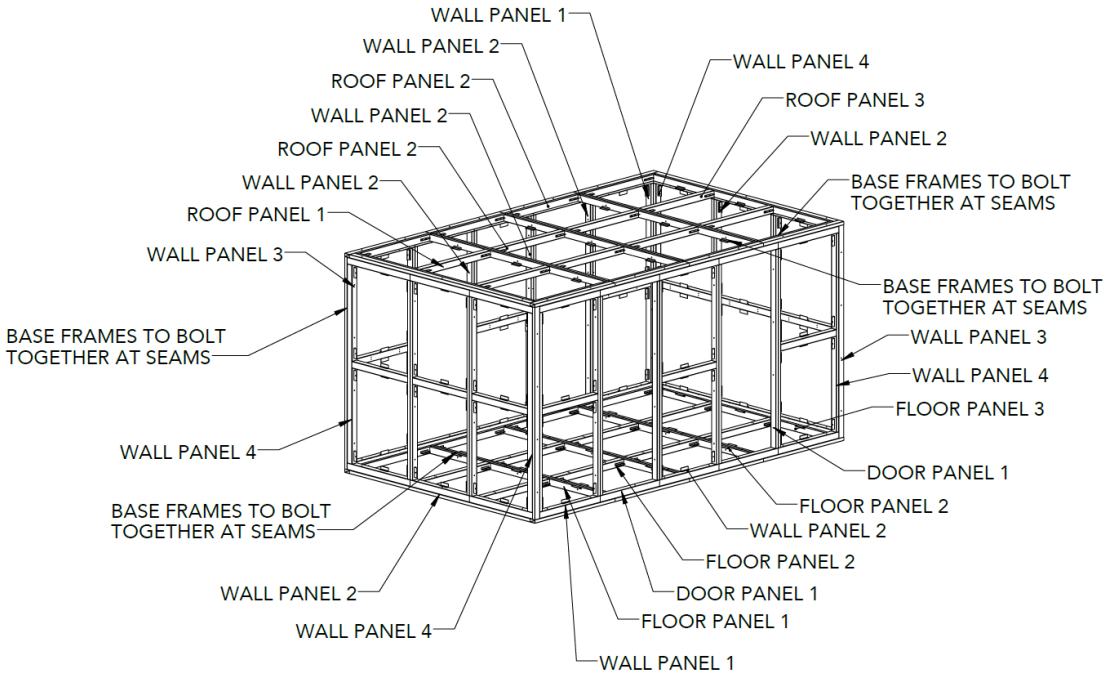

Figure 2.13 HBIL steel support structure

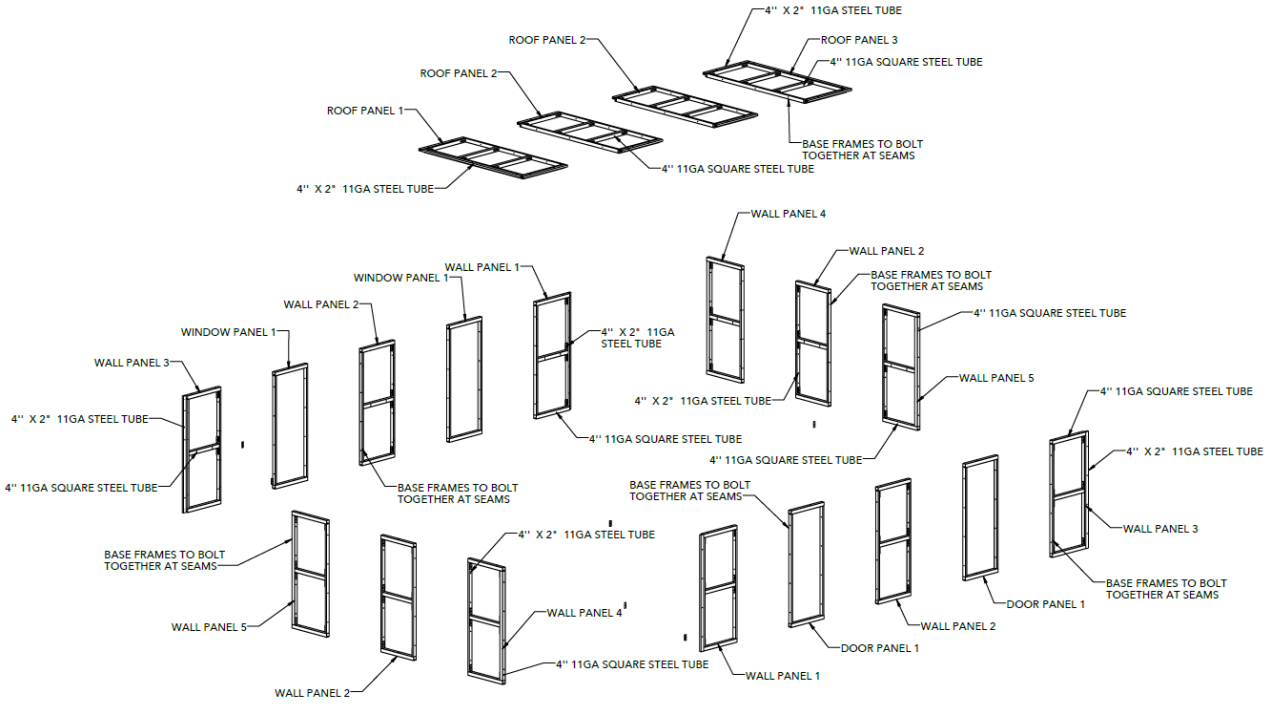

Figure 2.14 Exploded view- HBIL thermo-active panels

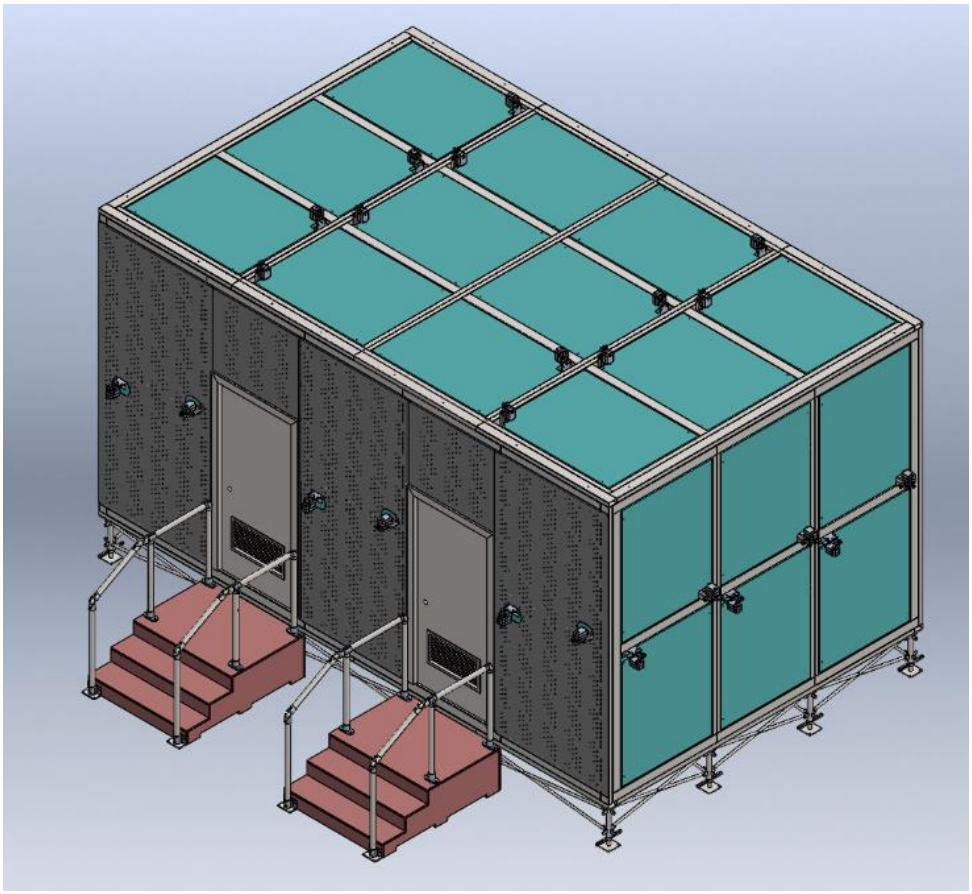

Figure 2.15 HBIL facility isometric view

3. THERMO-ACTIVE WALL PANEL DESIGN, TESTING, MODELING

3.1 Prototype Panel Design

A prototype panel was designed and constructed based on the panel surface temperature approach finalized in Section 2.2. Figure 3.1 depicts the initial conceptual design of a prototype panel assembly. The idea is to control the surface temperature of each panel by modulating the water supply temperature to each panel using a 4 -pipe common load hydronic system that continuously circulates cooling and heating water in two separate loops to 3-way mixing valves at the inlet of each panel. The panel includes a temperature sensor embedded in the interior surface treatment panel near the center of a 4'x5' panel to ensure better controllability of individual panel surface temperature and provide a reference for validating advanced sensing technology such as infrared-based surface temperature measurement.

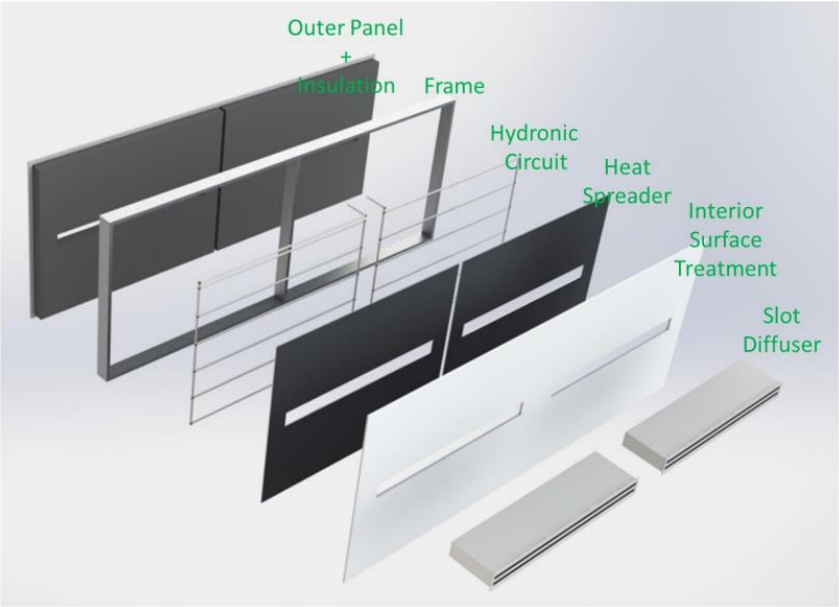

Figure 3.1 Exploded view of prototype panel concept

Figure 3.2 shows the assembly of the heat spreaders riveted on an aluminum support plate and installed inside a support frame of an initial prototype wall. Figure 3.3 presents a front view of the panel, with a white gypsum finish layer on an aluminum base plate that was screwed into the aluminum support frame. Figure 3.4 depicts the rear side of the prototype panel with PEX piping fitted inside the heat spreader slots.

Figure 3.2 Heat spreader-support plate assembly

Figure 3.3 Prototype panel front view

Figure 3.4 Prototype panel rear view

steady-state

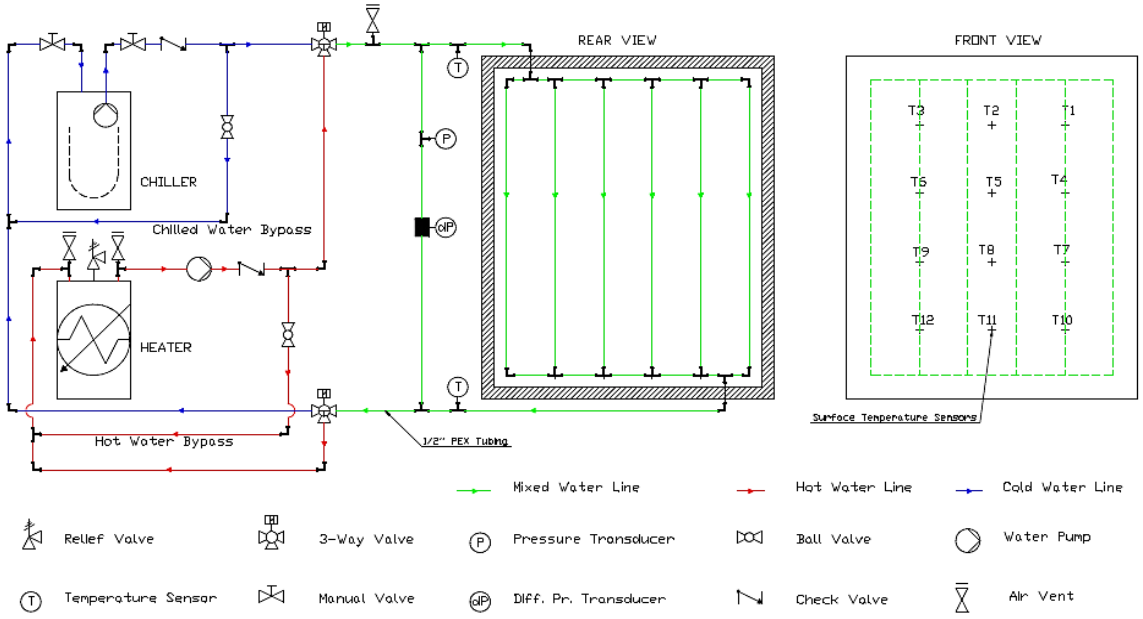

Figure 3.5 Initial prototype panel test setup schematic

A test setup was constructed to validate the steady-state and dynamic thermal performance of the prototype panel. A schematic of the initial test setup is illustrated in Figure 3.5. It consists of hot and cold water loops connecting to a 3-way valve that controls the water inlet temperature to the hydronic circuit that runs on the back surface of the panel. Figure 3.6 shows the 3-way valve with hot, cold, and mixed water connections. Since both the hot and cold water loops have single-speed pumps, two bypass loops on both hot and cold-water sides were added to control the water flow rate within the target range. A pressure transducer was installed to measure the water head pressure. A differential pressure transducer connected between the inlet and outlet of the panel measures the pressure drop across the panel, which can be used for validating the pressure drop calculations. Water inlet and outlet temperatures are measured by means of inline thermocouples installed at the inlet and outlet of the piping loop. Figure 3.7 shows the plumbing on the rear side of the panel with various sensor installations. The front view of the prototype panel has 12 thermocouples installed on the gypsum surface to capture the temperature distribution, as depicted in Figure 3.8. With this configuration, initial performance assessment tests were done. The control and data acquisition were done via NI LabVIEW (Bitter & Nawrocki, 2006). Figure 3.9 is the LabVIEW visual interface (VI)

of the test setup. The opening of 3-way valves is controlled, while the values of temperatures, head pressure, and differential pressure are logged at an interval of one second.

Figure 3.6 3-way valve

Figure 3.7 Test setup plumbing

Figure 3.8 Test setup with front view showing surface thermocouple locations

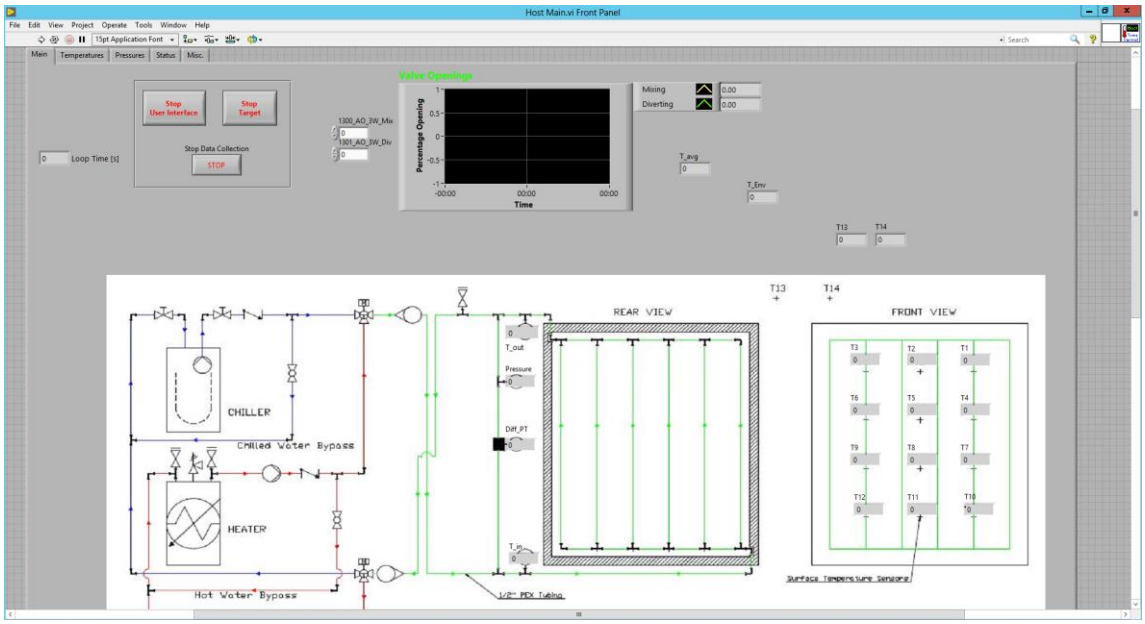

Figure 3.9 NI LabVIEW for prototype panel test setup

3.2 Prototype Panel Testing

The experimental investigations conducted on the prototype panel included three major parts:

1. Panel performance limit assessment: The thermal panel performance limit tests were conducted in heating and cooling mode by evaluating the maximum and minimum surface temperature that the panel could achieve using a 3.5 kW chiller and 6 kW heater for typical indoor conditions.

2. Steady-state and dynamic performance mapping: Experimental performance mapping of the prototype panel in steady-state and dynamic conditions. During steady-state testing, panel performance was studied by maintaining the surface temperature across various water flow rates and water inlet conditions to the panel. During dynamic testing, the panel time response to a change in its surface temperature induced by a change in the water inlet conditions was assessed.

3. Controllability of panel actuators: A 3-way mixing valve is employed in each panel to achieve a required water inlet temperature by mixing cold and hot water. In the prototype panel testing, the sizing and the controllability of this valve were assessed. Based on the panel performance mapping results, a PI feedback controller could be designed to maintain the panel surface temperature based on the 3-way valve actuation. Then, the controller design needs to be further assessed and fine-tuned with some additional testing.

3.2.1 Performance limit assessment and design modifications

As described in Section 2.1, the design goal was to obtain extreme panel surface temperatures of 15.5℃ (60℉) and 26.66℃ (80℉) for cooling and heating, respectively with a target mixed water flow rate of 1 GPM. The temperature on the panel surface was measured at twelve locations, as shown in Figure 3.8. The mixed water and inlet temperatures were also monitored. A temperature stratification was observed in the room air temperature from the ground level to 7 feet height. The air temperature at 1 foot above the floor was around 1°C lower than the temperature at a level of 7 feet above the floor level. Also, since all the panel layers were installed inside an aluminum frame, it was assumed that heat transfer would occur through the edges of the panel, thereby resulting in slightly different surface temperature readings compared to the central part. Keeping these factors in mind, the design goal was to have the surface temperature distribution across the twelve thermocouples within 1°C to 1.5°C.

During a typical performance assessment test, the heating mode was initiated first, and 100% hot water at around 45°C was circulated through the piping at the panel back until steady-state conditions were achieved. Steady-state was defined, such that the panel surface temperature reached the highest possible value and stayed within a tolerance of ± 0.4°C for 10 minutes. After a 10-minute steady-state measurement, the system was switched to cooling mode, and 100% chilled water was circulated through the panel. The chilled water loop provided around 4.5°C water at the inlet of the panel. Once the chilled water loop was engaged, the surface temperature change was monitored until a steady-state condition was achieved with the lowest surface temperature possible. A thermal camera was also set up to capture surface temperature variation from the start until the final steady-state was achieved.

Initial test results with PEX tubing showed that the design panel surface temperatures were achieved. However, the experimental results showed an unacceptable non-uniform surface temperature distribution. This non-uniformity was caused by the absence of water flow in the hydronic circuit last loop, as indicated in Figure 3.10 (Layout 1). A thermal image in Figure 3.11(a) clearly shows the absence of water in the last vertical loop. The piping layout was modified to provide a more uniform flow distribution, as illustrated in Figure 3.10 (Layout 2). A thermal image in Figure 3.11(b) showed water flow in the last loop. However, after testing Layout 2, a non-uniform surface temperature distribution was still observed, which indicated a non-uniform flow distribution across different passes. Both initial tests suggested that the change in water temperature between the

inlet and outlet of the panel was small. Hence, the hydronic circuit layout was modified to a series flow configuration, as illustrated in Figure 3.10 (Layout 3). Layout 3 led to a more uniform surface temperature distribution, with a slight increase in water temperature difference between inlet and outlet as compared to the previous two cases. Based on these findings, a series layout was adopted as a final configuration of the hydronic circuit on the back of the panel. Further tests were conducted in this configuration with PEX tubing and then with copper tubing.

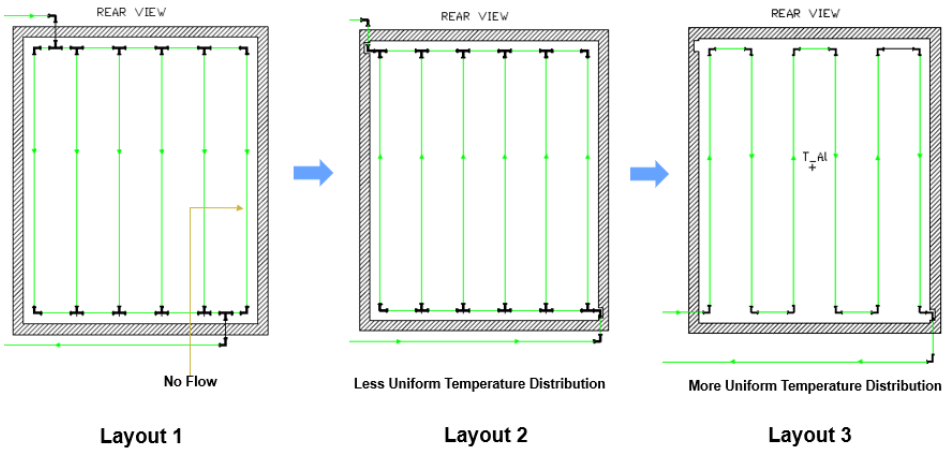

Figure 3.10 Piping layout modifications

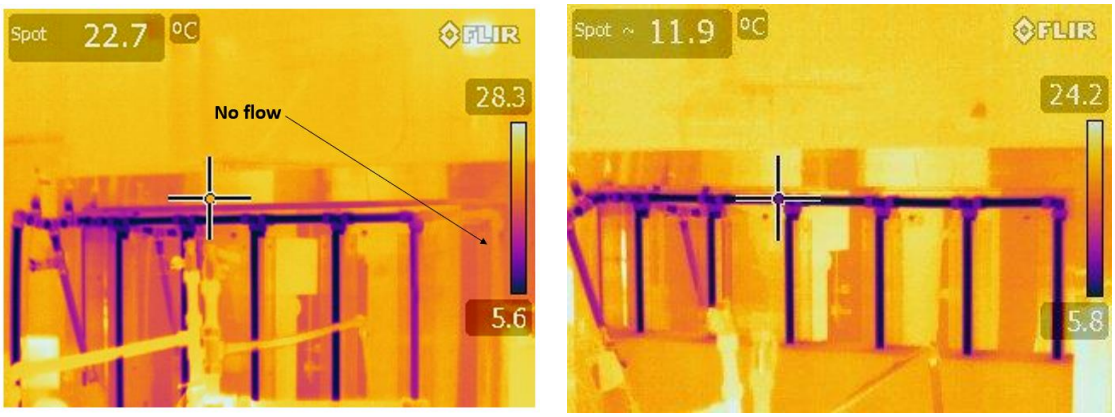

(a) Layout 1 (b) Layout 2

Figure 3.11 Thermal images of PEX pipe on the rear side of initial prototype panels

With a series configuration, the PEX tubing configuration was tested. Figure 3.12 shows the panel surface temperature variation at all twelve temperature locations for the performance limit assessment test with PEX tubing. The maximum average panel surface temperature achieved was around 30°C, while the minimum was around 15°C. These results satisfied the design goal of the

surface temperature from 15.5°C to 26.66°C. However, the transient response was considered to be too slow. It took around 90 minutes to reach the minimum surface temperature from the maximum, which did not meet the transient design goal. A target response time of around 45-50 minutes (time required for the panel to achieve an extreme steady-state temperature when the cooling or heating is started at room temperature conditions) was chosen.

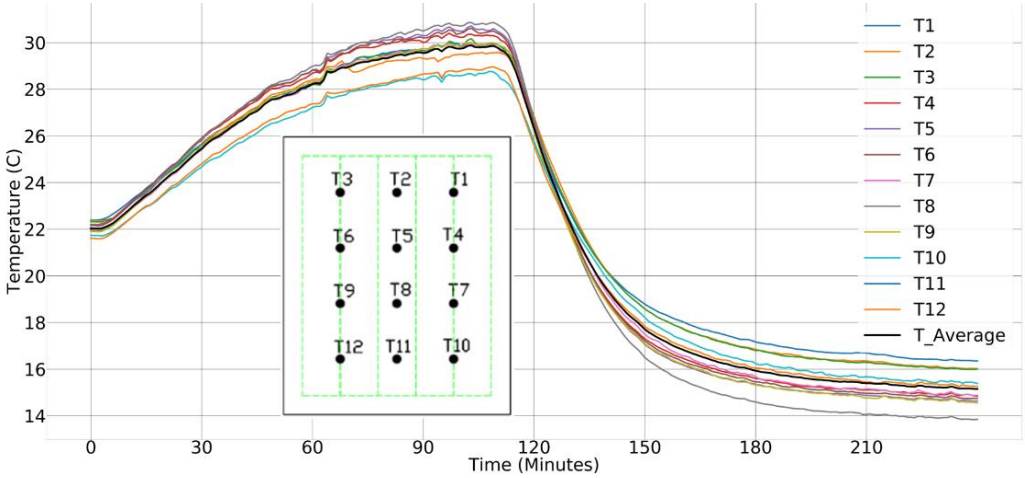

Figure 3.12 PEX tubing performance limit test results

PEX tubes were replaced with copper tubes, as shown in Figure 3.13. The goal was to decrease the response time while achieving the target surface temperatures.

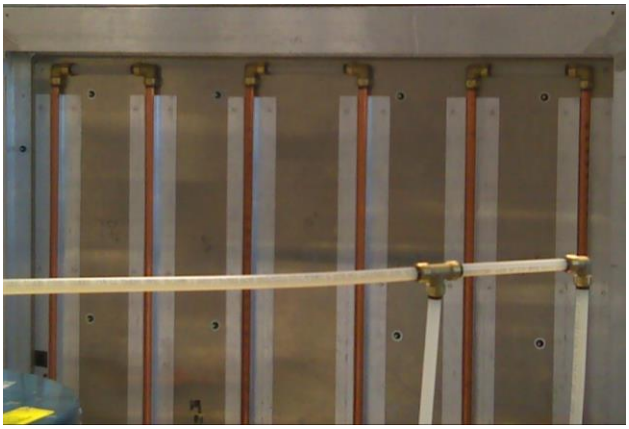

Figure 3.13 Test setup modification-PEX tubes replaced with copper tubes

Figure 3.14 shows test results with the copper tubing. The time required to reach maximum heating or minimum cooling steady-state temperature was reduced by 40%. In addition to the quicker response, there was a 2°C rise in heating steady-state panel surface temperature and a 1.5°C drop in cooling steady-state panel surface temperature compared to the test with PEX tubing. In addition,

during this test, the effect of rear insulation on the panel surface temperatures was also studied. Each thermocouple without rear insulation showed a temperature drop of about 1°C, as shown in Figure 3.14.

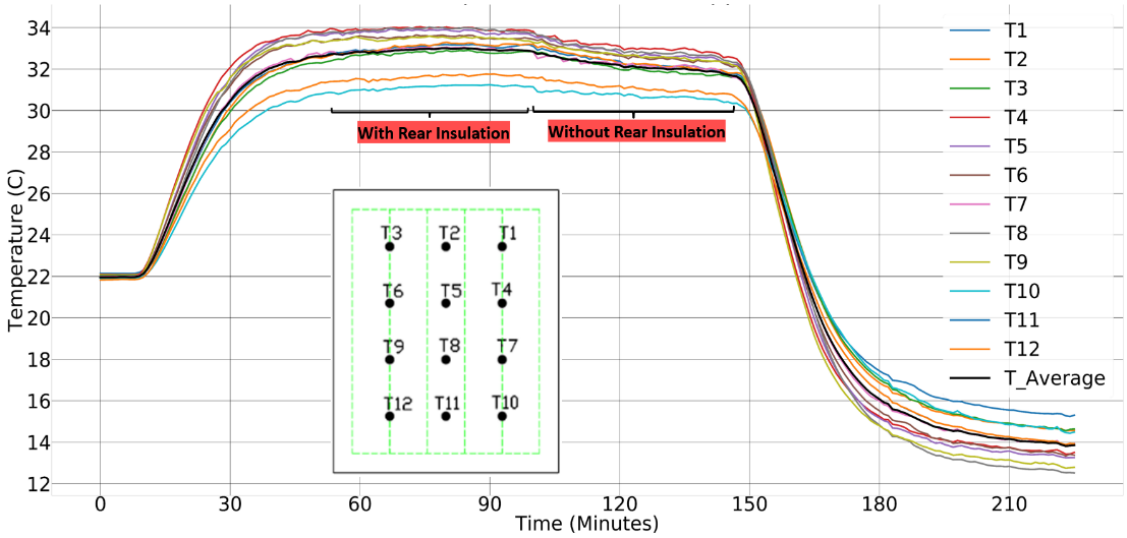

Figure 3.14 Copper tubing performance limit test results

Thermal images of the panel surface shown in Figure 3.15 were also used to validate prototype performance. The bottom left corner of each image shows the spot temperature, which is the temperature of the cross mark at the center of the image. At the top of each thermal image, there is a maximum and minimum temperature range in the frame. Figure 3.15(a) (PEX tubing) and Figure 3.15(b) (copper tubing) compare the steady-state cooling surface temperature distribution of PEX and copper tubes. It can be seen that the spot temperature for copper tubing is around 2.5°C lower than the PEX. Also, the range of surface temperatures for the copper case is lower, which agrees with the plots in Figure 3.14. Similarly, Figure 3.15(c) (PEX tubing) and Figure 3.15(d) (copper tubing) compare the steady-state heating results. In this case, copper tubing shows around 5°C higher steady-state temperature at the center. The range of surface temperatures is higher in this case too.

A significant heat gain/loss occurs at the edges of the panel, as evidenced by the significant temperature gradient that is observed. Consequently, the region with the lowest temperature value is in the center of the panel. This temperature distribution aligns with the thermocouple readings plotted in Figure 3.12 and Figure 3.14. It can also be observed that the temperature measured by thermocouples closer to the floor (T11, T12) was lower than the rest of the thermocouples, which aligns with the indoor air temperature stratification previously explained. It should be noted that

panel edge losses should be dramatically reduced when the panels are installed within the facility if adjacent panels are operating at similar conditions. It should also be noted that these experiments were extremely useful in finalizing the prototype panel design and validating the prototype panel model described in Section 3.3.

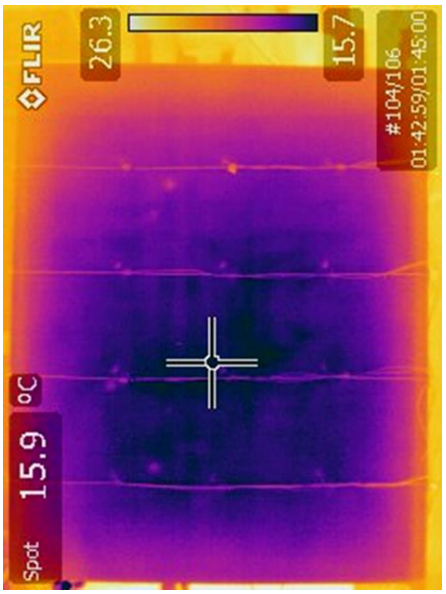

(a) PEX cooling steady-state

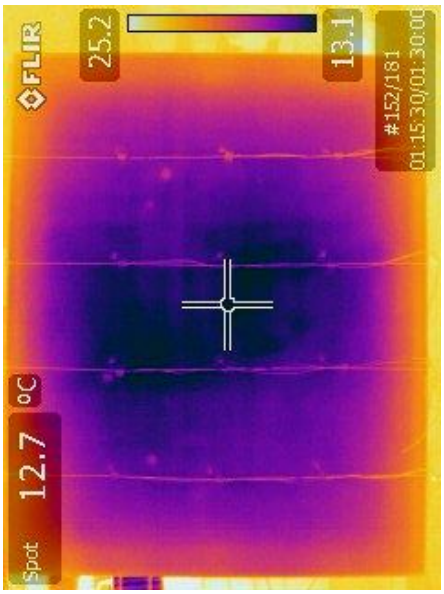

(b) Copper cooling steady-state

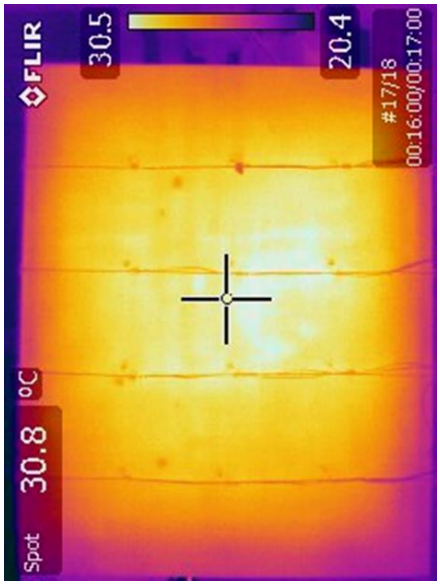

(c) PEX heating steady-state

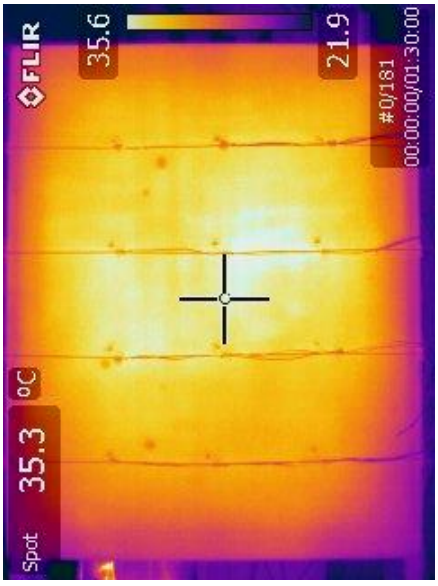

(d) Copper heating steady-state

Figure 3.15 Thermal images for PEX vs. copper tubing at steady-state for prototype panel

3.2.2 Heat Spreader Testing

Heat spreaders play a crucial role in enhancing heat transfer between the water tube wall and the back-surface aluminum plate. Hence, two different available options were studied, as shown in Figure 3.16, both in terms of performance and ease of assembly during the panel manufacturing. Figure 3.17 provides a schematic of the heat spreader test setup. Two heat spreaders were attached with thermal paste (between the heat spreader and back panel surface) and two without, as can be seen in the 'front view' in Figure 3.17. Note that the prototype panel on which the performance limit testing was done has C-type heat spreaders.

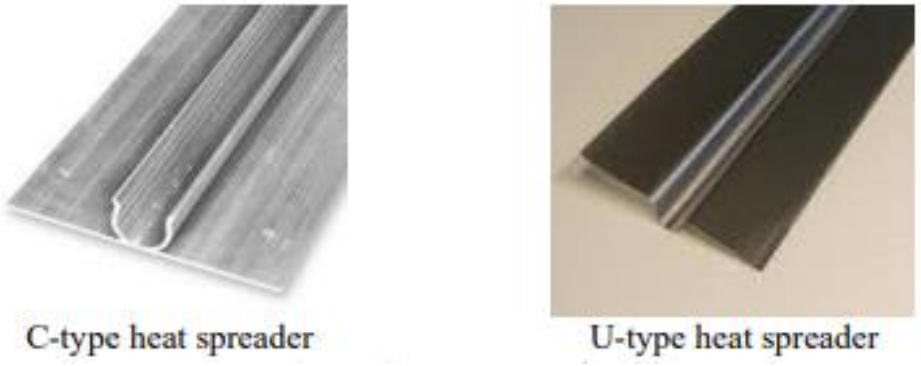

Figure 3.16 Heat spreaders

The test procedure was similar to the prototype panel testing described in Section 3.2.1. The only difference was that there were six thermocouples attached on the front side of the aluminum base plate (see Figure 3.18(a)) on the heat spreader test setup to measure the surface temperature as opposed to the twelve on the drywall surface of the prototype panel. In addition to that, four thermocouples were attached to the rear side copper tubes to measure the temperature drop. Figure 3.18(b) shows a rear view of the test setup. The goal of the tests was to evaluate which one of the two configurations was better in terms of thermal conduction between the base plate and pipe.

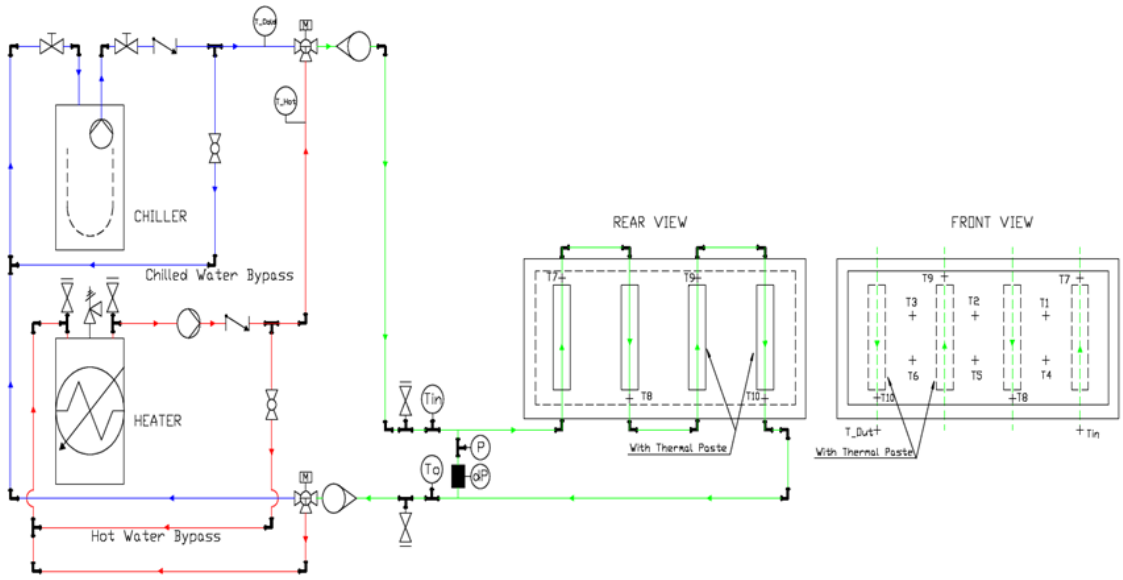

Figure 3.17 Heat spreader test setup schematic

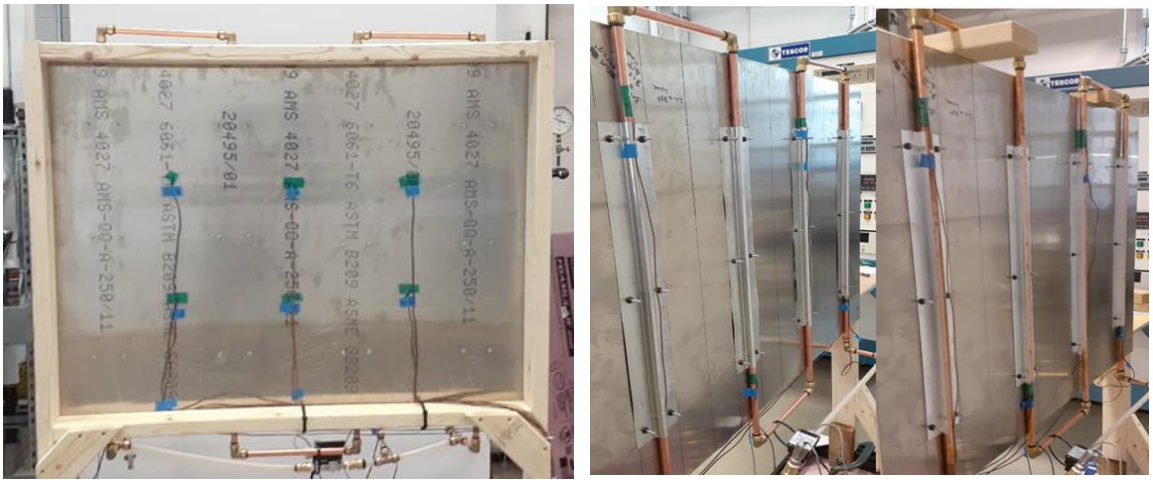

(a) Front view (b) Rear View

Figure 3.18 Heat spreader test setup

The plots in Figure 3.19 and Figure 3.20 compare transient test results as well as steady-state conditions achieved. It is evident that the C-Type heat spreaders show better performance. The time required to reach the cooling and heating steady-state with the C-type was at least 5-7 minutes less than the U-type heat spreaders. Also, the panel surface average temperature was around 1.5°C lower in cooling and higher in heating mode. C-type panels are more rigid in terms of ease of manufacturing and have more uniform flat surface contact with the panel's backplate. However, the

U-type heat spreaders are formed from thinner sheet metal, often deflected during attachment. Hence, C-type heat spreaders were selected as a better option amongst the two.

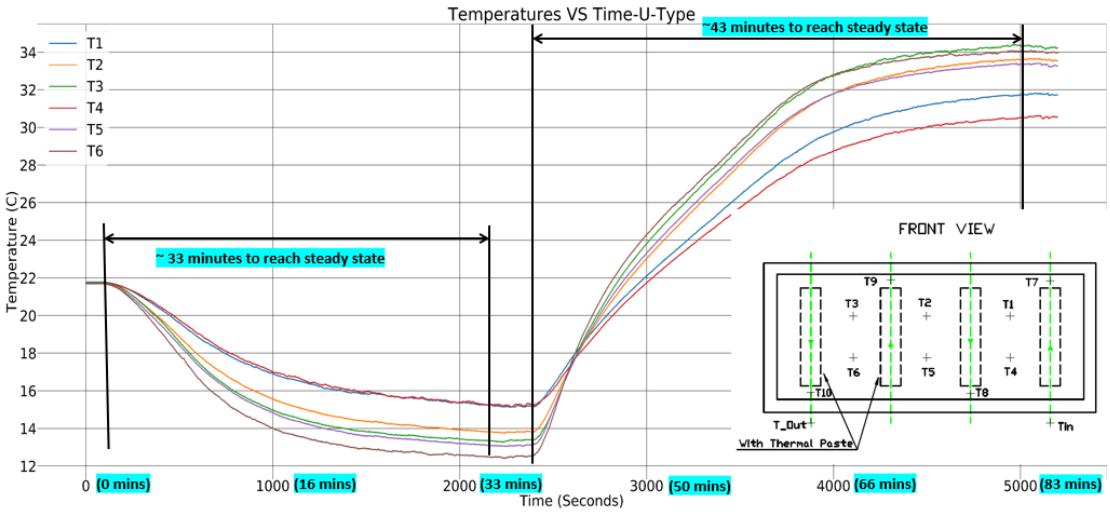

Figure 3.19 U-type heat spreader test results

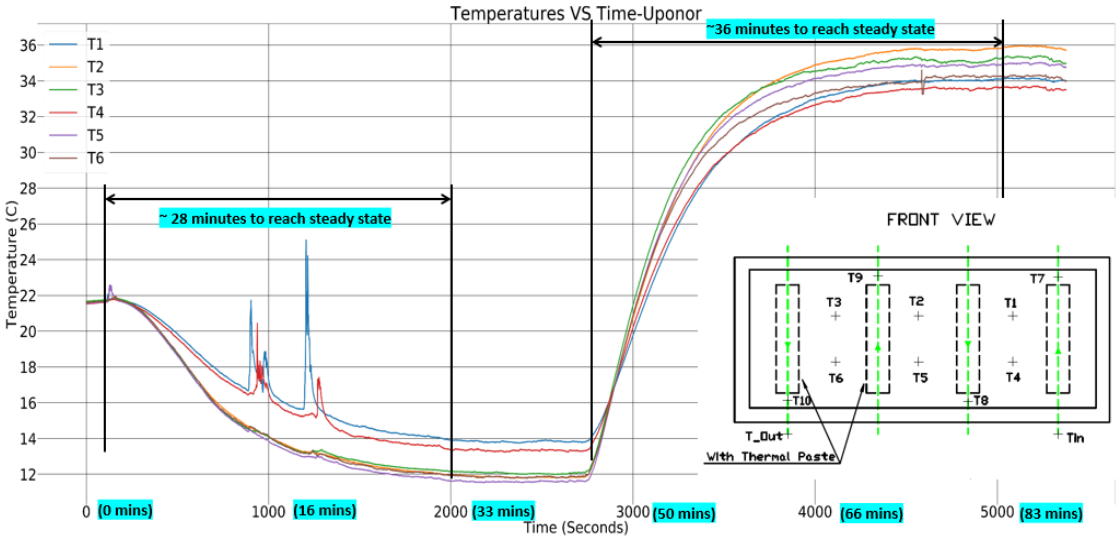

Figure 3.20 C-type heat spreader test results

Figure 3.21 shows steady-state test results for the C-type heat spreader along with the layout of thermocouples on the heat spreader testing setup in “front view” and “rear view.” Thermocouples T1 to T6 were on the front panel surface, while T7 to T10 were on the copper tube surface on the rear side. Thermocouples T3, T6 were between the heat spreaders attached with thermal paste, while

T1 and T4 were between the heat spreaders attached without thermal paste. It was observed from Figure 3.21 that thermocouples T1 and T4 showed the lowest temperature readings in heating and highest temperature readings in cooling. Thus, it can be concluded that applying thermal paste improves the heat transfer, thus increasing and decreasing the temperature of the panel surface by around 1.5 to 2°C in case of heating and cooling, respectively.

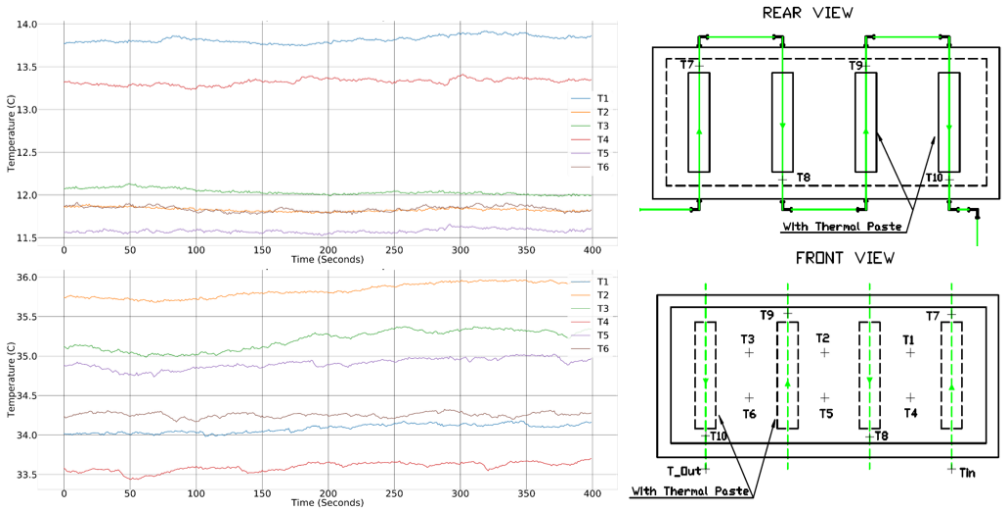

Figure 3.21 Effect of thermal paste between the heat spreader and back plate

3.2.3 3-way Valve Testing

As a next step, it was necessary to characterize the 3-way valve and study its performance and limitations. To characterize the 3-way valve, a dynamic performance map was developed, followed by a quasi-steady-state performance map. Based on these test results, the logic for actively controlling the panel surface temperature will be developed.

A preliminary test was done for 3-way valve dynamic performance mapping to get an idea of mixed water temperatures at different mixing valve opening percentages. In this preliminary test, a data point was recorded every 5 minutes after the mixing valve opening was changed. A total of 20 data points ranging from 0% to 100% (with a step of 5%) were taken. The bypass valves for full cold (0%) and full hot (100%) were adjusted such that the water flow rate for both these conditions was 1 GPM. The remaining data points between 0% and 100% were measured without changing the bypass valve positions. Water temperature was measured using a thermocouple probe immersed in the mixed water stream at the outlet of a 3-way mixing valve. The water flow rate was measured using a rotameter.

Figure 3.22 presents the mixed water temperature plotted against the mixing valve opening. Furthermore, Figure 3.23 shows the mixed water flow rate plotted against the different mixing valve openings from the same tests.

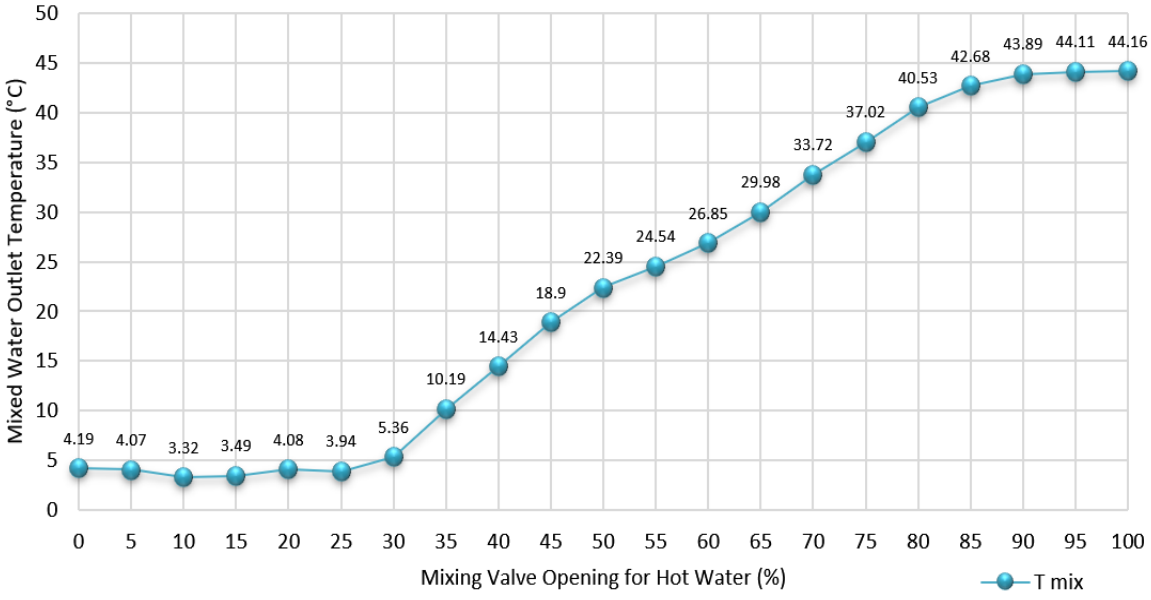

Figure 3.22 3-way mixing water temperature vs. valve opening

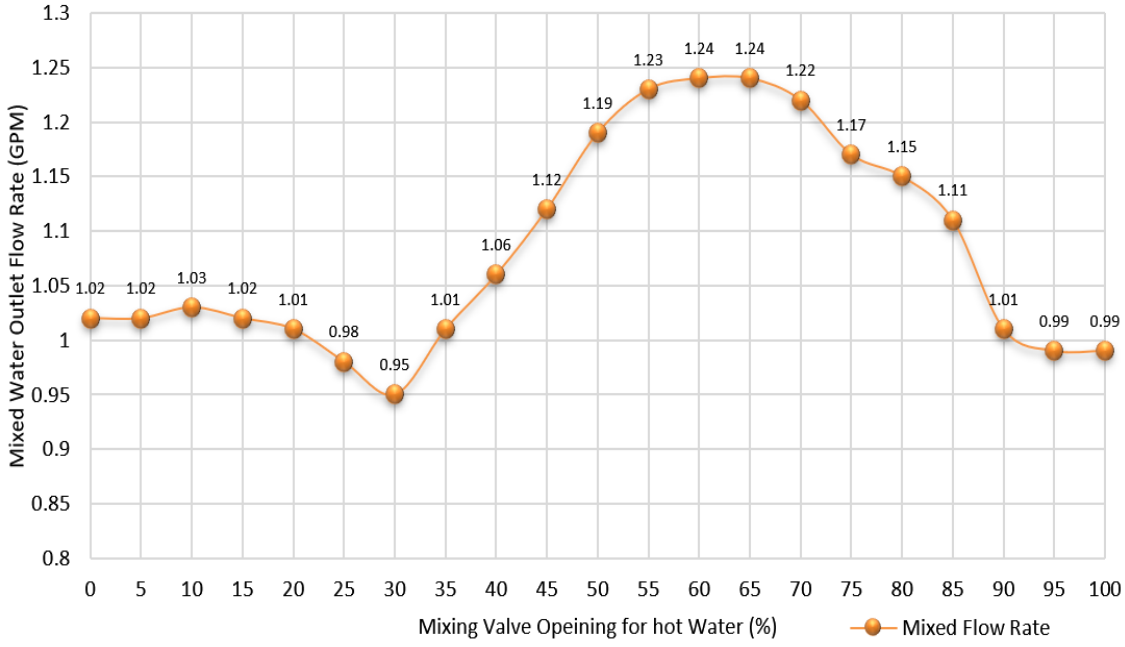

Figure 3.23 3-way mixing valve flow rate vs. valve opening

From these plots, it is evident that from 0% to 30% valve opening, there is no significant change in the mixed water temperature. Similar behavior is observed from 85% to 100% opening. Hence the primary control region for the mixing valve control is between 30% to 80% opening. The water flow rate was observed to vary between 0.99 to 1.24 GPM for the range of 3-way mixing valve positions.

It was observed that for 5°C water, the cold-water pump provided a 1 GPM flow rate at 28.35 psi head pressure. Also, for 42°C water, the hot water pump provided a 1 GPM flow rate at 28.33 psi head pressure. The mixed water temperature for different mixing conditions showed results similar to those in Figure 3.22. However, because the head pressures for hot and cold-water inlets were fixed at 28 (±0.5) psi (by adjusting the bypass valves) for extreme cooling and heating conditions, the water flow rate at the mixing conditions dropped below 1 GPM (the bypass valve position or head pressure was not changed during mixing). This behavior can be explained by analyzing the control of the valves. After opening the mixing valve for hot water (Port B), the head pressure in the cold water line increased above the initial 28 psi value due to the restriction on port A (refer to Figure 3.24). To change the head pressure to 28 psi, the cold water bypass valve needed to be opened, which decreased the cold water flow rate. The same happened with the hot water flow rate when we tried to decrease the head pressure when there was a restriction on port B. Also, note that, as per the 3-way valve specifications, the hot side port's opening is 70% of the cold side port. Hence, the same percentage of bypass valve opening does not correspond to a proportionate change in the head pressure of hot and cold-water lines. This decrease in head pressures (between 30-70% opening) led to a decrease in the mixed water flow rate as compared to the extreme cooling or heating conditions.

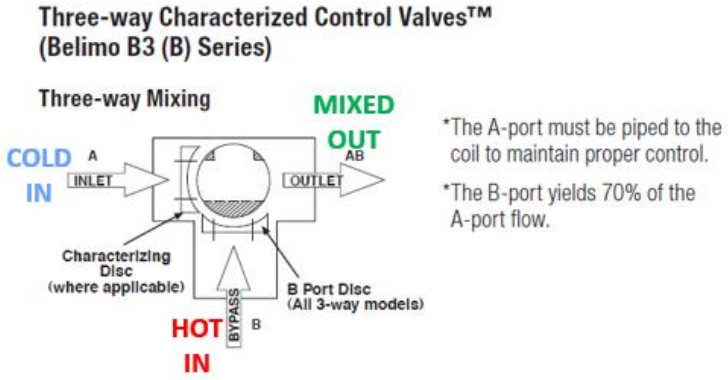

Figure 3.24 3-way valve port openings

For 3-way valve quasi-steady-state mapping, the hot water temperature was maintained at 44 (±1)°C, and the cold-water temperature was maintained at 4 (±1)°C for all mixing conditions. Both cold and hot water pumps provided a 0.95 to 1 GPM water flow rate at around 28 psi head pressure. Hence head pressure on the cold and hot water side was maintained at 28 (±0.5) psi for all the data points. Steady-state data points between 30% to 65% have been tabulated. The 3-way valve opening was fixed at each data point until the panel surface temperature reached a quasi-steady state. Table 3.1 shows the quasi-steady-state test results for different mixing valve opening percentages. It is evident that the 3-way valve can provide the required surface temperatures with a reasonable mixed water flow rate. These results will be used to develop a PI control logic in LabVIEW for automatically controlling the mixing valve opening based on the required panel surface temperature input.

Table 3.1 3-way valve quasi-steady-state mapping results

Mixing (%)	Mixed Flow Rate (GPM)	T in (°C)	T out (°C)	Mixed Head (psi)	Δ*P* (psi)	T Surface (°C)	T Al Back (°C)
0	0.958	4.53	5.26	13.22	3.03	14.35	10.45
30	0.801	6.72	7.5	12.1	2.33	15.14	11.8
35	0.832	10.32	11.17	12.61	2.34	17.02	14.54
40	0.831	16.36	16.86	12.28	2.34	20.01	18.55
45	0.833	19.91	20.24	12.18	2.06	21.64	21.19
50	0.712	25.62	25.52	11.62	2.14	24.1	24.85
55	0.764	26.86	26.72	13.09	2.12	24.05	25.43
60	0.749	30.62	30.26	15.45	1.66	26.19	28.1
65	1.005	36.5-33	36-32.8	15.5-16.5	2.62	28.8-29.7	31-32
85	0.95	39.73	39.26	13	2.22	31.3	34.6
100	0.991	44.55	43.69	10.96	2.60	33.31	38.29

3.2.4 Panel Surface Temperature Measurement Approach

The panel surface temperature for the initial prototype test setup was measured using thermocouples attached to the surface. However, in the actual HBIL facility, it is desired that the temperature sensor should not be visible to the occupants for aesthetics and testing purposes. Hence, the idea is to embed a temperature sensor inside the surface treatment panel. The key objective of the tests described in this section was to find a cost-effective solution for measuring the surface temperature within ±0.5°C of the actual surface temperature value and have an attachment that

would provide easy removability in case of damage or replacement. Three options were tested. In particular, the attachment method, type of sensor, and individual test results are discussed further.

A probe-type thermocouple was initially tested (see Figure 3.25(a)), which had a threading attachment that facilitates its mounting in a threaded hole in the aluminum backplate, as shown in Figure 3.25(b). The part of the probe touching the back and support panel was insulated while the tip touching the gypsum layer was left uninsulated, as shown in Figure 3.25(c). The exposed tip was covered with thermal paste before screwing it to avoid any air gap and provide better contact with the gypsum layer. The temperature reading from this sensor ($T_{Sensor1}$) was compared with the thermocouple attached at the center of the prototype panel surface ($T_{Surface}$). Results showed that $T_{Sensor1}$ read 1.5°C to 2°C different than $T_{Surface}$. This was because heat transfer occurred between the aluminum back-plate and the sensor probe despite insulating it. Although providing easy attachment, this sensor was not considered suitable for the panel surface temperature measurement.

(a) Probe-type thermocouple sensor

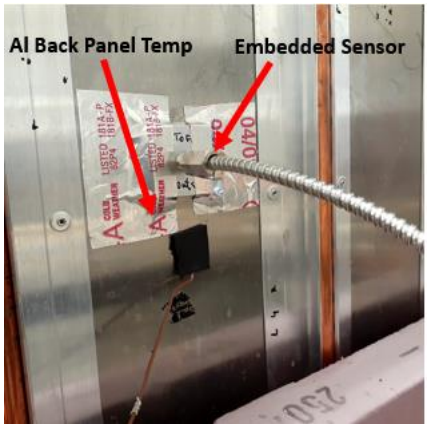

(b) Probe-type thermocouple assembly

(c) Probe-type thermocouple tip

Figure 3.25 Probe-type thermocouple testing

The second approach was to embed a welded thermocouple tip, as shown in Figure 3.26(a) directly into the gypsum layer and cover it with drywall mud. The tip was inserted in a small hole as close to the surface as possible, as shown in Figure 3.26(b). Then it was covered with mud from the front side. After the mud dried, the sensor was held in place by the mud, and the front surface of the panel was polished with sandpaper making it look like the gypsum surface, as shown in Figure 3.26(c). The temperature reading from this sensor ($T_{Sensor2}$) was compared with the thermocouple attached at the center of the prototype panel surface ($T_{Surface}$). Results showed that $T_{Sensor2}$ readings were within 0.5°C of the $T_{Surface}$ at steady-state cooling conditions. However, $T_{Sensor2}$ readings were

approximately 2.5°C off compared to the $T_{Surface}$ at steady-state heating conditions. This behavior was due to the heat transfer occurring through the air gap from the hot aluminum plate. Another reason could be the presence of mud in contact with the aluminum in the hole.

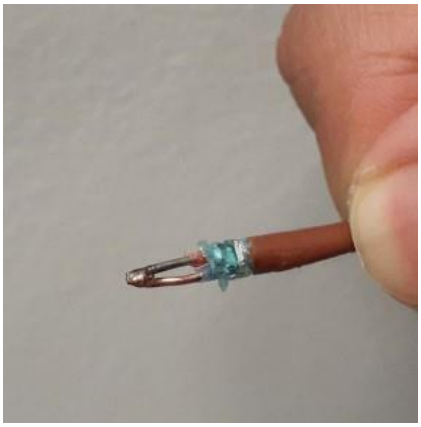

(a) Welded-tip thermocouple sensor

(b) Welded-tip thermocouple in dry-wall

(c) Welded-tip thermocouple embedded

Figure 3.26 Welded-tip thermocouple testing

The third tested approach involves using an embedded-type miniature thermocouple probe sensor. Figure 3.27 shows an image of this sensor. It has a cylindrical head of 0.275- inch diameter and 0.25-inch length (equal to the thickness of the surface treatment layer). The head prevents it from slipping back from the rear end. The wire has stainless steel over braid, making it robust and mechanically strong. Figure 3.28(a) shows the miniature probe sensor's cylindrical head being inserted inside the drywall from the front side. Figure 3.28(b) shows the cavity inside the drywall to embed the cylindrical head. Insulation tape was added between the rear side of the head to avoid direct contact with the aluminum back plate. Figure 3.28(c) shows the drywall front surface, finished after embedding the sensor inside the cavity. The temperature reading from this sensor ($T_{Sensor3}$) was compared with the thermocouple attached at the center of the prototype panel surface ($T_{Surface}$). The measured $T_{Sensor3}$ matched reasonably well with $T_{Surface}$ in cooling steady-state. However, it read very close to aluminum backplate temperature in heating at steady-state, similar to the welded tip thermocouple. This was because part of the sensor was always in contact with the aluminum back plate, despite adding the insulation.

Figure 3.27 Miniature probe thermocouple sensor

(a) Miniature Probe thermocouple sensor

(b) Drywall hole to embed cylindrical head

(c) Drywall after embedding sensor

Figure 3.28 Miniature probe sensor testing

It was evident that all three approaches needed some correction, and none of them read within the target goal of ±0.5°C for both heating and cooling cases. The idea of embedding a welded tip thermocouple directly into the mud showed better results than both the probe-type sensors. Also, it was the least expensive approach. However, the downside of embedding welded tip wire is that it is difficult to hold it in the gypsum layer without slipping back. The hole diameter will always be greater than the diameter of the welded tip. A slight jerk from the rear side may either break the thermocouple or damage the weld. To tackle this issue, a miniature thermocouple adapter is used in the final design, and the air gap is eliminated by adding nonconductive glue. A cable clip wire clamp is used, as shown in Figure 3.29, for pull stress proofing the thermocouple wire. All the thermocouples are embedded in the surface treatment panels in this fashion.

Figure 3.29 Welded-tip thermocouple assembly in final design

3.3 Transient Model Development, Tuning and Validation for Initial Prototype

The prototype wall panel is essentially a composite wall with copper tubes and heat spreaders on the rear and a gypsum panel on the front side. Figure 3.30 shows a sectional view of the panel. A 1-D transient thermal network model for this prototype wall panel was developed in EES (Klein, 2021) to predict the thermal behavior of the panel and guide design choices. Figure 3.31 illustrates the thermal network diagram for the model with different layers of the prototype wall panel. The critical inputs of the model are mixed water inlet temperature, outdoor temperature, and indoor air temperature values. The model calculates the panel surface temperature, water outlet temperature, and aluminum backplate temperature values. In addition, the heat transfer that occurs from water to the indoor air ($\dot{Q}_{front}$), the heat lost to the outdoor air ($\dot{Q}_{loss}$), and the heat lost through panel frame or edges ($\dot{Q}_{edge}$) are also estimated. The model uses bond conductance to account for the thermal resistance between the water and the heat spreader. Based on initial model verifications, the model was tuned to better match performance assessment results by varying bond conductance, capacitances, and thermal and contact resistances.

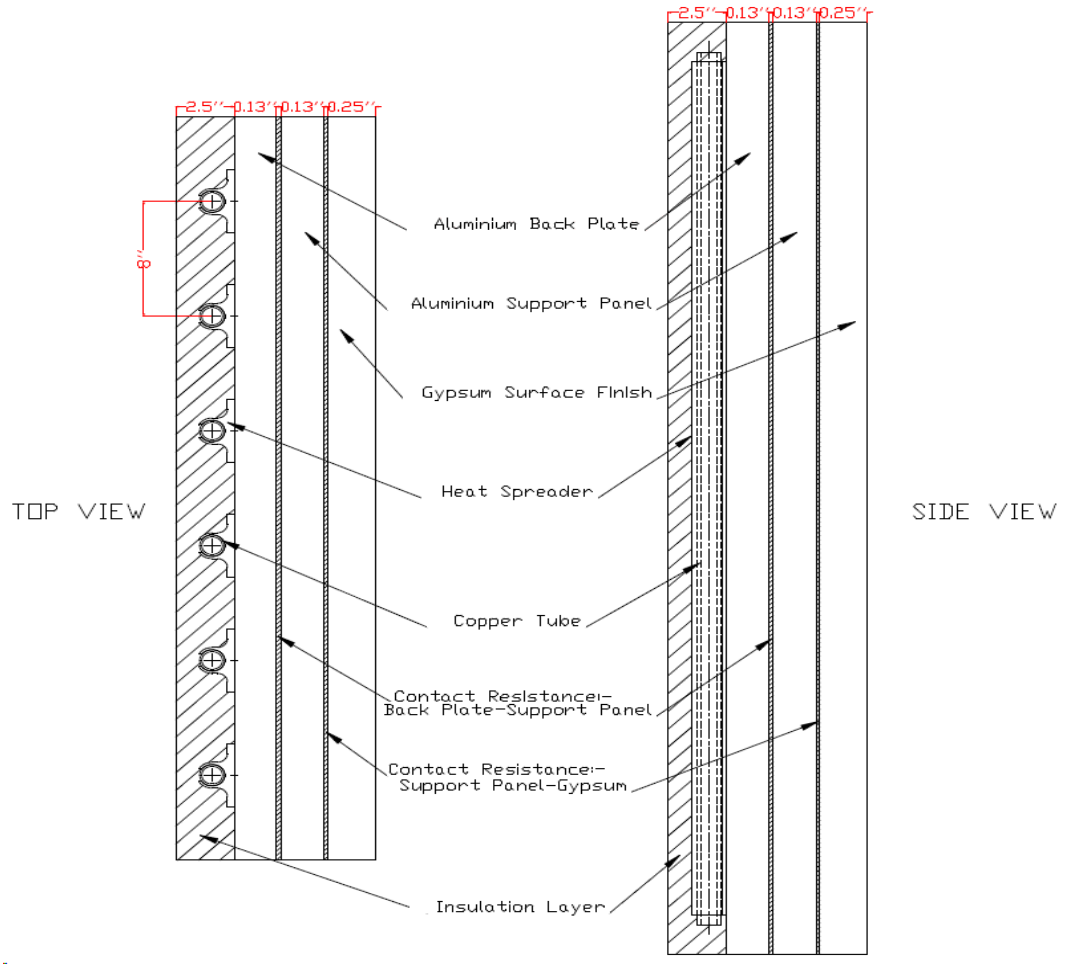

Figure 3.30 Prototype panel layers

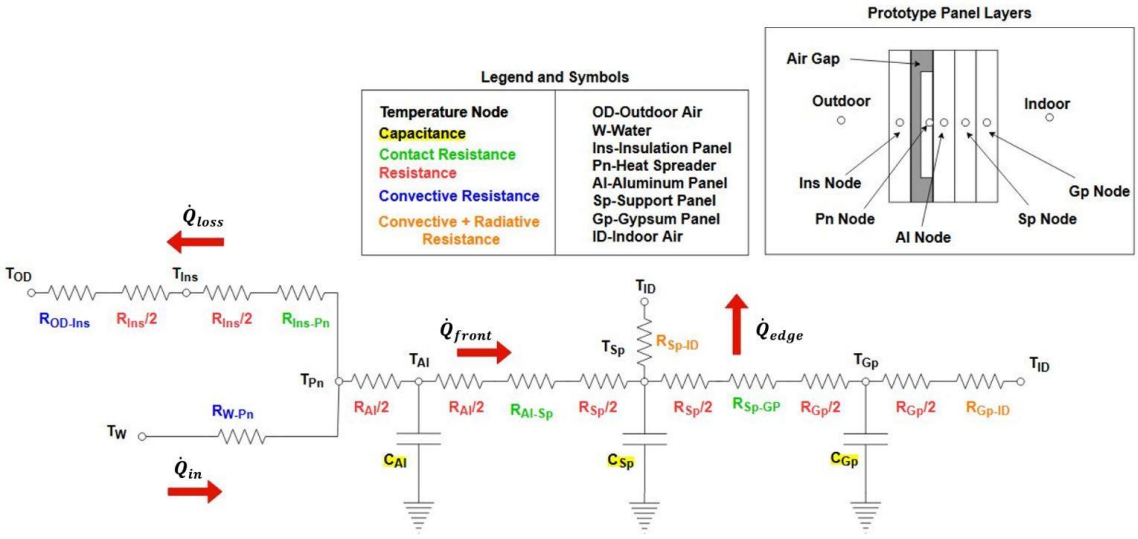

Figure 3.31 Thermal network diagram for 1-D transient numerical model

The thermal circuit of Figure 3.31 shows four main heat transfer contributions. For illustration purposes, the arrow direction shows heating case where heat transfer occurs from hot water in the tubes to the panels surface. Here, $\dot{Q}_{in}$ is the heat transfer rate between the water inside the tubes and the heat spreader node, $\dot{Q}_{front}$ is the heat transfer rate occurring between the heat spreader node and support panel node, $\dot{Q}_{loss}$ is the heat transfer rate happening between the heat spreader node and outdoor air through the insulation panel, and $\dot{Q}_{edge}$ is the heat transfer rate between support frame attached to the support panel and the indoor air. The thermal resistances (R) accounted for are thermal resistances for individual nodes (represented using red color in Figure 3.31). The values are estimated based on material properties (thermal conductivity per unit length and thickness of the respective layer). Additionally, contact resistances (R_C) between two adjacent layers (represented by green color in Figure 3.31) are also included. Furthermore, convective resistances (represented by blue color in Figure 3.31) are also involved along with two resistances accounting for combined radiative and convective heat transfer (represented by orange color in Figure 3.31) between the panel surface and indoor air, panel edges and indoor air. Lastly, to estimate the transient performance, thermal capacitances ((C) highlighted in yellow color) were added to the appropriate layers. The thermal capacitances of the heat spreader (due to its small size and mass) and insulation panel (due to its low mass density) were neglected because they were not found to significantly contribute to the transient behavior of the prototype wall panel.

The thermal network in Figure 3.31 leads to the system of equations 3.1, 3.2, 3.3, 3.4 to impose energy balances at heat spreader node (Pn), aluminum panel node (Al), support panel node (Sp), gypsum panel node (Gp), respectively. In addition, Equation 3.5 is used to close the energy balance between water, outdoor air, and the panel occurring at the heat spreader node to calculate the water outlet temperature. These equations are iteratively solved in EES (Klein, 2021) to obtain the values of temperatures at each node.

$$\frac{(T_{pn} - T_{w\,in})}{(1/C_b) + (1/(\pi D_i h_{fi}))} = \frac{(T_{Pn} - T_{OD})}{(A \cdot R_{C,Ins-Pn} + R_{Ins} + R_{OD-Ins})} + \frac{(T_{Pn} - T_{Al})}{(R_{Al}/2)} \qquad 3.1$$

$$\frac{dT_{Al}}{dt} = \frac{1}{C_{Al}} \cdot \left[\frac{(T_{Pn} - T_{Al})}{(R_{Al}/2)} - \frac{(T_{Al} - T_{Sp})}{(R_{Al}/2 + R_{Sp}/2 + (A \cdot R_{C,Al-Sp}))} \right] \qquad 3.2$$

$$\frac{dT_{Sp}}{dt} = \frac{1}{C_{Sp}} \cdot \left[\frac{(T_{Al} - T_{Sp})}{(R_{Al}/2 + R_{Sp}/2 + (A \cdot R_{C,Al-Sp}))} - \frac{(T_{Sp} - T_{Gp})}{(R_{Sp}/2 + R_{Gp}/2 + (A \cdot R_{C,Sp-Gp}))} - h_{edge} \times A_{edge} \times (T_{Sp} - T_{ID}) \right] \quad 3.3$$

$$\frac{dT_{Gp}}{dt} = \frac{1}{C_{Gp}} \cdot \left[\frac{(T_{Sp} - T_{Gp})}{(R_{Sp}/2 + R_{Gp}/2 + (A \cdot R_{C,Sp-Gp}))} - \frac{(T_{Gp} - T_{ID})}{(R_{Gp}/2 + R_{Air})} \right] \quad 3.4$$

$$\dot{Q}_{in} = \dot{m}_w \cdot c_{pw} \cdot (T_{w,out} - T_{w,in}) \quad 3.5$$

Equation 3.1 describes the energy balance at the heat spreader node ('Pn' node). The assembly of copper tubes inside the heat spreader panels is analogous to a solar flat plate collector scheme (Kalogirou, 2009). It uses a parameter called bond conductance (C_b) which essentially quantifies the thermal contact between the tubes and heat spreaders. The heat transfer coefficient between the water and tube inner surface *(h_{fi})* is evaluated using an inbuilt EES function for internal pipe flow from Nellis & Klein, (2009). The experimental setup was inside the lab space; hence the outdoor temperature (T_{OD}) and indoor temperature (T_{ID}) were essentially the bulk air temperature in the lab space. Hence it was assumed that $T_{ID} = T_{OD}$. This value was the experimentally measured indoor air temperature value at one-minute interval and was fed to the model using Lookup tables for each iteration along with the water flow rate ($\dot{m}_w$) and water inlet temperature ($T_{w\,in}$).

Equation 3.2 represents the energy balance at aluminum node ('Al' node) to calculate the time-dependent temperature gradient (dT_{Al}/dt). This was integrated numerically over the total duration of the test (*Et*) and added to indoor air temperature (T_{ID}) to calculate aluminum node temperature (T_{Al}). A similar set of energy balance and integration equations were set up at the support panel node (Equation 3.3) and the gypsum panel node (Equation 3.4) to finally calculate panel surface temperature, which is assumed to be equal to the gypsum node temperature. The equation system is closed to obtain water outlet temperature by an energy balance (Equation 3.5) between the total heat transfer rate entering the system and energy gained or lost through interaction with the cooling or heating water, respectively.

To calculate R_{Air} in Equation 3.4, convective and long-wave radiative heat transfer modes to or from the panel surface with a shared indoor condition are assumed to occur in parallel. The long-wave radiation is linearized with a view factor of unity (Bergman et al., 2011) to the surrounding surfaces (Equation 3.6). A natural convection correlation from Nellis & Klein, (2009) for a vertical

wall is employed through the EES built-in function. It uses the Rayleigh number (Equation 3.7) and an average Nusselt number (Equation 3.8) that are defined based on the length of the plate in vertical direction.

$$h_r = \varepsilon_{Gp} \cdot \sigma \cdot \left(T_{Surface}^2 + T_{ID}^2\right) \cdot \left(T_{Surface} + T_{ID}\right) \quad 3.6$$

$$Ra_L = \frac{g \times L'^3 \times \beta \times \left(T_{Surface} - T_{ID}\right)}{v \times \alpha} \quad 3.7$$

$$\overline{Nu_L} = \frac{\overline{h_c} \times L'}{k} \quad 3.8$$

The thermal resistances for each layer in the wall panel were estimated using their respective material properties and dimensions (thicknesses) of Figure 3.30. The bond conductance parameter accounts for the contact resistance between the heat spreader, tube wall, and the aluminum base panel. The thermal resistance ($R_{C,Ins-Pn}$) was basically around a 1-inch air gap between the insulation panel and the heat spreader-aluminum base plate assembly. The thermal resistance for this is air gap was 0.17 m^2-K/W taken from London Metropolitan University, (2004) and further tuned. Both aluminum base panel and support panel are 0.13-inch-thick aluminum plates that are screwed together (contact resistance - $R_{C,Al-Sp}$) and the 0.25-inch gypsum panel is pasted over the support panel (contact resistance - $R_{C,Sp-Gp}$).

First, the model was tuned to match the quasi- steady-state experimental results by tuning the steady-state parameters. These include bond conductance (C_b) between the heat spreaders water pipes, thermal contact resistances between the layers ($R_{C,Al-Sp}$), ($R_{C,Sp-Gp}$), ($R_{C,Ins-Pn}$) and the combined edge loss coefficient (h_{edge}), the reciprocal of which is the resistance between the panel edges and indoor air (R_{Sp-ID}). An error function was set up using Equation 3.9 and the cumulative error ($Error_{SS}$) for eleven steady-state data points was minimized using Genetic algorithm optimization function in EES (Klein, 2021). Badran et al., (2008) experimentally measured and theoretically analyzed the bond conductance between an absorber plate and the tube of solar collectors from different manufacturers. The values ranged from 2 W/(m-K) to 6 W/(m-K) and were used as lower and upper bounds in the optimization function. The initial guess values for contact resistances were selected from Nellis & Klein Sanford, (2009). The edge loss coefficient guess was selected from (Koca & Cetin, 2017). The optimum values obtained for a minimum cumulative error are summarized in Table 3.2.

$$Error_{SS} = \left(\sum_{i=1}^{11} \left[\sqrt[2]{\left(T_{Al,Expt,i} - T_{Al,Model,i}\right)^2 + \left(T_{Surface,Expt,i} - T_{Surface,Model,i}\right)^2} \right] \right)^{1/2} \quad 3.9$$

Table 3.2 Results of minimization of error for steady-state parameters

$Error_{SS}$ [°C]	C_b [W/m-K]	h_{edge} [W/m^2-K]	$R_{C,Al-Sp}$ [m^2-K/W]	$R_{C,Sp-Gp}$ [m^2-K/W]	$R_{C,Pn-Ins}$ [m^2-K/W]	Function Calls	Generation
3.018	4.18	9.86	0.016	0.02	0.18	4234	64/64

Panel surface temperature values ($T_{Surface}$) and aluminum backplate temperatures (T_{Al}) were measured for different water inlet temperatures corresponding to the mixing valve opening percentages (0%, 30% to 65%, 85%, 100%). The $T_{Surface}$ and T_{Al} values obtained at steady-state were plotted against the respective water inlet temperature values in these tests and overlaid on the quasi-steady-state numerical model predictions calculated at the same water inlet conditions and water flow rates using the values of optimized parameter in Figure 3.32 and Figure 3.33. The model and experimental results lie within ±1°C as reported by Mean Absolute Error (MAE) in the plots.

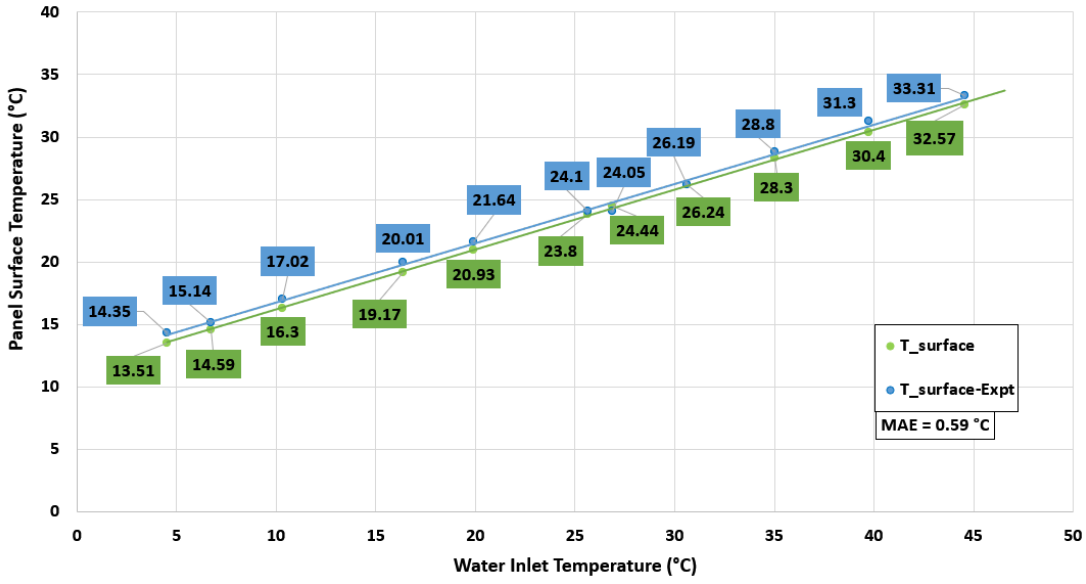

Figure 3.32 Panel surface temperature steady-state model vs experiment results

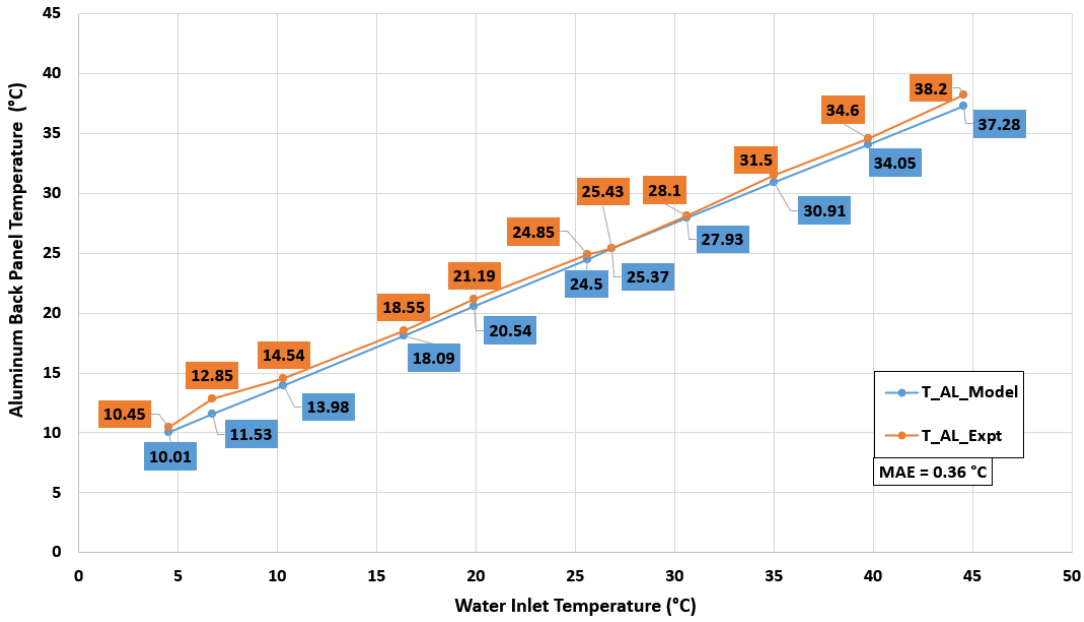

Figure 3.33 Al. back-plate temperature steady-state model vs experiment results

For transients, the thermal capacitance values (C_{Al} , C_{Sp} C_{Gp}) were calculated using the material properties. But to match the panel's dynamic response, these values were further tuned by adding multiplication factors (λ_1, λ_2, λ_3). These factors were bounded between 0.7 and 1.2, and a genetic optimization algorithm was utilized to minimize the error. The error function in Equation 3.9 was used but this time with a 140-minute performance assessment test data to calculate error ($Error_{TR}$) at each time step. After minimization, the values obtained are (λ_1=1.117, λ_2=1.167, λ_3=1.194). Using these multiplication factors, the transient simulation dataset was obtained.

The key outputs of the model are panel surface temperatures and aluminum backplate temperatures obtained for each time step (every minute), along with heat convective and radiative heat transfer coefficients, panel water outlet temperature, and heat transfer rates. Figure 3.34(a) shows the panel surface temperature results from the tuned model (T_{Model}) and experiments (T_{Expt}). Model results are within 0.5°C of the experimental results throughout the test interval. Similarly, Figure 3.34(b) shows the aluminum backplate temperature results ($T_{Al,Back,Model}$) overlaid on experimental results ($T_{Al,Back,Expt}$). In this case, the model and experimental values differences are slightly higher, about 1°C, at both cooling and heating steady-state. This is because the steady-state data used for steady-state parameters is different than the transient experimental data used for the

plots below. Additional validation tests were performed on the prototype at different operating conditions showed the model vs. experimental plots acceptable within limits too.

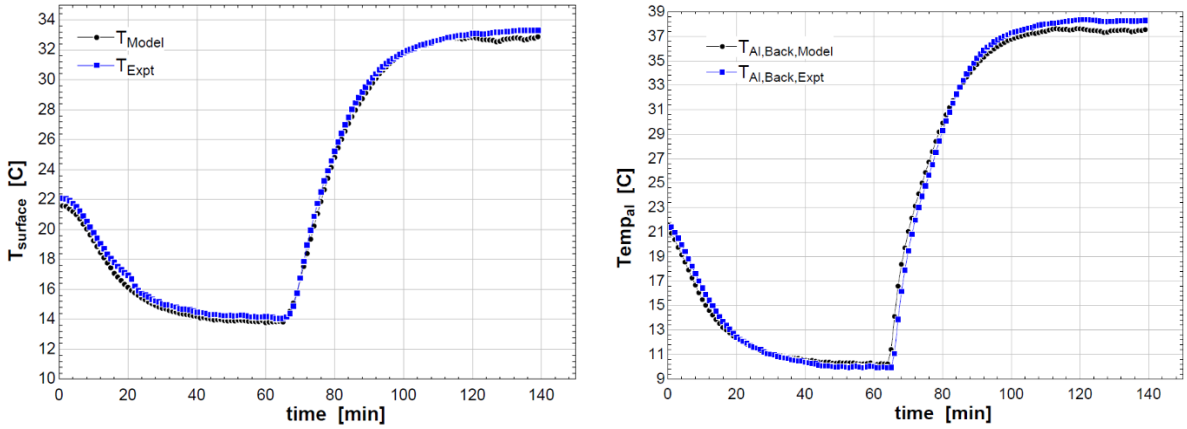

(a) Panel surface temperatures (b) Aluminum back-plate temperatures

Figure 3.34 Comparisons of the model and experimental results

3.4 Final Panel Design and Testing

A new prototype panel as per the final design modifications in Section 3 was constructed by Bridgewater Studio and was delivered to evaluate final construction and design. Figure 3.35(a) shows the complete assembly of the structure with drywall surface treatment panels in the front. Figure 3.35(b) shows a rear view with an insulation panel and hydronic piping outlets. It consists of a steel frame on which aluminum base panels are mounted, as shown in Figure 3.36 (top panel with diffuser slots) and Figure 3.37 (bottom panel with guide slots). The base panel has eight slots for eight magnets on surface treatment panels. A thin layer of thermal paste was added to the base panel to reduce the air gap between the base panel and surface treatment panel. Figure 3.38 shows a ceiling panel with a commonly used drywall acoustic tile finish, and Figure 3.39 shows a floor panel with plywood having a floor-tile-like finish that was delivered for testing. This section covers detailed test results for all these surface treatments evaluating their performance limits in terms of maximum and minimum achievable surface temperatures and cooling/heating transient response.

(a) Front view with drywall surface treatment (b) Rear view with insulation panel

Figure 3.35 New prototype panel

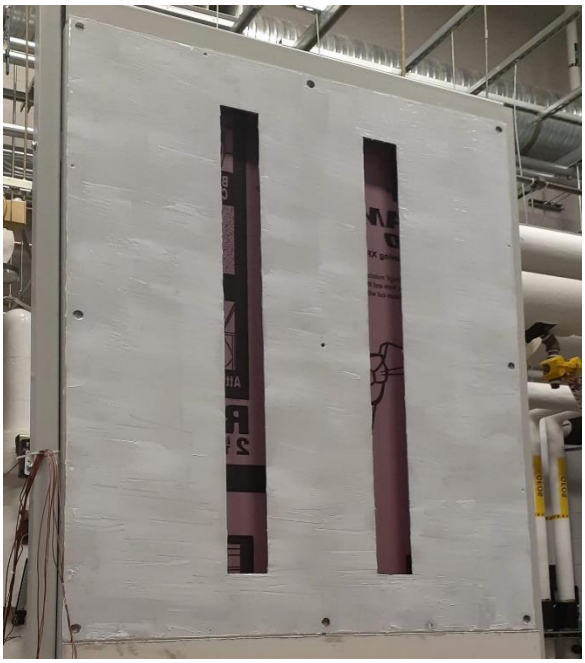

Figure 3.36 Aluminum base panel with full cut diffuser slots in steel frame

Figure 3.37 Aluminum base panel with guide slots in steel frame

Figure 3.38 Floor surface treatment panel (Plywood)

Figure 3.39 Ceiling surface treatment panel (Drywall acoustic tile)

The top and bottom panels were connected in a series configuration with the mixed water from the 3-way mixing valve supplied to the bottom panel first and its outlet connected to the inlet of the top panel. At the outlet of the top panel, there was a diverting valve to split the hot and cold water flow in proportion to the mixing valve. This configuration would decrease the number of 3-way valves by half, hence simplifying the control and piping. However, for this to work, the average surface temperatures of both the top and bottom panel should be within 1°C. Thermal images of aluminum base panels were taken at extreme heating and cooling steady-state operating conditions to test this. Using a thermal image post processing software, the images were marked with spots and a rectangular surface area to capture the average temperatures. Figure 3.40(a) and Figure 3.40(b) show the thermal images of the aluminum base panel in heating at steady-state. It can be observed from the measurements box that the average temperature of the top panel is 35.5°C, and the bottom panel is 34.5°C at a steady-state extreme heating case.

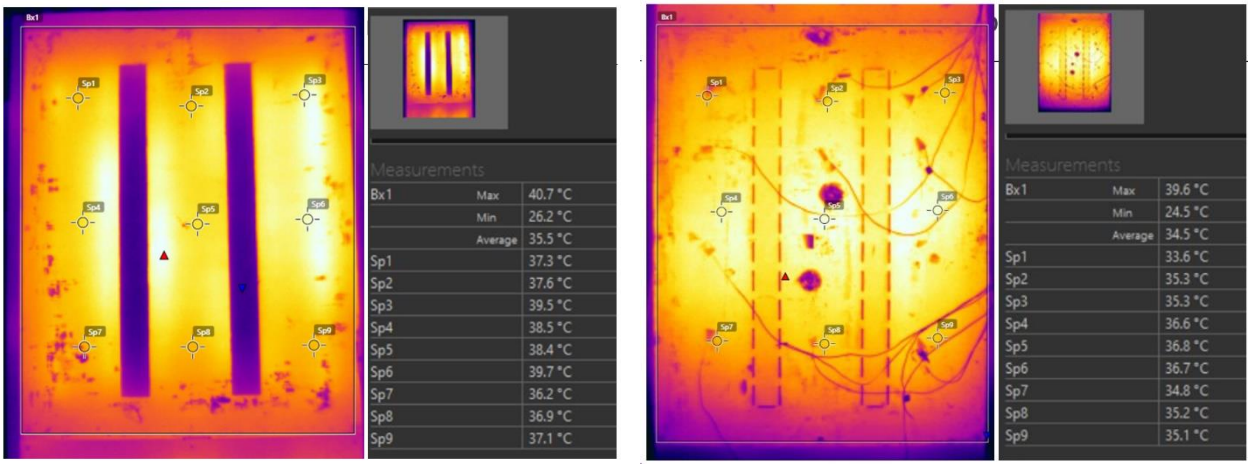

(a) Top panel (b) Bottom panel

Figure 3.40 Aluminum base panel heating steady-state thermal image

Similarly, Figure 3.41(a) and Figure 3.41(b) show thermal images of the aluminum base panel for steady-state cooling. It can be observed that the average surface temperature of the top panel is 14.7°C, and the bottom panel is 13.9°C. In both these cases, the top and bottom panel surface temperatures lie within the target 1°C range. Hence, the series configuration was finalized for further tests and the HBIL final design.

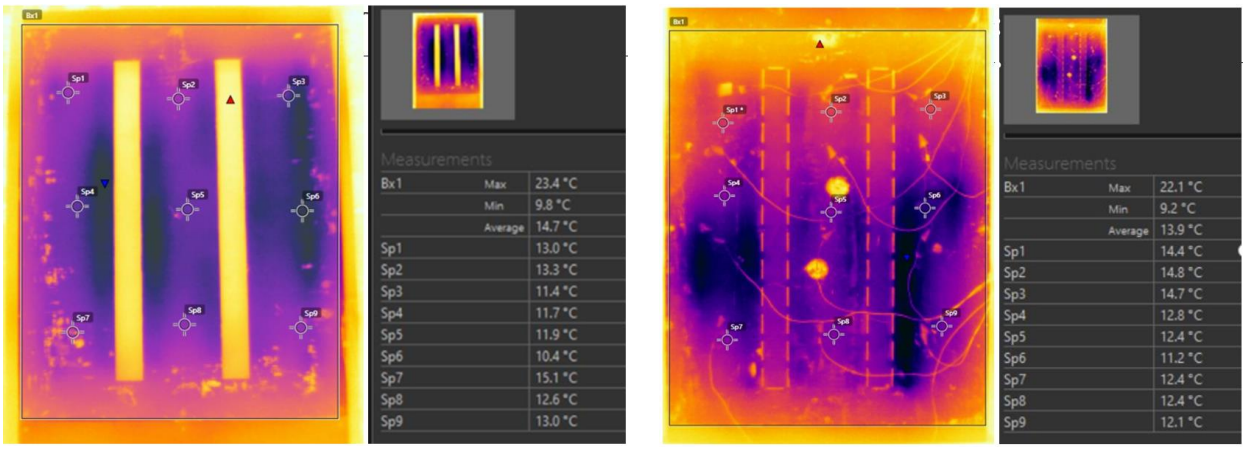

(a) Top panel (b) Bottom panel

Figure 3.41 Aluminum base panel cooling steady-state thermal image

Following this, different surface treatments were tested for performance limit assessment. A general test procedure involved an extreme cooling case where chilled water of 4°C to 5°C was maintained at the hydronic loop inlet until the surface temperatures reached a cooling steady-state. This was followed by an extreme heating case where the hot water temperature was maintained between 43°C to 45°C until the heating steady-state was reached. During the test, the head pressure of cold and hot water was maintained between 27-29 psi, which provided a water flow rate of 0.85 to 1.2 GPM for the cooling and heating cases. 6 thermocouples were mounted on the surface of the panels. Water inlet and outlet temperatures, water flow rate, aluminum back panel temperature, and differential pressure across the inlet and outlet were monitored throughout the tests.

3.4.1 Drywall Panel Testing

Two drywall panels of different thicknesses (1/4" and 3/8") were evaluated. Both of these wall panels had a miniature thermocouple sensor (Figure 3.27) embedded inside the panels to measure the surface temperature. In the first configuration, the drywall panel with 3/8" thickness was mounted on the bottom base panel, and the 1/4" panel was mounted on the top base panel. In the second configuration, the drywall panels were swapped, i.e., the 1/4" panel was mounted at the bottom, the 3/8" panel was mounted at the top.

The design surface temperature targets were 15.5°C for cooling and 26.7°C for heating. The average panel surface temperature for both the panels was observed to be around 15°C for steady-state cooling and 30°C for steady-state heating. Hence, both panels satisfied the design targets. As

expected, the 1/4" panel showed better performance than the 3/8" panel because of the lower thermal resistance. However, both panels showed non-uniform surface temperature distributions. This variation in performance and non-uniform surface temperature distribution can be seen more clearly in Figure 3.42(a) and Figure 3.42(b), which are steady-state thermal images for both configurations—cooling on the left and heating on the right. The reason for the non-uniformities is heat loss from the edges of the panel and a potential air gap between the surface treatment and base panels in non-contact areas, mostly observed at the center. The edge losses will be less significant in the facility where multiple surface treatments will be next to each other. Also, there is a scope for improving the surface-to-surface contact by increasing the thermal paste coating thickness or adding magnets in the center location for better contact. It was decided to use a PTFE insulation tape between the base panel and steel structure to break the thermal bridge.

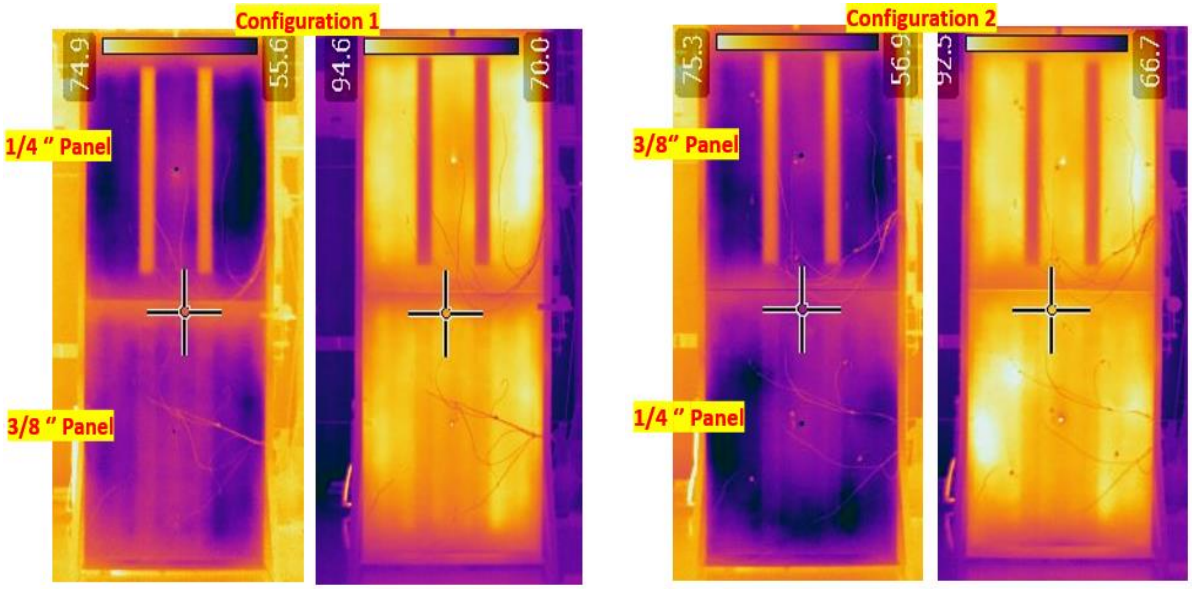

(a) Configuration 1 (b) Configuration 2

Figure 3.42 New drywall panel thermal image

Furthermore, it was observed that the embedded sensor read 1.5 to 2°C off the average temperature read by the thermocouples attached to the surface. The thermocouples on the surface were in direct contact with the ambient air and affected by radiation. The embedded thermocouple also had an exposed surface on the rear side and was influenced by direct contact with the aluminum base panel. Hence, it was decided to use a welded tip thermocouple. However, from the tests in Section 3.2.4 it is evident that this sensor will also not be an accurate measurement of the surface

temperature. Hence for the facility, based on experimental data, a specific offset will be provided for the value measured by this sensor.

3.4.2 Ceiling Panel Testing

Two magnets were added in the central area of ceiling panels as described in Section 0 to improve the surface contact and eliminate the air gap. The ceiling panel was tested on the bottom base panel using the same method as drywall panels, and the test results are reported in Figure 3.43. The test results show an average surface temperature of 18°C, which is 3.5°C higher than the target design temperature for steady-state cooling. For steady-state heating, the average panel surface temperature was observed to be around 27°C, just meeting the design temperature target. The worse performance for the ceiling panel compared to the wall panel with drywall is because the ceiling panel material has a very high thermal resistance and is porous. However, the overall surface temperature distribution looks better than for the wall panel results. This result is because of the center magnets. Similar conclusions can be drawn from the thermal image for the steady-state cooling in Figure 3.44(a) and the steady-state heating in Figure 3.44(b), respectively.

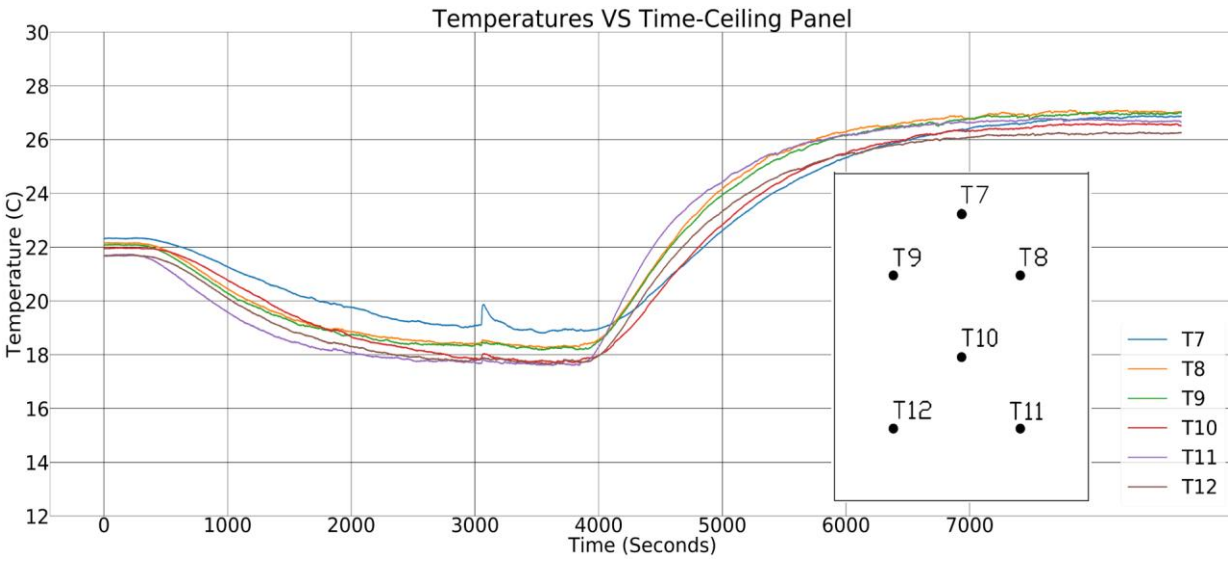

Figure 3.43 Ceiling panel surface temperature test results

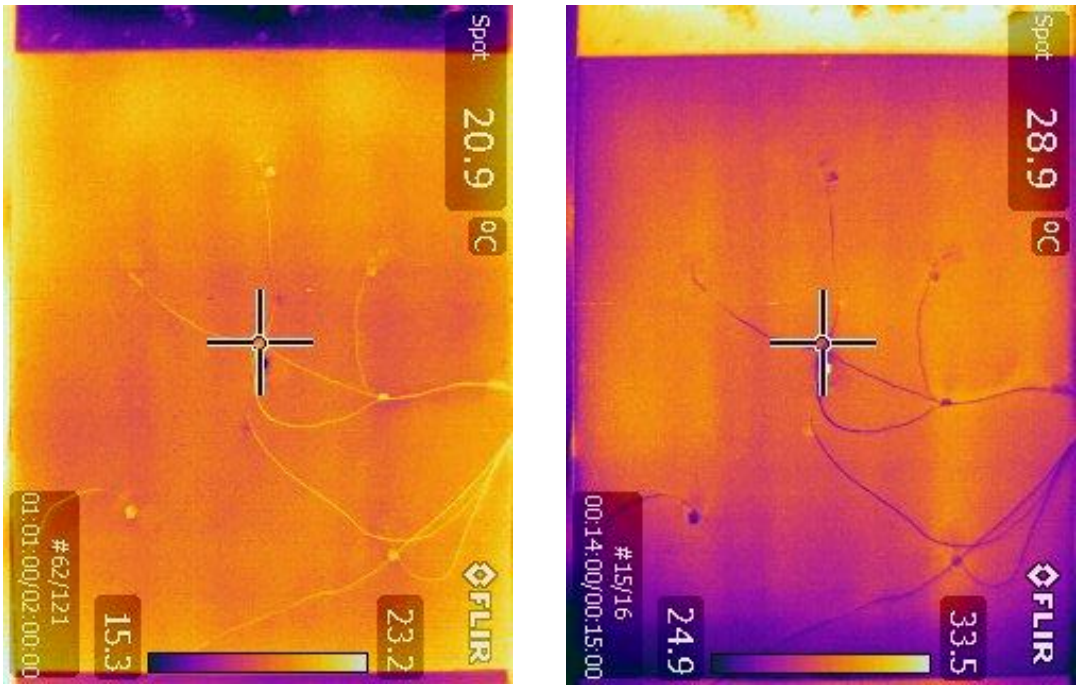

(a) cooling steady-state (b) heating steady-state

Figure 3.44 Ceiling panel (acoustic tile) thermal image

3.4.3 Floor Panel Testing

The floor panel is the heaviest of all the panels. It has a base layer made of plywood and finish-wood tiles on the front like a typical floor. While handling and changing surface treatments, the panel was slightly bent at some locations. The new magnets held the panel in the right place, but the attachment was not uniform across the base panel surface due to these bends and heavyweight. Hence clamps were used for attachment in addition to magnets in order to eliminate the non-contact area due to the bends.

Figure 3.45 shows test results with surface temperatures plotted as a function of time. It is evident from the plot that the floor panel (wood) took a longer period to reach a steady-state (approximately 30 minutes extra). However, the surface temperatures for both the cooling and heating cases exceed the design temperature targets. Figure 3.46(a), Figure 3.46(b) show steady-state thermal images for steady-state cooling and heating, respectively. The non-uniform contact is clearly reflected through the non-uniform surface temperature distributions seen in these images. Hence, plywood was not a good choice for floor panels, primarily due to heavyweight and tendency to bend, causing non-uniform surface temperature distribution.

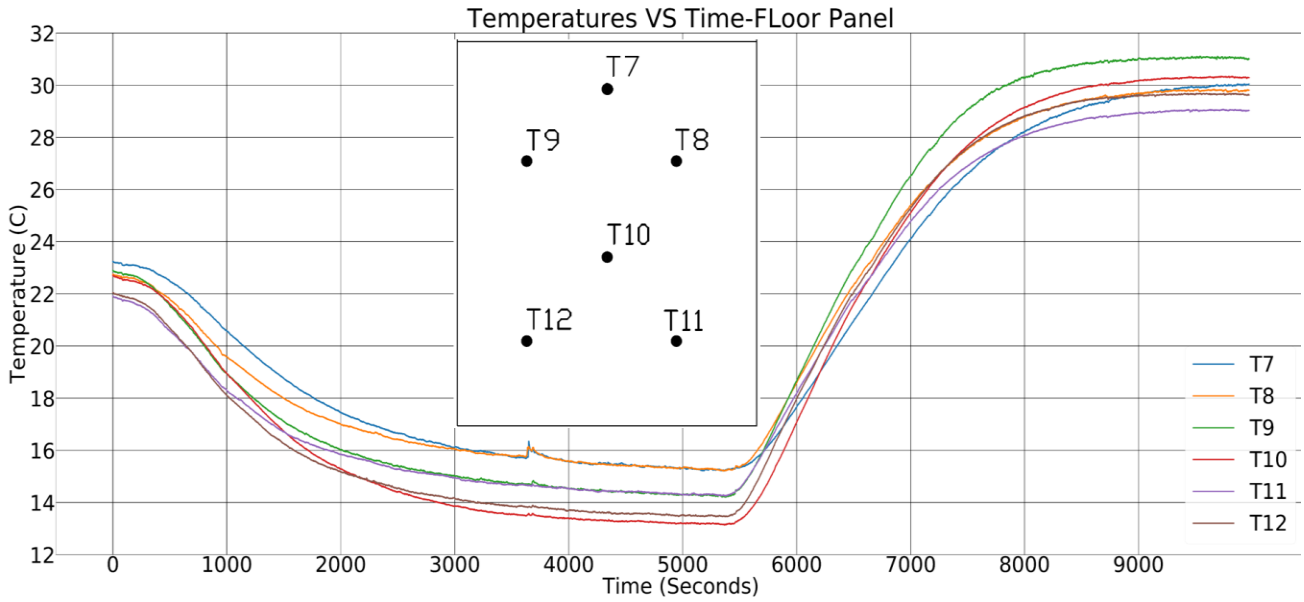

Figure 3.45 Floor panel surface temperature test results

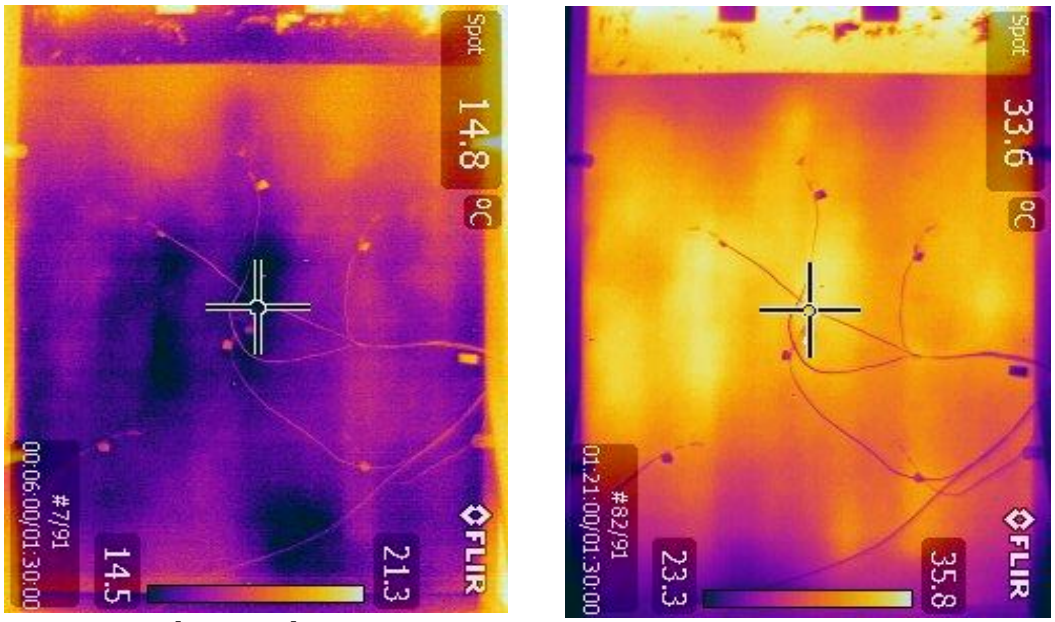

cooling steady-state (b) heating steady-state

Figure 3.46 Floor panel (plywood tile) thermal image

3.4.4 Investigation of Surface Treatment Attachment Method

Surface treatment panels are attached to the base panels using magnets. Originally, the magnets were glued to the surface treatment panels (see Figure 3.47) at 8 locations. All these magnets were then attached in their respective slots on the base panel, magnetically sticking on the

steel base frame through these slots. This attachment worked reasonably well for drywall panels due to their lighter weight. However, while changing surface treatment panels, they often detached from the panels and got stuck in the holes, the prime reason being the stronger magnetic pull than the glue's strength. This issue was more common in the ceiling and floor panels as they were heavier than the drywall panels (see Figure 3.48). The magnet locations were around the panels' edges, as shown in Figure 3.49. Hence, there was nothing to hold the panel at its center, which is unacceptable. Two additional magnets were added to the surface treatment panels at the center location to tackle this issue, as shown in Figure 3.50. It involved nut-bolt fastening by using a magnet with an unthreaded hole, as shown in Figure 3.51. This new design was tested with ceiling and floor panels as described in Section 3.4.2 and Section 3.4.3. Figure 3.52 shows the new through-hole magnet attachment using a screw and nut.

Figure 3.47 Magnet glued to the surface treatment panel

Figure 3.48 Magnets stuck in the slot hole in base panel

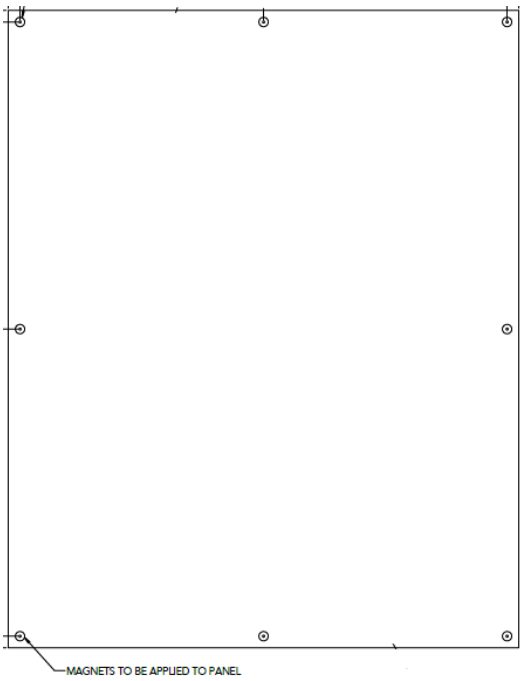

Figure 3.49 Magnet locations-8 magnets along the edges

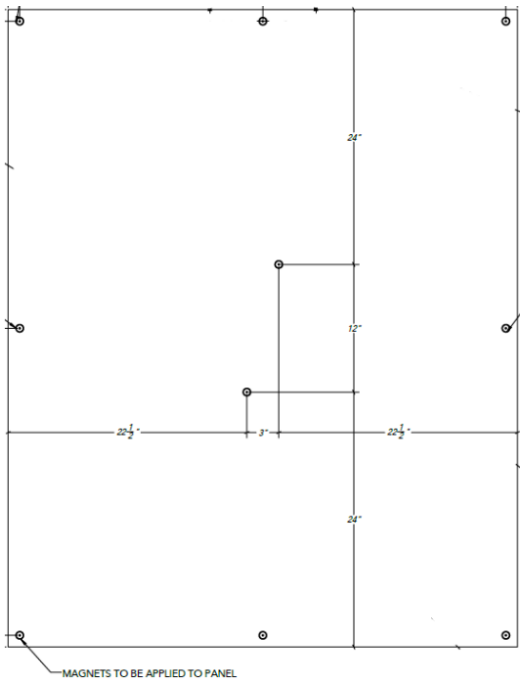

Figure 3.50 Magnet locations-2 magnets added at the center

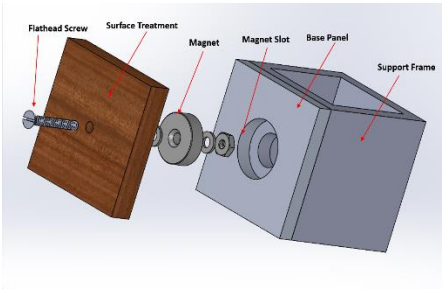

Figure 3.51 New magnet attachment method tested on floor, ceiling panels

Figure 3.52 Through-hole magnet with screw and nut attachment

Adding new magnets at the central location improved temperature distribution and better contact in the central region. However, a significant amount of surface area of the steel on which the magnet rests was reduced due to the through hole for accommodating the nut and screw. This decreased the pull strength of the magnet. Proceeding with this design for the HBIL would have involved drilling hundreds of these through holes which would be labor and cost-intensive and would also lead to alignment issues due to close tolerances. Consequently, a threaded magnet is used for

the final design, as shown in Figure 3.53 . It does not require the nut to hold it, eliminating the steel support frame holes. Also, 4 additional magnets were added in a relatively symmetric layout to increase the overall pull strength and improve the surface contact. Figure 3.54 shows the new magnet locations.

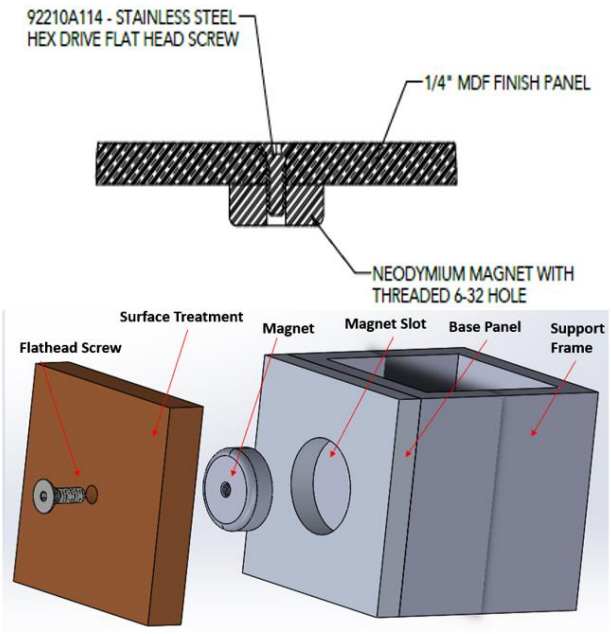

Figure 3.53 Final surface treatment attachment

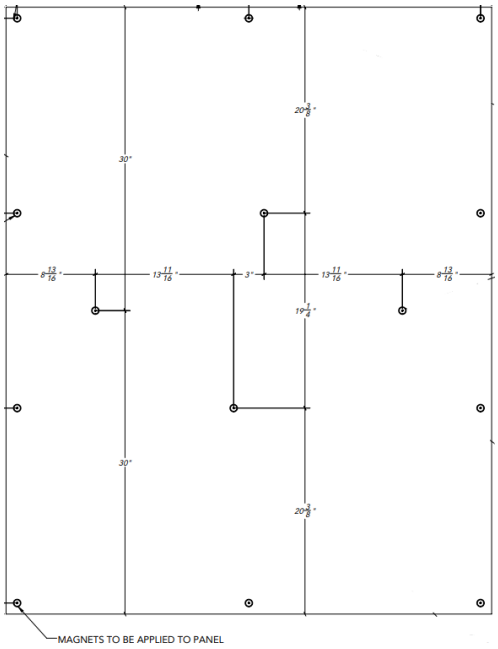

Figure 3.54 Final magnet locations

3.4.5 Final Panel Material and Design

Based on the analyses conducted, the drywall panels showed acceptable thermal performance; however, they tend to chip off and break during removal due to their layered structure. This was because the pull strength of the magnet overpowered the rigidity of the drywall panel. The acoustic tile panels for the ceilings did not satisfy the target temperature specifications. The plywood floor panels were too heavy and tended to bend, thereby showing non-uniform surface contact. As an alternative, Medium Density Fiberboard (MDF) panels were tested. MDF is rigid enough to not deform because of magnets, lightweight, and thermal conductivity close to drywall material. Three MDF samples of 1 ft^2 surface area and 0.25'' thickness each were delivered by Bridgewater Studio for testing. Figure 3.55(a), Figure 3.55 (b), Figure 3.55(c) show MDF samples with different faux color finishes for the walls, ceiling, and floor that Bridgewater Studio provided for testing.

(a) Wall sample (b) Ceiling sample (c) Floor sample

Figure 3.55 New MDF samples with faux color finish

The wall and ceiling samples were tested on the prototype panel test setup. Figure 3.56(a) and Figure 3.56(b) show the wall panel and ceiling panel mounted on the aluminum base panel after removing the thermal paste layer. These panels were attached to the base panel using aluminum duct tape. Both had 3 thermocouple sensors on the surface to measure surface temperature variation. Thermocouple T6 was attached between the guide slots to study the effect of cuts in the base panel on surface temperature. In contrast, thermocouple T3 was attached over a region without slots to study the contrast. Note that the floor panel sample was also an MDF sample, so it can be assumed that it would perform very close to either the ceiling or wall panel sample at the same experimental conditions.

A typical performance assessment test was conducted for both the wall and ceiling samples. First, 100% chilled water at around 4°C was circulated through the piping at the panel back until steady-state conditions were achieved, followed by 100% hot water at around 45°C. Thermal images were also taken to observe the transients and for comparison with thermocouple values. Figure 3.57 shows the MDF wall panel sample test, and Figure 3.58 shows the MDF ceiling panel sample test results.

(a) MDF wall sample (b) MDF ceiling sample

Figure 3.56 Performance limit assessment test for MDF samples

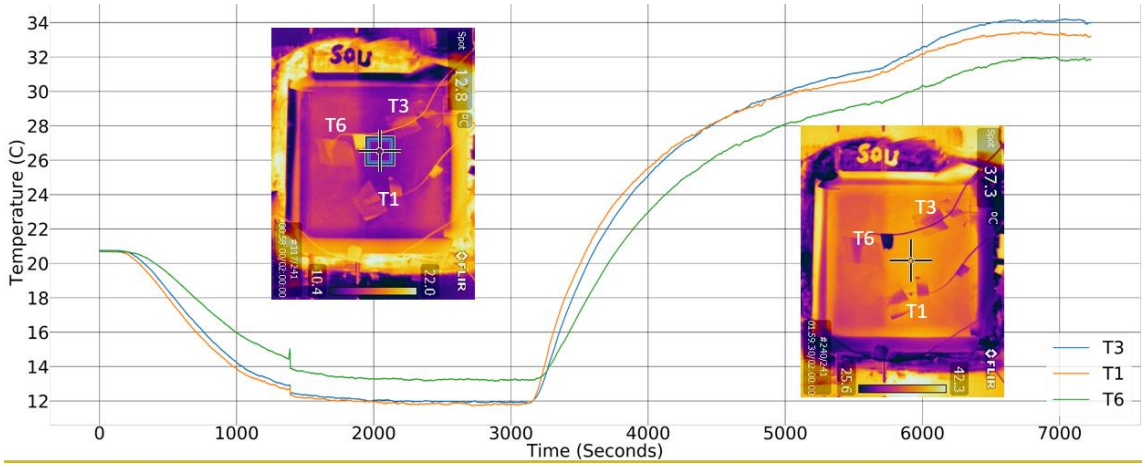

Figure 3.57 MDF wall panel sample test results with steady-state thermal images

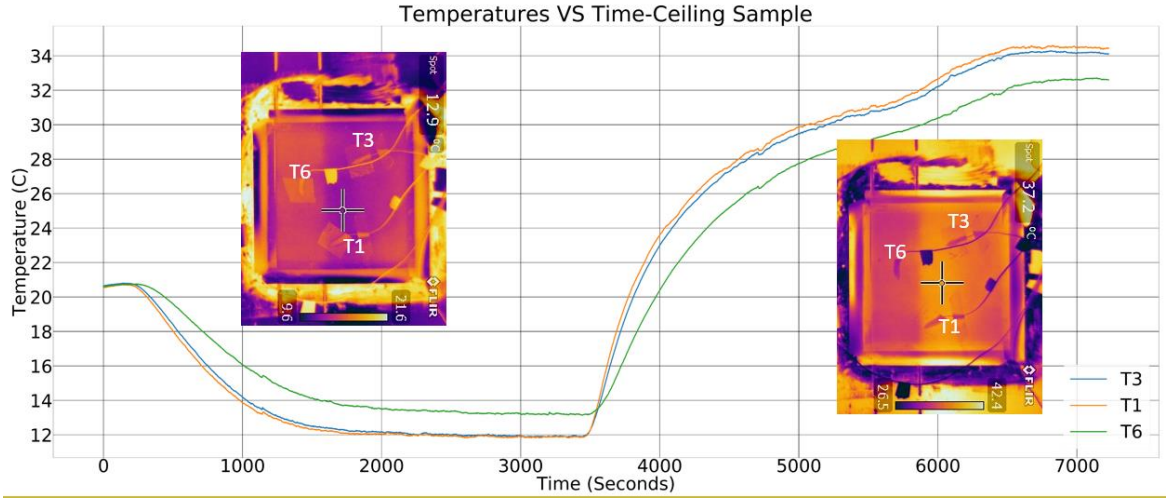

Figure 3.58 MDF ceiling panel sample test results with steady-state thermal images

The test results showed that the average panel surface temperature for both the wall and ceiling panels was around 13°C for steady-state cooling and 33°C for steady-state heating. Hence, both panels satisfied the target design range. It can also be inferred from the steady-state thermal images and the T6 measurements that the region between the guide slots is warmer in cooling and cooling in heating because of the heat transfer occurring through the slots in the base panel. Also, having the same material for the wall, ceiling, and floor surface treatment panels makes the design consistent. Hence, MDF with faux finishes was selected as the final material for the HBIL surface treatments.

4. HBIL DESIGN, INSTALLATION AND COMMISSIONING PLAN

4.1 HBIL Envelope Final Design and Construction

Due to the large size, design requirements, and complexity involved, the construction of the HBIL was outsourced to a third-party firm based in Chicago, IL. As mentioned in Section 2.1, Bridgewater Studio was responsible for designing the facility based on input from the Purdue HBIL team and installing it at the Herrick Labs. An overview of key design features of the HBIL was presented in Section 2.3. Based on these features, prototype panels were developed, tested, and improved. This led to multiple iterations of design drawings and a finalized design.

Figure 4.1 shows the front elevation view of the final design of the HBIL facility. The whole structure is mounted on a screw jack to level the floor. There is an 18-inch clearance under the facility for plumbing. Figure 4.2 shows a view of the ceiling panels with standard slots for lighting fixtures and air diffusers. Figure 4.3 shows a floor view that also has diffuser slots only on the base panel to test underfloor ventilation in the future, if necessary. Figure 4.4 is a detailed sectional view showing the assembly of all the panels in the base structure. The steel support frames are bolted together, and the base panel is screwed to the base frame on which the finish panel is attached using magnets. From the outside, the insulation panel is screwed to the base frame bracket using wing nuts for easy removal, if required.

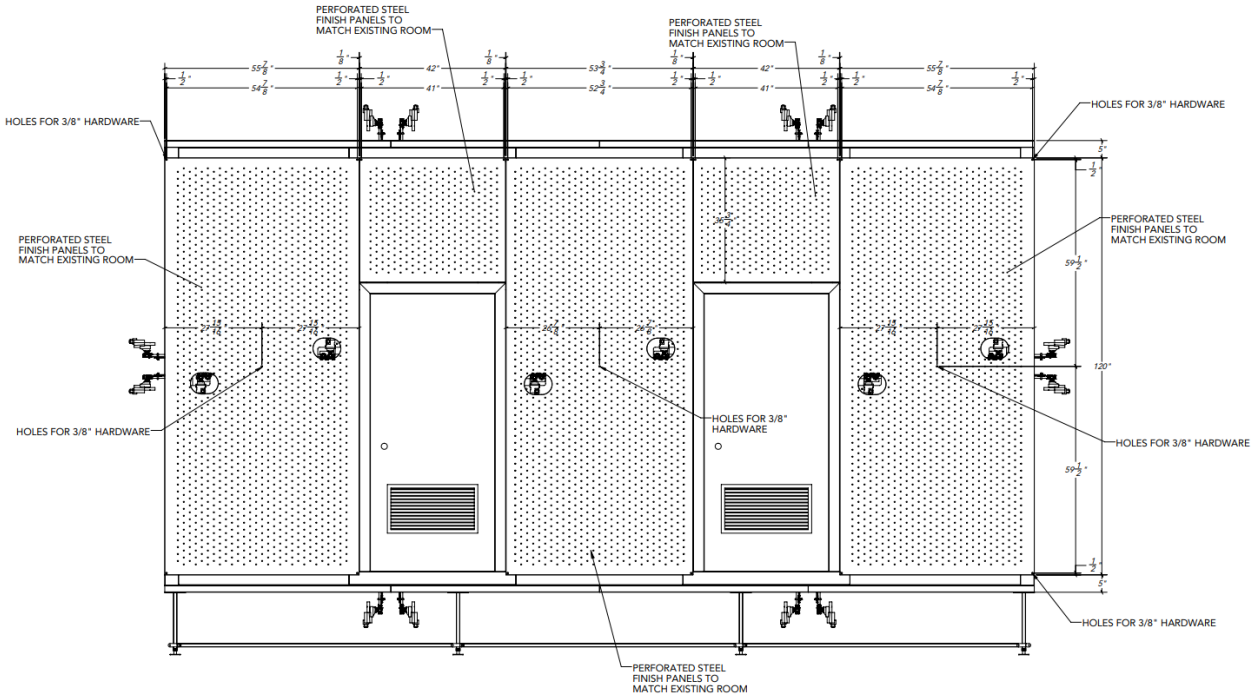

Figure 4.1 HBIL - front elevation view

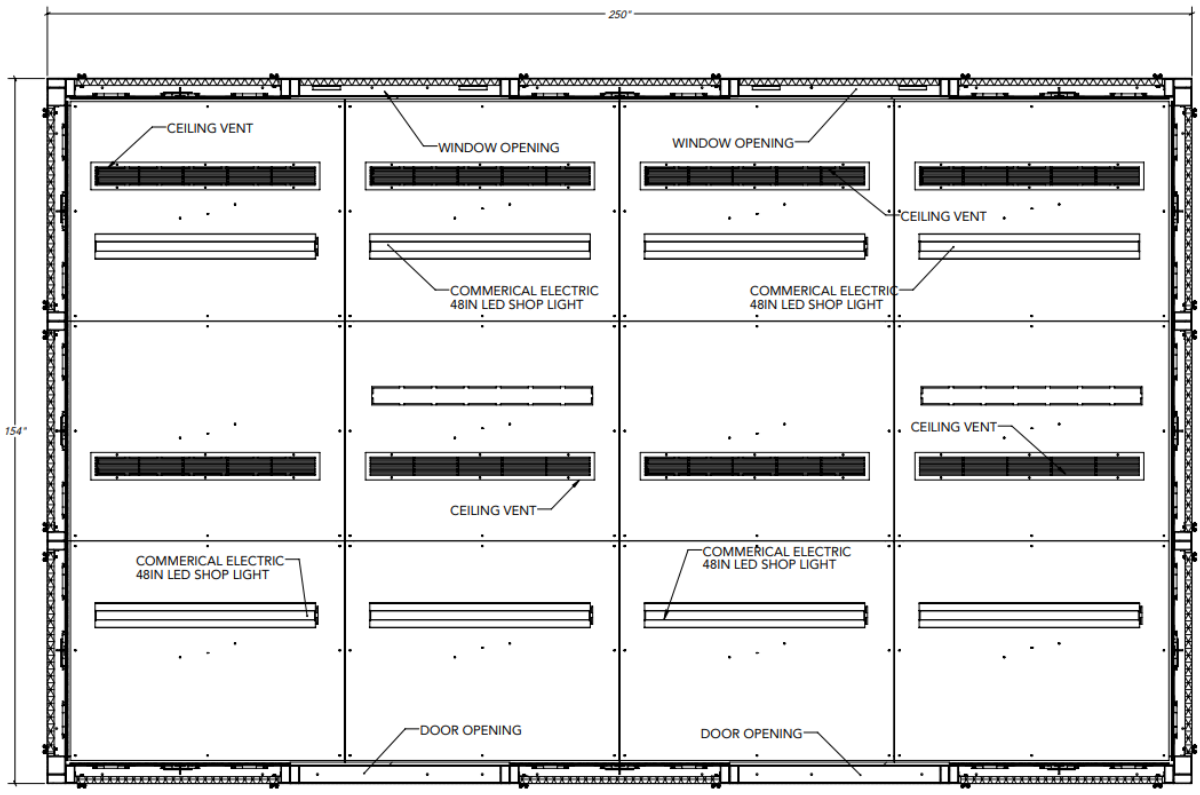

Figure 4.2 HBIL - ceiling view with electrical and air diffuser slots

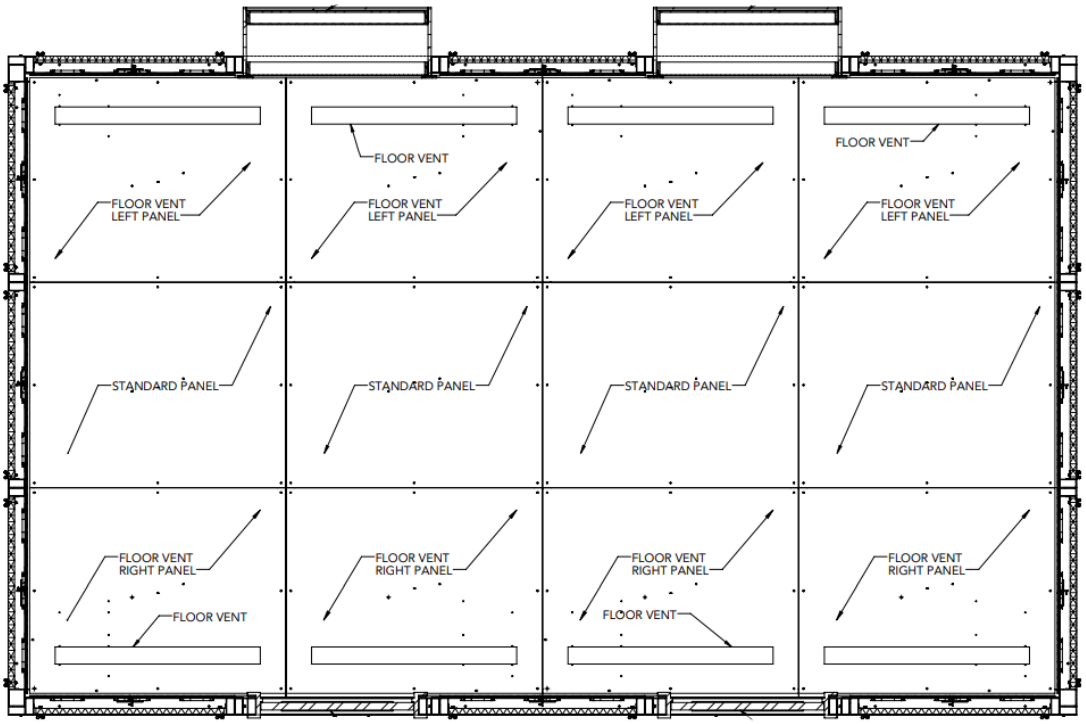

Figure 4.3 HBIL - floor view with optional air diffuser slots

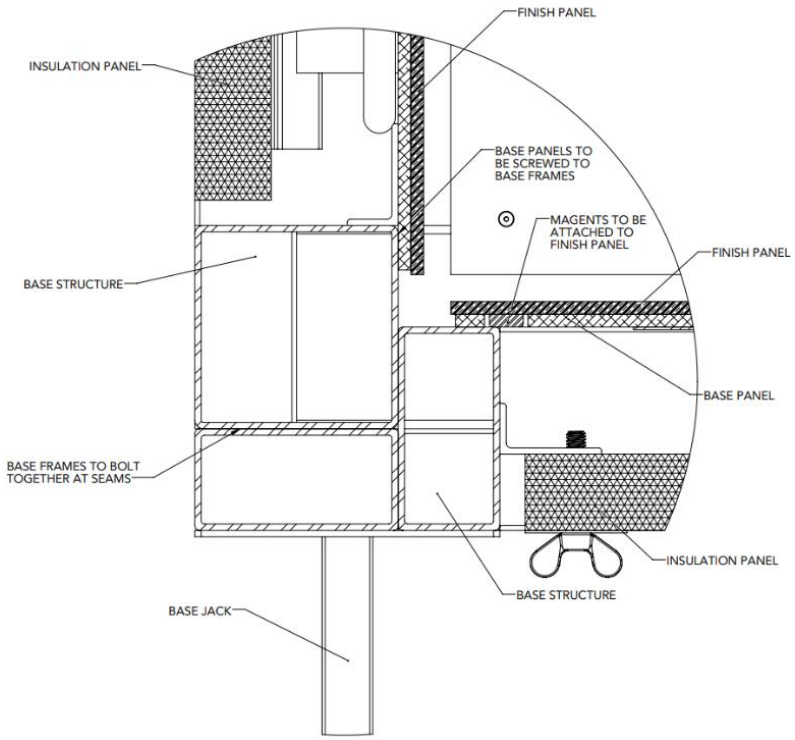

Figure 4.4 HBIL - detailed sectional view of thermo-activate panel assembly

Figure 4.5 shows a detailed rear elevation view of the base panel with hydronic piping sitting in heat spreaders. It also shows magnet holes and support plates for center magnets, along with a thermocouple sensor and T channel for support. The windows of the HBIL do not align perfectly with the PBE windows. Figure 4.6 shows the exploded view of a window lighting and conditioning box with an LED panel that is used to mimic a standard closed window. This box gives a visual effect similar to a bay window from a visual perspective. Also, the temperature of the windowpane will be controllable by adding a heating/cooling system to emulate the effect of different ambient conditions on window surface temperature and its radiative effect on human comfort. Additional drawings are shown in Section 2.3 and in the Appendix.

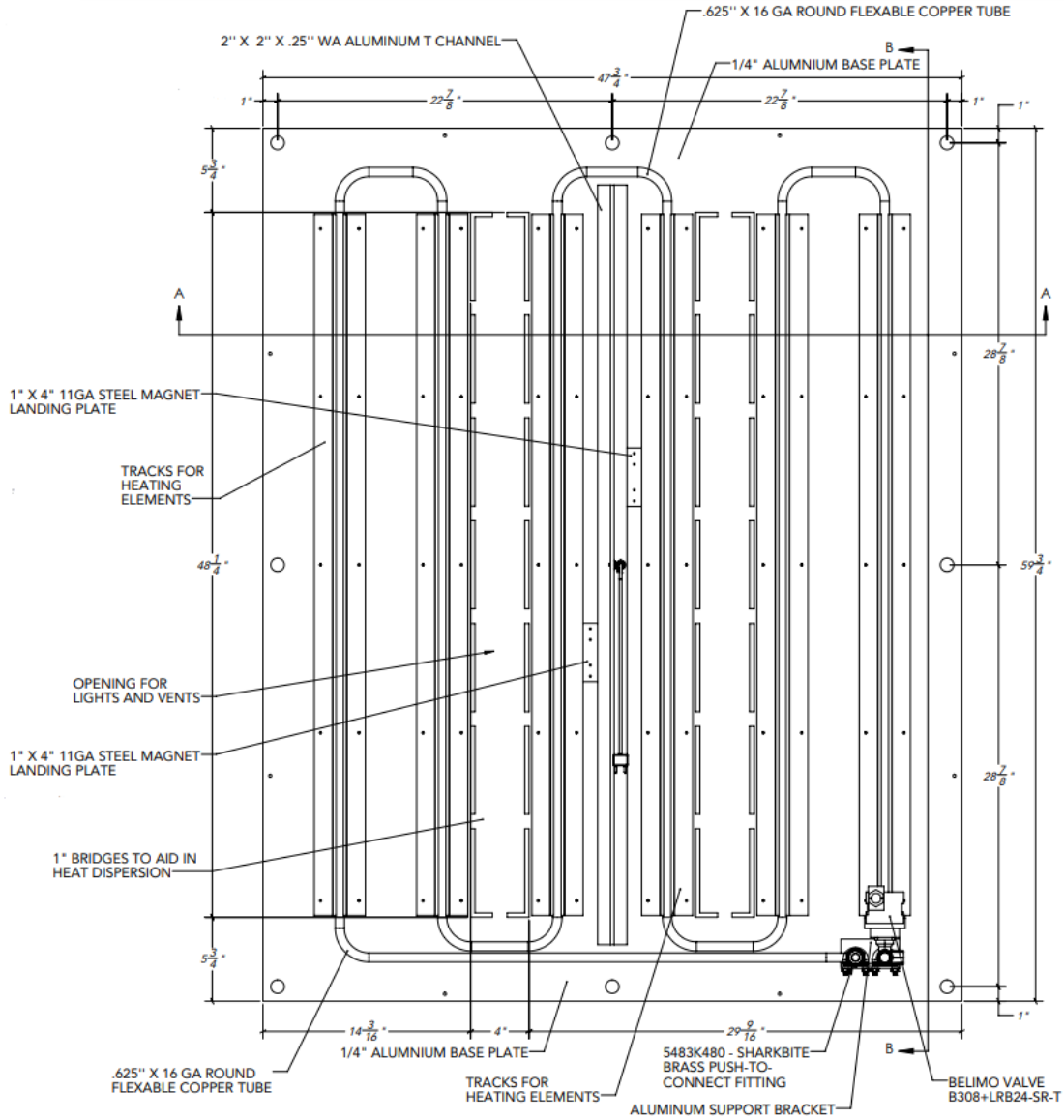

Figure 4.5 HBIL - rear elevation view of aluminum base panel

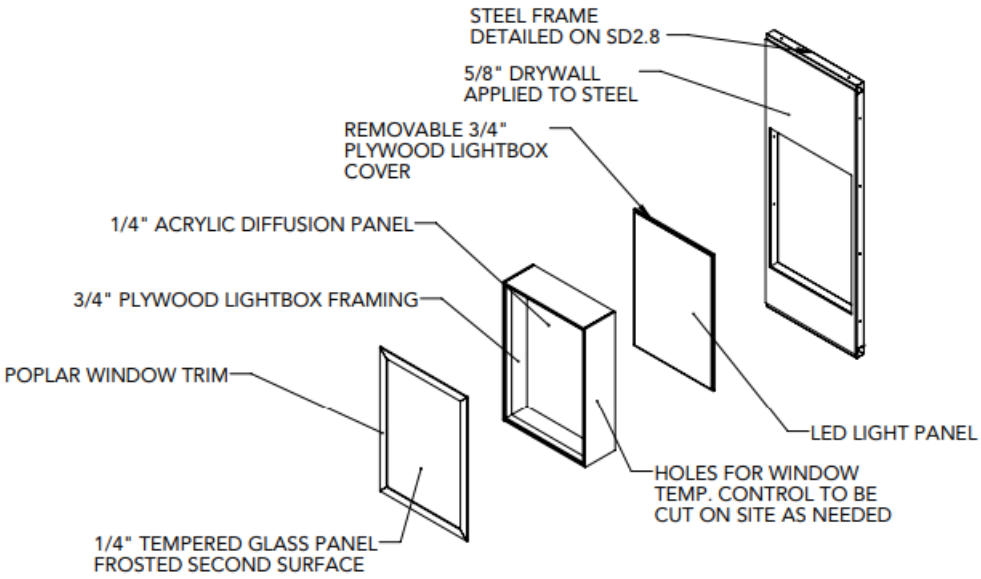

Figure 4.6 HBIL - window lighting and conditioning box

The HBIL facility was assembled at the Bridgewater Studio warehouse based on these drawings. The Purdue HBIL team then performed an on-site inspection to identify final design modifications in component details, faux color finishes on surface treatment panels, etc. Figure 4.7 shows the base panels with hydronic piping mounted in the steel frame on the right-side wall. Figure 4.8 shows the reconfigurability feature of the surface treatment. All the fourteen magnets mounted on the interior surface treatment panel can be seen. Figure 4.9 shows an image of the HBIL at Bridgewater Studio from the front side. The steel structure, front cladding, and stair were not painted at the time of the visit. The following points were identified from the site visit, which required design modifications:

- Floor panel finish was darker than anticipated while selecting a base color. Hence it was decided to change the floor color finish
- Add vinyl tape stickers to hide the magnet mounting screws that were visible on the interior surface treatment panels
- Add backing plates for all magnets to ensure good contact with the steel frame
- Change electrical switch locations from sides to the center panel at the entrance
- Color for steel structure, stairs, and cladding was finalized to match the PBE color shade
- White paint for window box to match the door color

Figure 4.7 HBIL base panels exterior view at Bridgewater Studio

Figure 4.8 HBIL interior surface treatment panel removed at Bridgewater Studio

Figure 4.9 HBIL front side at Bridgewater Studio

After accommodating all the suggested changes, the facility was installed at the PBE in Herrick Labs in November 2021. The Bridgewater Studio team set up the entire facility within four days (approximately 30 hours). The front cladding will be installed after the piping is installed. Following are some images showing the installation stages.

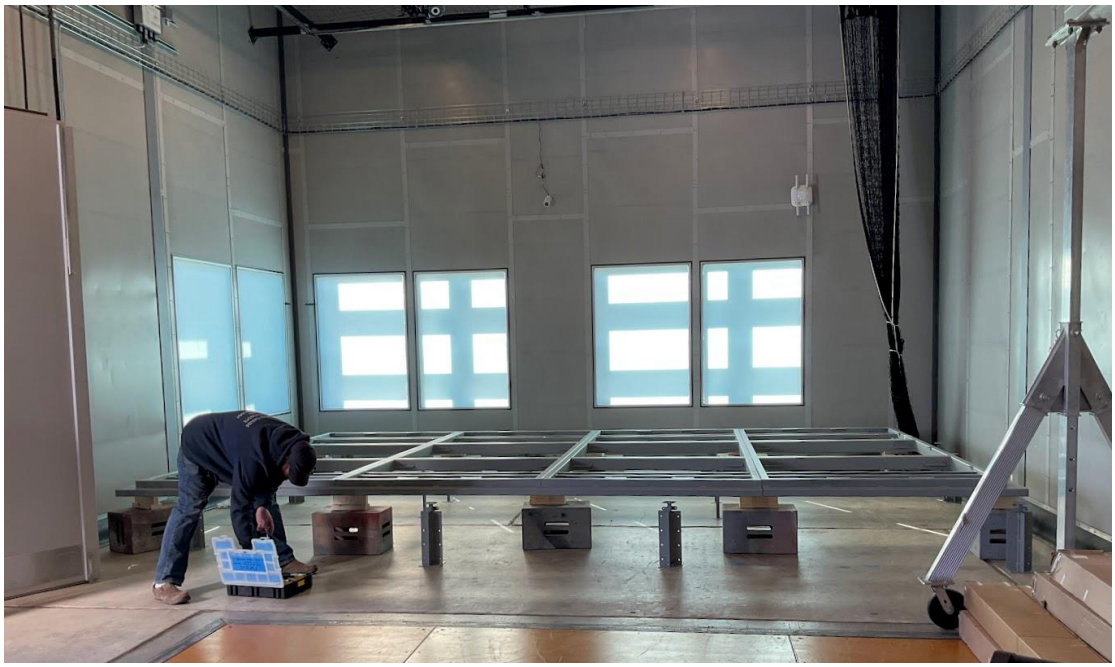

Figure 4.10 HBIL installation day 1 - base structure laid out

Figure 4.11 HBIL installation day 2 - full frame assembled

Figure 4.12 HBIL installation day 3 - base panels installed

Figure 4.13 HBIL installation day 4 - assembly completed by Bridgewater Studio team

4.2 Hydronic System Design

This section provides a detailed description of the design of the heating and cooling hydronic system for the HBIL facility. First, the heating and cooling loads were calculated to select primary heating and cooling equipment. The HBIL involves 48 panels (two 4'x5' panels paired in series to make one 4'x10' panel) that require hot or cold water. The hydronic system involves the use of a four-pipe reverse return piping layout. Pressure drop in the panel farthest from the tank location was estimated to select pumps for the hydronic system.

4.2.1 Load Estimation and Selection of Heat Pump, Water Heaters and FCU

To determine a system configuration and size equipment for controlling the surface temperatures over the range of interest, the first step was to determine facility heating and cooling loads based on heat loss/gain estimates from interior surfaces for the most extreme temperature conditions. Thus, convective and radiative heat gains/losses were estimated for the room dimensions (surface area (A) of walls, floor, and ceiling), target interior surface temperatures ($T_{surface}$), and indoor air temperature (T_{air}) conditions that are shown in Table 4.1

Table 4.1 Load estimation design parameters

Room Dimension: 20×12×10 ft	**Heating Design Temperatures**	**Cooling Design Temperatures**
A_{wall} = 640 ft^2 (59.2 m^2)	$T_{surface}$ = 80°F (26.7°C)	$T_{surface}$ = 60°F (15.5°C)
A_{floor} = Aroof = 240 ft^2 (22.3 m^2)	T_{air} = 70°F (21.1°C)	T_{air}= 74°F (23.3°C)

The convective heat transfer from the interior surfaces (walls and floor) was estimated using convective heat transfer correlations from Goldstein & Novoselac, (2010) based on air flow from ceiling diffusers. The radiative heat transfer from the interior surfaces (walls and floor) was estimated using a radiative heat transfer correlation from Bergman et al., (2011). The long-wave radiation is linearized with a view factor of unity. Table 4.2 shows the load estimation results based on heat transfer from interior surfaces (walls and floor) for the heating and cooling cases. The heating case represents the minimum heating input required to maintain a positive heat gain to the room from the interior surfaces at the specified conditions. The negative sign in the cooling case conveys that the heat transfer is into the surface from the indoor air.

Table 4.2 Load estimation for heating and cooling case

Operation Mode	Convection [W]	Radiation (*1) [W]	Total [W]	Heat Flux [W/m^2]
Heating	1592	2592	**4184**	**51**
Cooling	-2229	-3469	**-5698**	**-70**

*1 Radiation heat transfer assuming worst-case scenario for each surface, i.e., the surface in the calculation is at $T_{surface}$ whereas other walls, floor, and roof are at T_{air}, and assuming paint (ϵ=0.96)

Figure 4.14 shows a schematic of the overall hydronic system. A water-to-water heat pump providing heat transfer between chilled and hot water tanks will be coupled to the chilled and hot water loops. In addition, there will be a resistance heating element in the hot water tank and an auxiliary hot water fan coil unit (FCU) for heat rejection that will be used when necessary for load balancing. WaterFurnace donated the heat pump unit and two tanks with resistive elements. Two 120 Gallon tanks were selected with a 4.5 kW heating element in the hot water tank. The largest available heat pump model in the series was selected based on the operation point in Table 4.3 for heating mode at 19 GPM source and load side water flow rate.

Table 4.3 Heat pump operation point during the selection

Operating Mode	Cooling Capacity	Entering Source Temperature	Leaving Source Temperature	Entering Load Temperature	Leaving Load Temperature
Heating	17.26 kW	10℃	6.44℃	37.78℃	42.61℃
	4.90 Ton	50 °F	43.6 °F	100 °F	108.7 °F

A separate skid was designed to house all the hydronic system equipment that make the primary loop. In addition to the heat pump, water tanks, and FCU, there are two primary loop source, and load side fixed speed pumps, two secondary loop VFD pumps, and cold and hot side expansion tanks. The pumps were sized and selected based on the pressure drop calculations in Section 4.2.2. 1.5-inch PEX piping is used for plumbing in the primary loop, whereas 2-inch PVC piping is used for the main supply and return lines in the secondary loop.

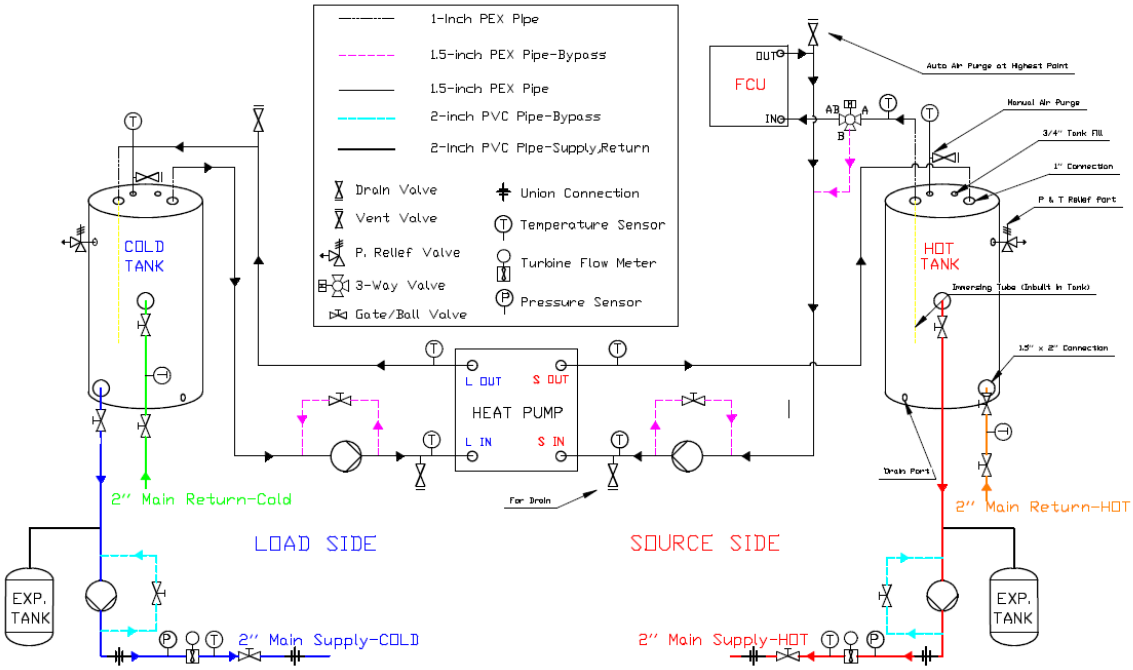

Figure 4.14 HBIL - primary loop hydronic system schematic

All four pumps have a manual bypass valve to control the water flow rate. There are expansions tanks in the hot and cold water primary loop. The FCU will be used to reject the heat when hot water is not being used in the same proportion as cold water. However, there is a 3-way valve installed to bypass the FCU when it is not in use to reduce pressure and heat loss. Both hot and cold water tanks have a pressure and temperature relief valve set at 150 psi. An automatic air purge valve will be installed at the highest location. In addition, there are manual air purge valves on both tanks. The secondary loop pumps have a VFD which will be controlled based on the head pressure sensor on the pump outlet. There is a turbine-type flow meter to measure the water flow rate. Finally, a provision will be made using a gate valve and union connections to separate the skid from the secondary piping, if required.

4.2.2 Facility Plumbing with Pressure Drop Calculations to Select Pumps

Facility is plumbing is split into four sub-loops, each having twelve panels as depicted in Figure 4.15. To decrease the number of 3-way valves and the complexity of control involved, two 4’x5’ panels are paired in series to make one panel. Hence the effective number of panels was reduced by half to 24 controllable panels. Sub-loop 1 includes the six left side and front wall panels,

sub-loop 2 includes six right side and rear wall panels, sub-loop 3 provides water to six ceiling panels, and sub-loop is six floor panels.

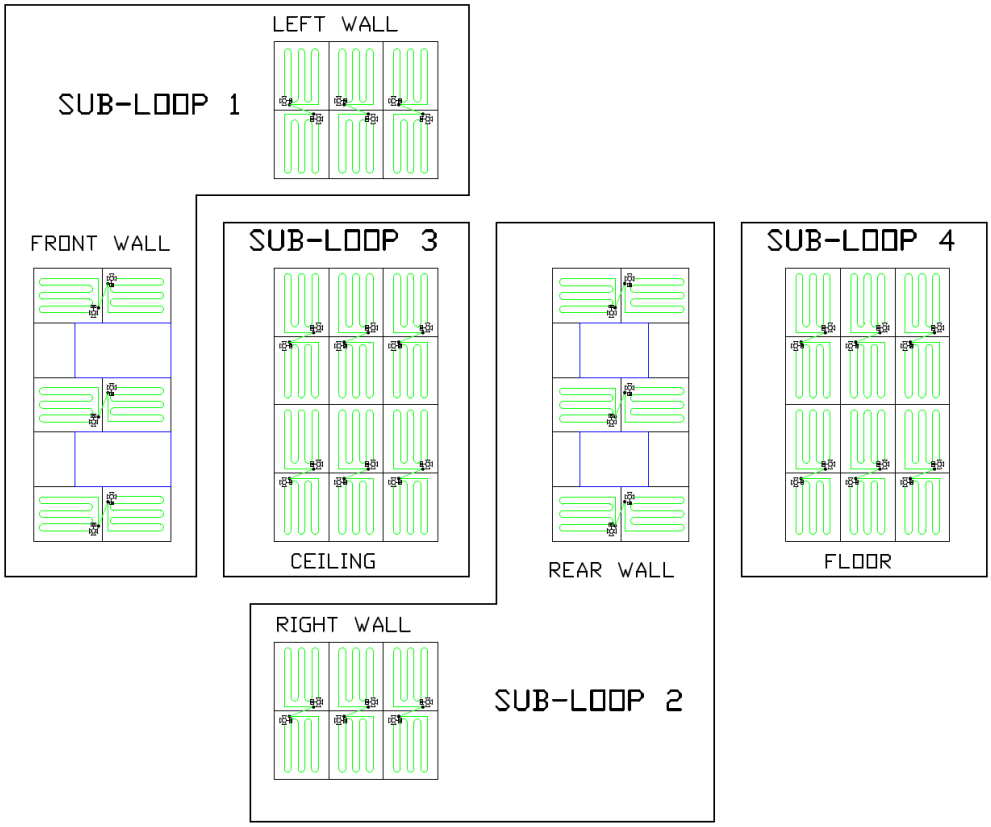

Figure 4.15 HBIL plumbing layout - 4 sub-loops

Figure 4.16 shows a schematic of the secondary loop of the hydronic system. The two 2-inch PVC main lines carry hot and cold water from respective tanks. Each pipe splits into four sub-loops through cold and hot water supply manifolds. On the return side, the sub loops meet to form two 2-inch main cold and hot water return lines that go back to the respective tanks. The sub-loops have 1-inch PEX piping. Each subloop has a manual ball valve to have the flexibility to isolate each sub-loop.

Furthermore, all the sixteen outlets of manifolds will have inline immersed thermocouple sensors to monitor the water supply and return temperatures. Provision will be made to install temporary gauge pressure sensors that will be used during the commissioning of the sub-loops. The piping manifold locations are the highest points in the whole plumbing system. Hence, four automatic air vents will be installed at these locations.

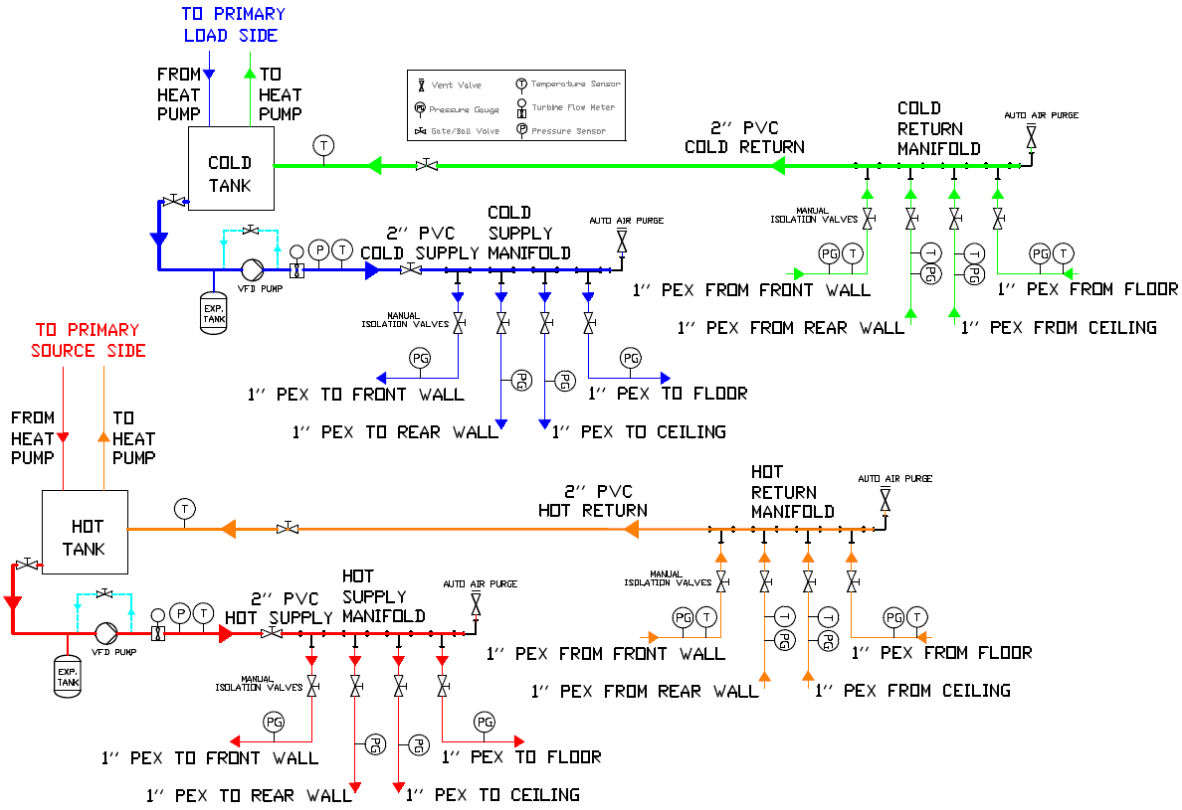

Figure 4.16 HBIL - secondary loop hydronic system schematic

The 1-inch sub-loop piping is further reduced to 1/2-inch pipe for the 3-way valve ports and the panel pipe size. A reverse return configuration is adopted for piping to achieve similar head pressures at the inlets of all the panels in each sub-loop. Based on experimental results, each panel has a pressure drop of around 1-2 psi at 1 GPM water flow rate. The two 3-way valves (mixing valve at the inlet and diverting valve at the outlet) together have pressure drop of 10 psi at 1 GPM. Hence it can be safely assumed that maintaining 10-12 psi differential pressure across the inlet and outlet of the farthest panel will ensure approximately 1 GPM water flow across each panel. A differential pressure-operated 2-way modulating bypass valve will be installed at the farthest panel in each sub-loop to maintain this pressure. It is further assumed that because of the reverse return configuration, all the panels upstream will also see enough differential pressure across the inlet and outlet ports, thereby ensuing adequate flow across them. The differential pressure bypass valve location might be changed if the assumption above does not work during the commissioning process. Figure 4.17 shows sub-loop 1 and sub-loop 2 piping with the differential pressure sensor located at the farthest panel.

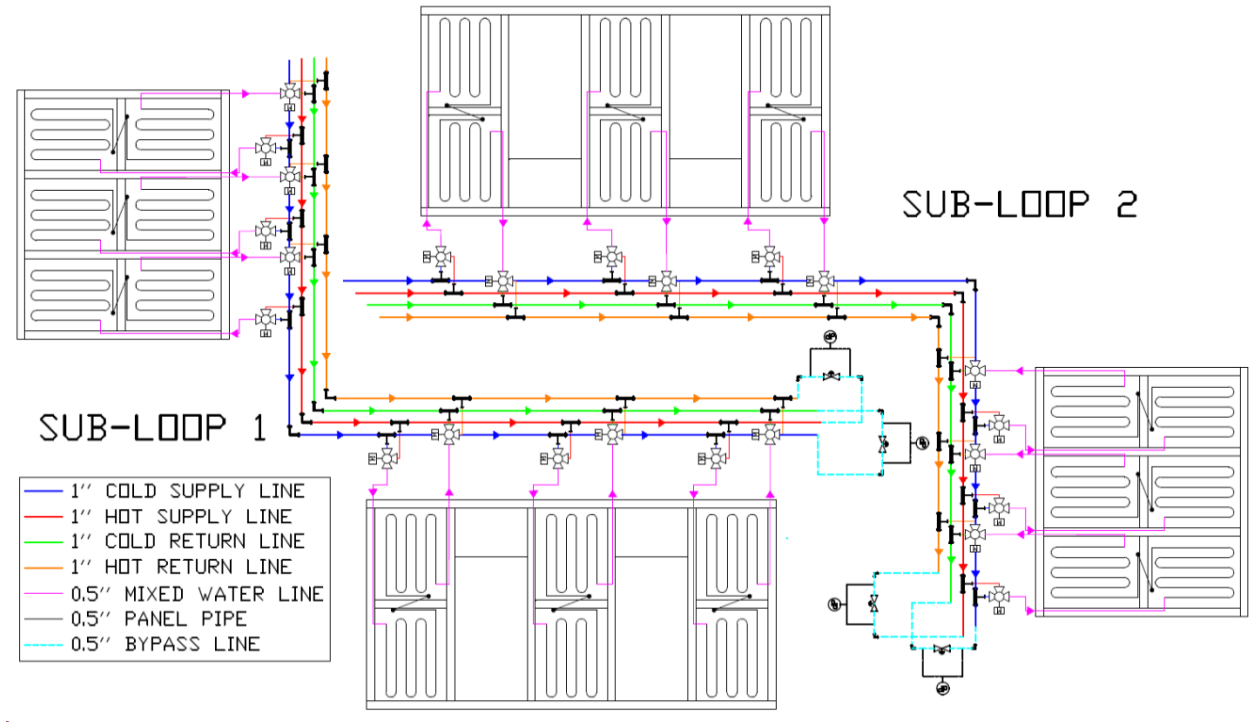

Figure 4.17 HBIL - secondary loop sub-loop 1, 2

The ceiling and floor panel sub-loops (sub-loop 3,4) will be identical due to the same layout of panels. However, the floor sub-loop will see the highest pressure drop due to increased pipe length from the top of the facility to the bottom and then back up to the return manifold. Hence, sub-loop 4 piping was used to calculate the pressure drop and select the secondary loop pumps. The cold water loop is taken for explanation purposes as both hot and cold water loops in each branch will have a similar layout and fittings, hence the same pressure drop for the identical operating conditions. Figure 4.18 shows the sub-loop 4 piping layout with the reference cold water pipe shown in larger line-thickness.

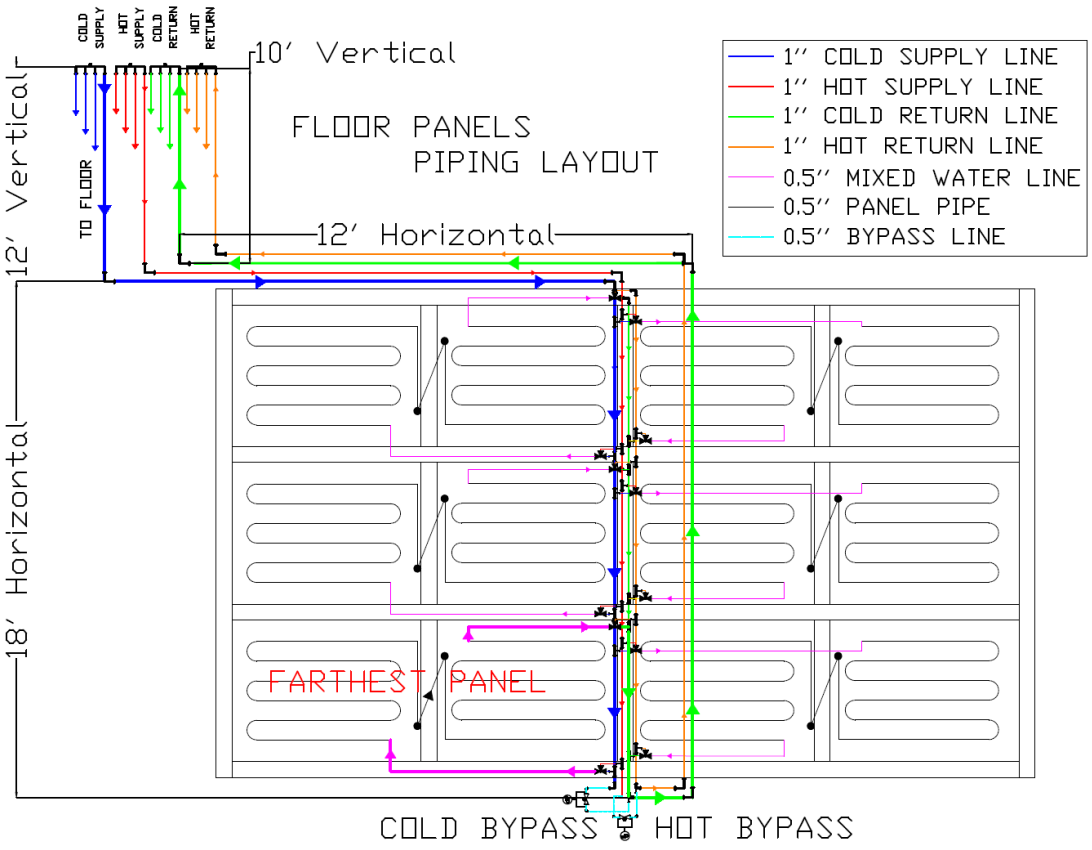

Figure 4.18 HBIL - sub-loop 4 used for pressure drop calculations

The highlighted reference pipe section is divided into different sub-sections as we move from the supply manifold to the farthest panel and ultimately back to the return manifold. These sub-sections have different lengths or water flow rates or sizes. The total piping pressure drop (PD_{piping}) is the addition of the pressure drop in these individual pipe sections and the main 2-inch PVC pipe from the secondary pump outlet to the supply manifold and back from the return manifold to the tank. Table 4.4 shows the pressure drop in these sub-sections for their respective water flow rates and pipe lengths. Values of pressure drop factors (in feet of water column) per 100 feet of tubing for 2-inch-Schedule 40 PVC pipe were taken from Engineering ToolBox, (2004). For PEX tubes of different sizes and flow rates, the values in the guide by Uponor Inc., (2020) were used. For panel piping that has copper tubes, the values from Copper Design Handbook Copper Development Association Inc, (2020) were used. These values were multiplied by respective lengths of sections to obtain the pressure-drop values. To validate these results, pressure drops in pipe sections (Shashi Menon, 2015) were also calculated using the Darcy-Weisbach equation (4.1), where the friction

factor (f) was calculated using the Colebrook-White equation (4.2). Reynolds number is calculated using Equation 4.3. Following are the key equations employed in this method. Based on the literature, an appropriate roughness factor was assumed for the pipe material (Engineering Toolbox, 2003). Table 4.4 shows the pressure drop in these sub-sections for their respective water flow rates and pipe lengths for both these methods. The Darcy-Weisbach equation assumes a standard value of absolute roughness for a specific material, whereas the manufacturer provides the pressure loss factor in the equivalent length method. Hence the resultant pressure drop is thought to be more accurate. The equivalent length method also provided more conservative estimates of the pressure drops and was employed for pump sizing.

$$h_f = f \cdot \left(\frac{L}{D}\right) \cdot \left(\frac{V^2}{2g}\right) \quad 4.1$$

$$\frac{1}{\sqrt{(f)}} = 1.14 - (2\log_{10}[(e/D) + (9.35/\mathrm{Re}\sqrt{f})]) \quad 4.2$$

$$\mathrm{Re} = \frac{V \cdot D}{\nu} \quad 4.3$$

Table 4.4 Total pressure drop in pipe sections

Piping Section	Diameter (inch)	Length (ft)	Flow Rate (GPM)	PD EQL (psi)	Darcy (psi)
PVC Main Supply Horizontal-Skid	2	5	28	0.035	0.039
PVC Main Supply Vertical-Up	2	12	28	0.083	0.094
PVC Main Supply Horizontal-Top	2	40	28	0.277	0.315
PEX Floor Supply Vertical-Down	1	12	7	0.502	0.224
PEX Floor Supply Horizontal	1	12	7	0.345	0.224
PEX Supply 1	1	3.5	5	0.078	0.036
PEX Supply 2	1	3.5	3	0.031	0.015
PEX Supply 3	0.5	3.5	1	0.004	0.002
PEX Supply 4	0.5	5	1	0.104	0.086
Copper Panel Piping	0.5	60	1	0.601	1.032
PEX Return 1	0.5	5	1	0.104	0.086
PEX Return 2	1	3.5	6	0.110	0.050
PEX Return 3	1	18	7	0.752	0.337
PEX Floor Return Horizontal	1	12	7	0.501	0.224
PEX Floor Return Vertical-Up	1	10	7	0.418	0.187
PVC Main Return Horizontal-Top	2	40	28	0.278	0.315
PVC Main Return Vertical-Down	2	10	28	0.069	0.079
PVC Main Return Horizontal-Skid	2	5	28	0.035	0.039
$PD_{PVC\ pipe} + PD_{sub-loop\ pipe} + PD_{panel\ pipe}$	=	PD_{piping}	=	**4.327**	**3.384**

The pressure drops occurring through the fittings were calculated by the equivalent length method using Equation 4.4. Equivalent length values for the fittings were provided by the fitting manufacturers (Uponor Inc., 2020), (Engineering ToolBox, 2004). Table 4.5 shows the total pressure drop across all the fittings ($PD_{fittings}$) that lie in this hydronic loop.

$$PD_{fitting\ eq} = N \cdot EQL \cdot P_{loss\ factor} \qquad 4.4$$

Table 4.5 Total pressure drop in pipe fittings

Fittings	Quantity	Diameter (inch)	Flow Rate (GPM)	PD EQL (psi)
Tee Through 2"	2	2	28	0.476
Reducing Adapter 2" x 1"	2	2	28	0.886
Flow Meter	1	1	28	1.329
Gate Valve 2"	1	2	28	0.083
Union 2"	1	2	28	0.110
Elbows 2"	3	2	28	0.947
Tee Through 2"	2	2	21	0.267
Tee Through 2"	2	2	14	0.119
Tee Through 2"	2	2	7	0.029
Tee Branch 2" x 1"	1	1	7	0.664
Adapter PVC to PEX	1	1	7	0.066
PEX adapter 1"	1	1	7	0.066
Isolation Valves	1	1	7	0.238
Elbow 1"	2	1	7	1.274
Reducing Tee 1x1x0.5"	1	1	7	0.066
Reducing Tee 1x1x0.5"	1	1	6	0.048
Reducing Tee 1x1x0.5"	1	1	5	0.034
Reducing Tee 1x1x0.5"	1	1	4	0.021
Reducing Tee 1x1x0.5"	1	1	3	0.012
Reducing Tee 1x0.5x1"-Branch	1	0.5	1	0.229
Reducing Tee 1x0.5x1"-Branch	1	0.5	1	0.229
Reducing Tee 1x1x0.5"	1	1	6	0.048
Reducing Tee 1x1x0.5"-Branch	1	1	7	0.360
3-Way Valves (Mix., Div.)	2	0.5	1	9.477
Elbow 0.5"	10	0.5	1	1.881
Reducing Tee 1x0.5x1"-Branch	1	1	7	0.360
Elbow 1"	2	1	7	1.274
Isolation Valve	1	1	7	0.066
PEX Adapter	1	1	7	0.066
Adapter PVC to PEX	1	1	7	0.066

Table 4.5 continued

Tee Branch 1" x 2"	1	1	7	0.664
Elbows 2"	3	2	28	0.947
Union 2"	1	2	28	0.110
Gate Valve 2'	1	2	28	0.083
Reducing Adapter 2" x 1.5"	2	2	28	0.498
Tee Through 2"	2	2	28	0.476
Tee Through 2"	2	2	28	0.476
	$\boldsymbol{PD_{fittings}}$			**24.045**

The estimated pressure drop through fittings was 24 psi based on the equivalent length method. The summation of total pressure drops through piping and fittings is the total maximum pressure drop (PD_{Total}) amongst all other hydronic loops. A safety factor of 15% was assumed, leading to a design pressure-drop of 32.6 psi for the hydronic system. The hot and cold-water pumps in the secondary loop were selected based on this value. The smaller pumps were selected based on the flow rate requirements of the heat pump load and source side. Table 4.6 summarizes the total pressure-drop calculation results. The EES pressure drop calculation tables are included in the Appendix section. Table 4.7 shows the main equipment selected for the HBIL facility.

Table 4.6 Pressure drop calculation summary

Pressure Drop		**psi**
Pressure drop through all pipe sections	$\boldsymbol{PD_{piping}}$	4.327
Pressure drop through all fittings	$\boldsymbol{PD_{fittings}}$	24.045
Total Pressure Drop	$\boldsymbol{PD_{Total}}$	28.372
$\boldsymbol{PD_{Facility} = PD_{Total} \cdot 1.15 =}$		**32.628**

Table 4.7 HBIL-Hydronic equipment list

Sr. No.	**Equipment**	**Brand**	**Specifications**
1	Hot water tank with a heating element	WaterFurnace	GEO Storage-120 Gallon 4.5 kW Heating Element
2	Heat Pump (Water Chiller)	WaterFurnace	Series-5-Water to Water 17.2 kW 208-230V, Single Phase
3	Fan Coil Unit (FCU)	Johnson Controls	Horizontal Direct Drive-VFD JCI-AHD-40, 23.2 kW

Table 4.7 continued

4	Primary Loop Pumps (Single Speed)	Grundfos	CR 5-2-1ph -20 GPM, 15 psi Single Phase, 0.75 HP
5	Secondary Loop Pumps (VFD)	Grundfos	CR 5-4 -30 GPM, 33 psi Single Phase, 1.5 HP

4.3 Installation and Commissioning of Hydronic System

4.3.1 Installation and Commissioning Plan

The Bridgewater Studio team installed the HBIL facility at Herrick Labs in the first week of November. Following this, the installation of the hydronic system, electrical system, and controls system is underway. Table 4.8 shows the installation plan, and Table 4.9 presents the commissioning plan.

Table 4.8 HBIL - Installation plan

Sr. No.	Tasks	12/21	01/22	02/22	03/22	04/22
1	**Facility Side Installation**					
1.1	Bridgewater-vinyl tape, miscellaneous touch-up					
1.2	Fall protection safety railings installation					
1.3	Plumbing wireways installation					
1.4	Ceiling and Floor tray installation					
2	**Hydronic System**					
2.1	Unistrut mounts for heat pump and water pumps					
2.2	Primary loop plumbing					
2.4	FCU ductwork					
2.5	PVC plumbing					
2.6	Secondary loop plumbing-walls					
2.7	Secondary loop plumbing-ceiling					
2.8	Secondary loop plumbing-floor					
3	Electrical System					
3.1	Main power wiring					
3.2	Control wiring					
4	**Controls and Instrumentation System**					
4.1	Testing Panel surface temperature sensors					
4.2	Water leak sensors installation and testing					
4.3	Primary loop controls, instrumentation installation					

Table 4.8 continued

4.4	**3-way valve installation**					
4.5	Thermocouple wiring and installation					
4.6	Pressure sensors and bypass valves wiring					
4.7	LabView VI development and DAQ installation					

Task Completed Task Scheduled

Table 4.9 HBIL - Commissioning plan

Sr. No.	Tasks	02/22	03/22	04/22	05/22	06/22
1	**Primary Loop Commissioning**					
1.1	Heat Pump and HydroStat					
1.2	Heat Pump with FCU with LabView					
1.3	VFD Pumps with Bypass					
2	**Secondary Loop Commissioning**					
2.1	Sub-loop 1					
2.2	Sub-loop 2					
2.4	Sub-loop 3					
2.5	Sub-loop 4					
2.6	All sub-loops manual-Heating and Cooling					
3	**Overall Facility Commissioning**					
3.1	PI control development and commissioning					
3.2	Full Facility simultaneous Heating and Cooling					

Task Completed Task Scheduled

4.3.2 Installation and Commissioning of Primary Loop

The Primary loop of the hydronic system, as depicted in Figure 4.14 includes the heat pump, primary loop pumps, cold and hot water tanks, fan coil unit for excess heat rejection along with a series of sensors and control devices. All the plumbing in primary loop is completed in 1.5-inch PEX tubing. The secondary loop plumbing from tanks to the manifolds is done in 2-inch PVC piping to accommodate larger maximum water flow rate of 30 GPM. The skid also houses the secondary loop VFD pumps and expansion tanks. The plumbing has been done in such a way that the skid can be easily disengaged from the secondary loop piping using isolating valves and union connections. All the pumps have bypass loops for manual flow regulation. Figure 4.19 shows the completed installation of the equipment skid. The heat pump commissioning was completed by running it in

cooling mode using a manufacturer provided thermostat controller. Following this, heat pump commissioning using LabView VI is scheduled.

Figure 4.19 HBIL-primary loop equipment skid

5. CONCLUSIONS AND FUTURE WORK

This thesis describes the overall design approach of a novel Human-Building Interactions Laboratory (HBIL). This included the development of prototype thermo-active wall panels and their experimental characterizations that guided the design decisions of the complete HBIL facility. Moreover, a 1-D transient numerical model of the prototype wall panel was developed, tuned, and validated to predict the thermal performance of the thermo-active panels and assess various design choices. Furthermore, the design and installation steps for the hydronic system of the HBIL facility were also presented with an initial commissioning plan.

Based on experimental investigation, copper tubes showed better performance in terms of extreme panel surface temperatures and dynamic response. The panel was able to satisfy the target temperature bounds of 15.5℃ (60°F) and 26.66℃ (80°F) and was able to cool or heat the panel surface from room temperature to extreme heating and cooling temperatures within the desired 50 minutes. The series layout showed the best uniformity in surface temperature distribution. Further investigation also showed that C-type heat spreaders performed better than the U-type. Adding thermal paste between the copper tubes and heat spreaders improved the heat transfer rate. The 3-way valve showed acceptable mixing characteristics from 30% to 70% opening, providing mixed water temperatures from 5℃ to 40℃.

A range of thermocouple sensor options were tested on the prototype wall panel for panel surface temperature measurement. The welded-tip thermocouple sensor was finalized as it was the least expensive amongst other equally performing sensors. The surface treatment attachment method was tested on the new prototype panel testbed provided by Bridgewater Studios. Internally threaded magnets were selected, and the total magnets were increased from eight to fourteen to ensure better contact and stronger pull strength. Drywall, Plywood, Hardwood, and MDF material surface treatments were also tested on the new prototype panel test stand. Out of these, MDF with faux color finishes proved to be the best in terms of required thermal properties and mechanical strength and rigidity.

The 1-D transient numerical model was developed in EES, tuned, and validated using the experimental data. The model helped in understanding important thermophysical characteristics of the panel, for example, convective and radiative heat transfer coefficients at different temperatures, heat transfer rates, contact resistances, thermal capacitances, etc. This model will help develop the

overall facility model in Modelica and select different surface treatment materials in the future. Based on the experimental findings and modeling results, the thermo-active panel design was finalized.

A series of drawings were reviewed based on the changes suggested at various experimental stages. The final design of HBIL satisfies important target goals like reconfigurable interior panels, modular structure and design, provision for air diffuser slots for ventilation, and so on. However, the panel size in the final design is effectively 4’ x 10’ instead of the original 4’ x 5’ design because 2 panels are paired together to decrease the number of 3-way valves and ease the controllability.

The HBIL hydronic system was also designed to provide hot and cold water for all the panels. A water-to-water heat pump is used in cooling mode for cold water, and a tank with an electric heating element is used for hot water. A 4-pipe return configuration with a differential pressure operated 2-way bypass valve is used at the end of each subloop. The detailed piping layouts are designed, and the installation is in progress. An installation and commissioning plan is laid out that involves step-by-step installation and loop-by-loop commissioning.

The challenges would involve commissioning the complex hydronic loops with pressure and flow balancing, running out of thermal capacity when running all the panels close to 50% mixing point, and designing the optimum control strategy for individual panels.

Future work will include testing the hydronic system to demonstrate that it can provide localized heating and cooling using LabVIEW controls, followed by integrating smart voice assistants with the control systems. Different residential and commercial spaces will be emulated using the facility to test occupant perception of thermal comfort and the effect of their interaction with the building control systems.

Furthermore, this facility will serve as a testbed to evaluate decentralized local heating and cooling systems like micro heat pumps embedded in the wall panels. Due to reconfigurability, the HBIL will also enable testing of advanced phase change materials along with the integration of intelligent sensors.

APPENDIX A. 1-D STEADY-STATE MODEL CODE

Heat transfer Model for Wall Panel- Steady State Analysis

Sourabh Yadav

- Layers

,,,,,,,,,,,,,,,, *- Gypsum Panel (gp)*

,,,,,,,,,,,,,,,, *- Support Panel (sp)*

,,,,,,,,,,,,,,,, *- Aluminum Panel (al)*

,,,,,,,,,,,,,,,, *- Heat Spreader (pn)*

,,,,,,,,,,,,,,,, *- Copper tube (tb)*

,,,,,,,,,,,,,,,, *- Insulation (ins)*

SUBPROGRAM **steadystate** (C_b, h_{edge}, $R_{al,sp}$, $R_{sp,gp}$, $R_{pn,ins}$, $T_{w,Int}$, $\dot{v}_{w,Int}$, $T_{Room,Air}$: $Temp_{al,C}$, $T_{Surface,C}$)

$Fluid_{os}$ = 'WATER'

$V_{I,air}$ = 0.25 [m/s] *Indoor Air Velocity from comfort conditions*

IDT_{SP} = 70 [F] *Indoor Air Temperature - Assumed Constant*

RH_{space} = 0.6 *Indoor Relative Humidity*

T_{supply} = 55 [F] *Supply Air Temperature from AHU*

ACH = 10 *Air Change per hour*

$P_{atm} = 1 \cdot \left| 101.325 \cdot \frac{kPa}{atm} \right|$ *Air Pressure Inside as well in Outside Air*

T_{amb} = 25 [C] *Ambient Temperature*

$T_{w,In}$ = **ConvertTemp** (C , K , $T_{w,Int}$)

$\rho_w = \rho(Fluid_{os}, T = T_{amb}, P = P_{atm})$

$Cp_w = Cp(Fluid_{os}, T = T_{amb}, P = P_{atm}) \cdot \left| 1000 \cdot \frac{J/kg-K}{kJ/kg-K} \right|$

During Initial Steady State

$\dot{V}_w = \dot{v}_{w,Int} \cdot \left| 0.0000630902 \cdot \frac{m3/s}{gpm} \right|$

$\dot{m}_{w,Int} = \dot{V}_w \cdot \rho_w$ *Volume Flow rate in single PEX/Copper tube*

Convert T in Kelvin

T_{ID} = **ConvertTemp** (C , K , $T_{Room,Air}$)

T_{sink} = **ConvertTemp** (F , K , T_{supply})

T_{env} = **ConvertTemp** (C , K , T_{amb})

$T_{OD} = T_{ID}$

Outside Temperature

$Fluid_{i\$} = 'AIR_{HA}'$

$\rho_{air} = \rho(Fluid_{i\$}, T = T_{amb}, P = P_{atm})$

$Cp_{air} = Cp(Fluid_{i\$}, T = T_{amb}, P = P_{atm})$

Properties of Layers

Gypsum Panel

$H_{gp} = 5 \cdot \left| 0.3048 \cdot \frac{m}{ft} \right|$ *Height*

$W_{gp} = 4 \cdot \left| 0.3048 \cdot \frac{m}{ft} \right|$ *Width*

$t_{gp} = 1/4 \cdot 1 \cdot \left| 0.0254 \cdot \frac{m}{inch} \right|$ *Thckness*

Based on ASHRAE Fundamentals - 2017

$C_{gp} = 950$ [J/kg-K] *Specific Heat*

$\rho_{gp} = 668$ [kg/m3] *Density*

$k_{gp} = 0.17$ [W/m-K] *Thermal Conductivity ENgineering ToolBox*

$\varepsilon_{gp} = 0.903$ *Emissivity on a smooth plate*

$RelRough_{gp} = 0.02$ **Assumption**

Support Panel

$H_{sp} = H_{gp}$

$W_{sp} = W_{gp}$ *Heght and width same as gypsum panel*

$t_{sp} = 0.13 \cdot 1 \cdot \left| 0.0254 \cdot \frac{m}{inch} \right|$ *Thickness*

$material_{sp\$} = 'Aluminum_{6061}'$

$\rho_{sp} = \rho(material_{sp\$}, T = T_{amb})$

$C_{sp} = Cp(material_{sp\$}, T = T_{amb}) \cdot \left| 1000 \cdot \frac{J/kg-K}{kJ/kg-K} \right|$

$k_{sp} = k(material_{sp\$}, T = T_{amb})$

$AbsRough_{sp} = 0.002 \cdot 10^{-3} \cdot 1$ [m]

Aluminium Panel

$H_{al} = 48 \cdot \left| 0.0254 \cdot \frac{m}{inch} \right|$

$W_{al} = 54 \cdot \left| 0.0254 \cdot \frac{m}{inch} \right|$ *Heght and width same as gypsum panel*

$t_{al} = 0.13 \cdot 1 \cdot \left| 0.0254 \cdot \frac{m}{inch} \right|$ *Thickness*

$Alumin\$ = 'Aluminum_{6061}'$

$\rho_{al} = \rho(Alumin\$, T = T_{amb})$

$C_{al} = Cp(Alumin\$, T = T_{amb}) \cdot \left| 1000 \cdot \frac{J/kg-K}{kJ/kg-K} \right|$

$k_{al} = k(Alumin\$, T = T_{amb})$

$AbsRough_{al} = 0.002 \cdot 10^{-3} \cdot 1$ [m] *Absolute Roughness: https://www.engineeringtoolbox.com/surface-roughness ventilation-ducts-d_209.html*

Heat Trasnfer Panel / Spreader

$t_{pn} = 0.05 \cdot \left| 0.0254 \cdot \frac{m}{in} \right|$ *Thickness*

$W_{pn} = 4 \cdot \left| 0.0254 \cdot \frac{m}{in} \right|$ *Width*

$H_{pn} = 48 \cdot \left| 0.0254 \cdot \frac{m}{in} \right|$ *Length*

$material_{pn\$} = 'Aluminum'$ *Material*

$k_{pn} = k(material_{pn\$}, T = T_{amb})$

$\rho_{pn} = \rho(material_{pn\$}, T = T_{amb})$

$C_{pn} = Cp(material_{pn\$}, T = T_{amb}) \cdot \left| 1000 \cdot \frac{J/kg-K}{kJ/kg-K} \right|$

$A_{pn} = 4 \cdot 48 \cdot \left| 0.00064516 \cdot \frac{m^2}{in^2} \right|$ *Surface area of heat spreader*

COPPER Tube

Size: 3/8"

Tube Material Thermal Conductivity

$ID_{tb} = 0.35 \cdot \left| 0.0254 \cdot \frac{m}{in} \right|$ *Tube Internal Diameter*

$OD_{tb} = 0.5 \cdot \left| 0.0254 \cdot \frac{m}{in} \right|$ *Tube Outer Diamater*

$L_{tb} = 48 \cdot \left| 0.0254 \cdot \frac{m}{in} \right|$ *Length of tube in each pass*

$AbsRough_{tb} = 0.0015 \cdot \left| 0.001 \cdot \frac{m}{mm} \right|$

$RelRough_{tb} = \frac{AbsRough_{tb}}{ID_{tb}}$

$W = 8 \cdot \left| 0.0254 \cdot \frac{m}{in} \right|$ *Spacing between two tube passes*

Panel Frame

$Edge_{Width} = 4 \cdot \left| 0.0254 \cdot \frac{m}{inch} \right|$

$Edge_{Height} = 59 \cdot \left| 0.0254 \cdot \frac{m}{inch} \right|$

$Edge_{Base} = 48 \cdot \left| 0.0254 \cdot \frac{m}{inch} \right|$

$Edge_{SArea,V} = 2 \cdot Edge_{Width} \cdot Edge_{Height}$

$Edge_{SArea,H} = 2 \cdot Edge_{Width} \cdot Edge_{Base}$

$Edge_{SArea} = Edge_{SArea,V} + Edge_{SArea,H}$

Insulation

Poured foam in place

$\rho_{ins} = 30$ [kg/m3] *Density of Insulation material*

$k_{ins} = 0.0245$ [W/m-K] *Thermal conductivity of insulation material*

$t_{ins} = 2.5 \cdot \left| 0.0254 \cdot \frac{m}{in} \right|$ *Thickess of Insulation*

$C_{ins} = 1000$ [J/kg-K]

$A = H_{gp} \cdot W_{gp}$ *Surface area of each layer*

*Thermal resistances in each layer=Thickness of layer/(thermal conductivity*Surface area) K/W*

$R_{gp} = \frac{t_{gp}}{k_{gp} \cdot A}$ *Thermal resistance in gypsum panel*

$R_{sp} = \frac{t_{sp}}{k_{sp} \cdot A}$ *Thermal resistance in support panel*

$R_{al} = \frac{t_{al}}{k_{al} \cdot A}$ *Thermal resistance in aluminum panel*

$R_{pn} = \frac{t_{pn}}{k_{pn} \cdot A}$ *Thermal resistance in heat spreader*

Thermal resistance in water-tube wall

$R_{ins} = \frac{t_{ins}}{k_{ins} \cdot A}$ *Thermal resistance in insulation*

Insulation Surface to outdoor resistance

Call $fc_{plate,vertical}$ ($Fluid_{is}$, $T_{Surface,C}$, 22 [C], 101.3 [kPa], 1.542 [m] : h_{ins})

$$R_{air,ins} = \frac{1}{h_{ins}}$$

Resistances

$$R_{contact} = \frac{R_{al,sp} + R_{sp,gp}}{A}$$ *Total Contact Resisitance*

$$R_{f,total} = R_{al} + R_{sp} + R_{gp}$$ *Total Thermal Resistance-Front-AL to GP*

$$R_{b,total} = \frac{R_{pn,ins}}{A_{pn} \cdot 6} + R_{ins} + \frac{R_{air,ins}}{A}$$ *Total Thermal Resistance-Back-PN to INS*

Overall loss coefficients

$$U_F = \frac{1}{R_{f,total} + R_{contact}}$$ *Front Overall loss coefficient*

$$U_B = \frac{1}{R_{b,total}}$$ *Back Overall loss coefficient*

Fin Efficiency Factor

$$m = \sqrt{\frac{U_F}{k_{al} \cdot t_{al}}}$$

$$F = \tanh\left[\frac{m \cdot \left[\frac{W - OD_{tb}}{2}\right]}{m \cdot \left[\frac{W - OD_{tb}}{2}\right]}\right]$$ *Fin efficiency factor*

Heat Balance

$n_t = 6$ *No. of Tubes*

$Eq_L = L_{tb} \cdot n_t$ *Tube Equivalent length*

Call $\mathbf{pipeflow_{local}}(Fluid_{os}, T_{amb}, P_{atm}, \dot{m}_{w,Int}, ID_{tb}, Eq_L, RelRough_{tb} : h_{fi})$ *To calculate water-tube wall convective HTC*

Call $\mathbf{fc_{plate,vertical}}(Fluid_{is}, T_{Surface,C}, T_{Room,Air}, 101.3\ [kPa], 1.542\ [m] : h_c)$

$h_r = \varepsilon_{gp} \cdot 5.670E{-}08\ [W/m^2\text{-}K^4] \cdot (T_{surface}^2 + T_{ID}^2) \cdot (T_{surface} + T_{ID})$ *Radiative heat transfer coefficient Gypsum-Indoor Air*

$h_i = h_c + h_r$ *Net HTC (Convective+Radiative) between Panel Surface-Indoor Air*

$$R_{air} = \frac{1}{h_i \cdot A}$$ *Thermal resistance-Gypsum-Indoor Air*

$$\dot{Q}_{loss} = F \cdot U_B \cdot (Temp_{pn} - T_{OD})$$ *Heat Lost to Outoor*

$$\dot{Q}_{in} = Eq_L \cdot \left[\frac{T_{w,in} - Temp_{pn}}{\frac{1}{C_b} + \frac{1}{h_{fi} \cdot \pi \cdot ID_{tb}}}\right]$$ *Heat In from water to heat spreader*

$$\dot{Q}_{front} = \frac{Temp_{pn} - Temp_{al}}{\frac{R_{al}}{2}}$$

Heat to Surface = Heat in-Heat Loss-Heat Edge

$\dot{Q}_{edge} = h_{edge} \cdot Edge_{BArea} \cdot (Temp_{sp} - T_{ID})$ *Heat Lost to Indoor through panel frame/edges*

Heat Spreader Node Energy Balance

$\dot{Q}_{in} = \dot{Q}_{front} + \dot{Q}_{loss}$

Aluminum Node Energy Balance

$$\dot{Q}_{front} = \frac{Temp_{al} - Temp_{sp}}{\frac{R_{al}}{2} + \frac{R_{sp}}{2} + \frac{R_{al,sp}}{A}}$$

Support Panel Node Energy Balance

$$\frac{Temp_{al} - Temp_{sp}}{\frac{R_{al}}{2} + \frac{R_{sp}}{2} + \frac{R_{al,sp}}{A}} = \frac{Temp_{sp} - Temp_{gp}}{\frac{R_{sp}}{2} + \frac{R_{gp}}{2} + \frac{R_{sp,gp}}{A}} + h_{edge} \cdot Edge_{BArea} \cdot (Temp_{sp} - T_{ID})$$

Gypsum Panel Energy Balance

$$\frac{Temp_{sp} - Temp_{gp}}{\frac{R_{sp}}{2} + \frac{R_{gp}}{2} + \frac{R_{sp,gp}}{A}} = \frac{Temp_{gp} - T_{ID}}{\frac{R_{gp}}{2} + R_{air}}$$

$Temp_{gp} = T_{surface}$

$T_{Surface,C} = \mathbf{ConvertTemp}(K, C, T_{surface})$

$Temp_{al,C} = \mathbf{ConvertTemp}(K, C, Temp_{al})$

$Temp_{sp,C} = \mathbf{ConvertTemp}(K, C, Temp_{sp})$

$$\dot{Q}_{loss} = \frac{Temp_{pn} - Temp_{Ins}}{\frac{R_{Ins}}{2} + \frac{R_{pn,Ins}}{A}}$$ *To calculate Insulation Node Temperature*

$\dot{Q}_{in} = \dot{m}_{w,Int} \cdot Cp_w \cdot (T_{w,out} - T_{w,In})$ *To calculate Water Outlet Temperature*

$\Delta T = T_{w,out} - T_{w,In}$ *Water inlet-outlet temperature*

END steadystate

Input Parameters

To calculate Error

$NR = \mathbf{NLookupRows}('Steady State')$

$Error_{88,0} = 0$

$Error_{Step,0} = 0$

$T_{w,Int,i} = \mathbf{Lookup}('Steady State', i, 'T_{In}')$ (for i = 1 to NR) *Chilled Water inlet temperature / SP*

$\dot{V}_{w,Int,i} = \mathbf{Lookup}('Steady State', i, 'Mixed_{Flow}')$ (for i = 1 to NR) *Water FLow Rate*

$T_{Room,Air,i}$ = **Lookup** ('Steady State', i, 'T_{Env}') (for i = 1 to NR) *Indoor Air Temperature*

Call steadystate (C_b, h_{edge}, $R_{al,sp}$, $R_{sp,gp}$, $R_{pn,Ins}$, $T_{w,Int,i}$, $\dot{V}_{w,int,i}$, $T_{Room,Air,i}$: $Temp_{al,C,1}$, $T_{surface,C,i}$) (for i = 1 to NR)

$T_{AL,Expt,i}$ = **Lookup** ('Steady State', i, '$T_{Al,Back}$') (for i = 1 to NR)

$T_{Surface,Expt,i}$ = **Lookup** ('Steady State', i, 'T_{avg}') (for i = 1 to NR)

$DTAL_i = |T_{AL,Expt,i} - Temp_{al,C,i}|$ (for i = 1 to NR)

$DTS_i = |T_{Surface,Expt,i} - T_{surface,C,i}|$ (for i = 1 to NR)

$DT1_i = DTAL_i \cdot DTAL_i$ (for i = 1 to NR)

$DT2_i = DTS_i \cdot DTS_i$ (for i = 1 to NR)

$Error_{Step,i} = \sqrt{DT1_i + DT2_i}$ (for i = 1 to NR)

$Error_{SS,i} = Error_{Step,i} \cdot Error_{Step,i} + Error_{SS,i-1}$ (for i = 1 to NR)

$Error_{SS} = \sqrt{Error_{SS,11}}$

Lookup Table-Experimental data used for tuning steady-state parameters

	1 time [min]	2 Step [-]	3 Mixing Percentage [-]	4 T_{Env} [C]	5 $Mixed_{Flow}$ [GPM]	6 T_{in} [C]	7 T_{out} [C]	8 Mixed Head (psi)	9 $Diff_{P}$ (psi)	10 T_{avg} [C]	11 $T_{Al,Back}$ [C]
Row 1	1	1	0	21.5	0.958	4.53	5.26	13.22	3.03	14.35	10.45
Row 2	2	2	30	21.61	0.801	6.72	7.5	12.1	2.33	15.14	12.85
Row 3	3	3	35	21.72	0.832	10.32	11.17	12.61	2.34	17.02	14.54
Row 4	4	4	40	21.83	0.831	16.36	16.86	12.28	2.34	20.01	18.55
Row 5	5	5	45	21.94	0.833	19.91	20.24	12.18	2.06	21.64	21.19
Row 6	6	6	50	22.06	0.712	25.62	25.52	11.62	2.14	24.1	24.85
Row 7	7	7	55	22.17	0.764	26.86	26.72	13.09	2.12	24.05	25.43
Row 8	8	8	60	22.28	0.749	30.62	30.26	15.45	1.66	26.19	28.1
Row 9	9	9	65	22.39	1	35	34.5	16	2.62	28.8	31.5
Row 10	10	10	85	22.42	0.85	39.73	39.26	13	2.22	31.3	34.6
Row 11	11	11	100	22.5	0.991	44.55	43.69	10.96	2.6	33.31	38.2

Result Table-Model predicted result table

Main

Sort	1 $DT1_i$ [C2]	2 $DT2_i$ [C2]	3 $DTAL_i$ [C]	4 DTS_i [C]	5 $Error_{SS,i}$ [C2]	6 $T_{Room,Air,i}$ [C]	7 $\dot{V}_{w,int,i}$ [gpm]	8 $T_{w,int,i}$ [C]	9 $T_{Surface,Expt,i}$ [C]	10 $T_{surface,C,i}$ [C]	11 $T_{AL,Expt,i}$ [C]	12 $Temp_{al,C,i}$ [C]	13 $Error_{Step,i}$ [C]
[0]					0								0
[1]	0.1913	0.6982	0.4374	0.8356	0.8894	21.5	0.958	4.53	14.35	13.51	10.45	10.01	0.9431
[2]	1.731	0.3051	1.316	0.5523	2.926	21.61	0.801	6.72	15.14	14.59	12.85	11.53	1.427
[3]	0.3123	0.5209	0.5589	0.7217	3.759	21.72	0.832	10.32	17.02	16.3	14.54	13.98	0.9128
[4]	0.212	0.6981	0.4604	0.8355	4.669	21.83	0.831	16.36	20.01	19.17	18.55	18.09	0.954
[5]	0.4217	0.5012	0.6494	0.7079	5.592	21.94	0.833	19.91	21.64	20.93	21.19	20.54	0.9607
[6]	0.1257	0.09267	0.3545	0.3044	5.81	22.06	0.712	25.62	24.1	23.8	24.85	24.5	0.4673
[7]	0.003358	0.1523	0.05795	0.3902	5.966	22.17	0.764	26.86	24.05	24.44	25.43	25.37	0.3945
[8]	0.02747	0.002433	0.1657	0.04933	5.996	22.28	0.749	30.62	26.19	26.24	28.1	27.93	0.1729
[9]	0.3423	0.2538	0.585	0.5038	6.592	22.39	1	35	28.8	28.3	31.5	30.91	0.7721
[10]	0.3031	0.8022	0.5506	0.8956	7.697	22.42	0.85	39.73	31.3	30.4	34.6	34.05	1.051
[11]	0.8545	0.5542	0.9244	0.7445	9.106	22.5	0.991	44.55	33.31	32.57	38.2	37.28	1.187

Result Plot-Model predicted result vs experimental results after tuning

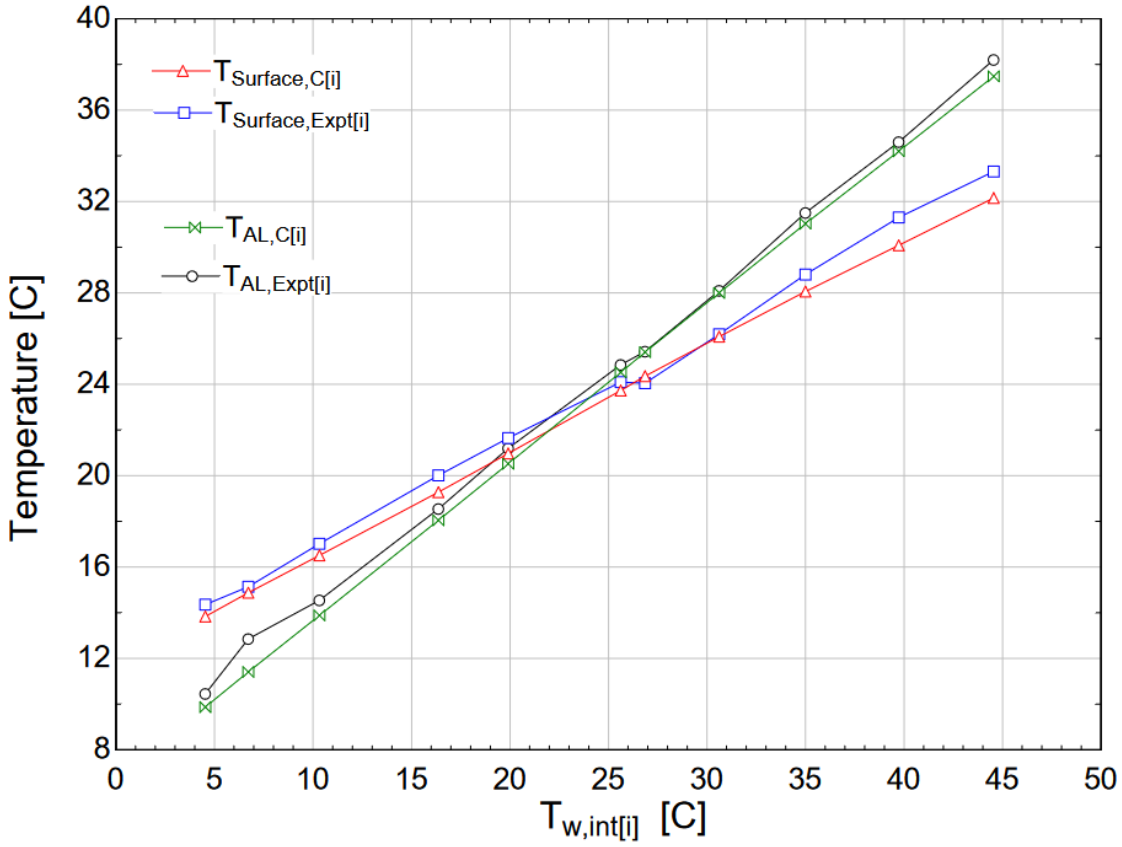

APPENDIX B. 1-D TRANSIENT MODEL CODE

Heat transfer Model for Wall Panel- Transient Analysis-Tuned

Sourabh Yadav

- Layers

,,,,,,,,,,,,,,,, *- Gypsum Panel (gp)*

,,,,,,,,,,,,,,,, *- Support Panel (sp)*

,,,,,,,,,,,,,,,, *- Aluminum Panel (al)*

,,,,,,,,,,,,,,,, *- Heat Spreader (pn)*

,,,,,,,,,,,,,,,, *- Copper tube (tb)*

,,,,,,,,,,,,,,,, *- Insulation (ins)*

Procedure to calculate error

```
Procedure optimizetr (Temp_al,C, T_Surface,C, time : Error_TR)
  N_TR := 139
  Error_T,0 := 0
  Error_TR,0 := 0
  If (time >= N_TR ) Then
     Duplicate i=1, N_TR
     T_AL,Expt, i := Lookup ('Data Sept 15', i, 'T_Al,Back' )
     T_Surface,Expt, i := Lookup ('Data Sept 15', i, 'T_avg' )
     DTAL, i := |T_AL,Expt, i - Temp_al,C |
     DTS, i := |T_Surface,Expt, i - T_Surface,C |
     DT1, i := DTAL, i · DTAL, i
     DT2, i := DTS, i · DTS, i
     Error_T, i := √(DT1, i + DT2, i)
     Error_TR, i := Error_T, i · Error_T, i + Error_TR, i-1
  End
  Error_TR := √(Error_TR,139)
Else
  Error_TR := 0
End optimizetr

EndTime = 139 [min]
```

$C_b = 4.18$ [W/m-K] *Bond Conductance-Ideal*

$h_{Edge} = 9.86$ [W/m^2-K] *Combined Radiative+Convective Heat Transfer Coefficent for edge loss*

$Fluid_{o\$} =$ 'WATER' *Fluid in tubes*

FOr Transient

$T_{w,Int} =$ **Lookup** ('Data Sept 15', time, 'T_{In}') *Chilled Water inlet temperature / SP*

$\dot{v}_{w,Int} =$ **Lookup** ('Data Sept 15', time, '$MIXED_{FLOW}$')

$T_{Room,Air} =$ **Lookup** ('Data Sept 15', time, 'T_{Env}')

$T_{w,In} =$ **ConvertTemp** (C, K, $T_{w,Int}$)

$\rho_w = \rho(Fluid_{o\$}, T = T_{amb}, P = P_{atm})$

$Cp_w =$ **Cp** $(Fluid_{o\$}, T = T_{amb}, P = P_{atm}) \cdot \left| 1000 \cdot \frac{J/kg\text{–}K}{kJ/kg\text{–}K} \right|$

$\dot{V}_w = \dot{v}_{w,Int} \cdot \left| 0.0000630902 \cdot \frac{m3/s}{gpm} \right|$

$\dot{V}_w = \frac{\dot{m}_{w,Int}}{\rho_w}$ *Volume Flow rate in single PEX/Copper tube*

$V_{i,air} = 0.25$ [m/s] *Indoor Air Velocity from comfort conditions*

$IDT_{SP} = 70$ [F] *Indoor Air Temperature - Assumed Constant*

$RH_{space} = 0.6$ *Indoor Relative Humidity*

$T_{supply} = 55$ [F] *Supply Air Temperature from AHU*

$ACH = 10$ *Air Change per hour*

$P_{atm} = 1 \cdot \left| 101.325 \cdot \frac{kPa}{atm} \right|$ *Air Pressure Inside as well in Outside Air*

$T_{amb} = 25$ [C] *Ambient Temperature*

$T_{OD} = T_{ID}$ *Outside Temperature*

Convert T in Kelvin

$T_{ID} =$ **ConvertTemp** (C, K, $T_{Room,Air}$)

$T_{sink} =$ **ConvertTemp** (F, K, T_{supply})

$T_{env} =$ **ConvertTemp** (C, K, T_{amb})

$Q_{Internal} = 0.2$ [kW] *Internal Load*

$Fluid_{i\$} =$ 'AIR_{HA}'

$\rho_{air} = \rho(Fluid_{i\$}, T = T_{amb}, P = P_{atm})$

$Cp_{air} =$ **Cp** $(Fluid_{i\$}, T = T_{amb}, P = P_{atm})$

Properties of Layers

Gypsum Panel

$H_{gp} = 5 \cdot \left| 0.3048 \cdot \frac{m}{ft} \right|$ *Height*

$W_{gp} = 4 \cdot \left| 0.3048 \cdot \frac{m}{ft} \right|$ *Width*

$t_{gp} = 1/4 \cdot 1 \cdot \left| 0.0254 \cdot \frac{m}{inch} \right|$ *Thckness*

Based on ASHRAE Fundamentals - 2017

$C_{gp} = 950$ [J/kg-K] *Specific Heat*

$\rho_{gp} = 668$ [kg/m3] *Density*

$k_{gp} = 0.17$ [W/m-K] *Thermal Conductivity ENgineering ToolBox*

$\varepsilon_{gp} = 0.903$ *Emissivity on a smooth plate*

$RelRough_{gp} = 0.02$ **Assumption**

Support Panel

$H_{sp} = H_{gp}$

$W_{sp} = W_{gp}$ *Heght and width same as gypsum panel*

$t_{sp} = 0.13 \cdot 1 \cdot \left| 0.0254 \cdot \frac{m}{inch} \right|$ *Thickness*

$material\$_{sp} = 'Aluminum_{6061}'$

$\rho_{sp} = \rho(material\$_{sp}, T = T_{amb})$

$C_{sp} = Cp(material\$_{sp}, T = T_{amb}) \cdot \left| 1000 \cdot \frac{J/kg-K}{kJ/kg-K} \right|$

$k_{sp} = k(material\$_{sp}, T = T_{amb})$

$AbsRough_{sp} = 0.002 \cdot 10^{-3} \cdot 1$ [m]

Aluminium Panel

$H_{al} = 48 \cdot \left| 0.0254 \cdot \frac{m}{inch} \right|$

$W_{al} = 54 \cdot \left| 0.0254 \cdot \frac{m}{inch} \right|$ *Heght and width same as gypsum panel*

$t_{al} = 0.13 \cdot 1 \cdot \left| 0.0254 \cdot \frac{m}{inch} \right|$ *Thickness*

$Alumin\$ = 'Aluminum_{6061}'$

$\rho_{al} = \rho(Alumin\$, T = T_{amb})$

$C_{al} = Cp(Alumin\$, T = T_{amb}) \cdot \left| 1000 \cdot \frac{J/kg-K}{kJ/kg-K} \right|$

$k_{al} = k(Alumin\$, T = T_{amb})$

$AbsRough_{al} = 0.002 \cdot 10^{-3} \cdot 1$ [m] *Absolute Roughness: https://www.engineeringtoolbox.com/surface-roughness ventilation-ducts-d_209.html*

Heat Trasnfer Panel / Spreader

$t_{pn} = 0.05 \cdot \left| 0.0254 \cdot \frac{m}{in} \right|$ *Thickness*

$W_{pn} = 4 \cdot \left| 0.0254 \cdot \frac{m}{in} \right|$ *Width*

$H_{pn} = 48 \cdot \left| 0.0254 \cdot \frac{m}{in} \right|$ *Length*

$material_{pn\$} =$ 'Aluminum' *Material*

$k_{pn} = k(material_{pn\$}, T = T_{amb})$

$\rho_{pn} = \rho(material_{pn\$}, T = T_{amb})$

$C_{pn} = Cp(material_{pn\$}, T = T_{amb}) \cdot \left| 1000 \cdot \frac{J/kg-K}{kJ/kg-K} \right|$

$A_{pn} = 4 \cdot 48 \cdot \left| 0.00064516 \cdot \frac{m^2}{in^2} \right|$ *Surface area of heat spreader*

COPPER Tube

Size: 3/8"

Tube Material Thermal Conductivity

$ID_{tb} = 0.35 \cdot \left| 0.0254 \cdot \frac{m}{in} \right|$ *Tube Internal Diameter*

$OD_{tb} = 0.5 \cdot \left| 0.0254 \cdot \frac{m}{in} \right|$ *Tube Outer Diamater*

$L_{tb} = 48 \cdot \left| 0.0254 \cdot \frac{m}{in} \right|$ *Length of tube in each pass*

$AbsRough_{tb} = 0.0015 \cdot \left| 0.001 \cdot \frac{m}{mm} \right|$

$RelRough_{tb} = \frac{AbsRough_{tb}}{ID_{tb}}$

$W = 8 \cdot \left| 0.0254 \cdot \frac{m}{in} \right|$ *Spacing between two tube passes*

Panel Frame

$Edge_{Width} = 4 \cdot \left| 0.0254 \cdot \frac{m}{inch} \right|$

$Edge_{Height} = 59 \cdot \left| 0.0254 \cdot \frac{m}{inch} \right|$

$Edge_{Base} = 48 \cdot \left| 0.0254 \cdot \frac{m}{inch} \right|$

$Edge_{SArea} = 2 \cdot (Edge_{Width} \cdot Edge_{Height} + Edge_{Width} \cdot Edge_{Base})$ *Surface Area of Frame*

Insulation

Poured foam in place

$\rho_{ins} = 30$ [kg/m3] *Density of Insulation material*

$k_{ins} = 0.0245$ [W/m-K] *Thermal conductivity of insulation material*

$t_{ins} = 2.5 \cdot \left| 0.0254 \cdot \frac{m}{in} \right|$ *Thickess of Insulation*

$C_{ins} = 1000$ [J/kg-K]

Contact Resistances

$R_{sp,gp} = 0.02$ [K-m2/W] *Contact resistance between Gypsum and Support Panel*

$R_{al,sp} = 0.016$ [K-m2/W] *Contact resistance between Support and Aluminum Panel*

$R_{pn,Ins} = 0.18$ [K-m2/W] *Air Gap-Thermal Resistance between Heat Spreader and Insulation*

$A = H_{gp} \cdot W_{gp}$ *Surface area of each layer*

*Thermal resistances in each layer=Thickness of layer/(thermal conductivity*Surface area) K/W*

$R_{gp} = \frac{t_{gp}}{k_{gp} \cdot A}$ *Thermal resistance in gypsum panel*

$R_{sp} = \frac{t_{sp}}{k_{sp} \cdot A}$ *Thermal resistance in support panel*

$R_{al} = \frac{t_{al}}{k_{al} \cdot A}$ *Thermal resistance in aluminum panel*

$R_{pn} = \frac{t_{pn}}{k_{pn} \cdot A}$ *Thermal resistance in heat spreader*

Thermal resistance in water-tube wall

$R_{ins} = \frac{t_{ins}}{k_{ins} \cdot A}$ *Thermal resistance in insulation*

Resistances

$R_{contact} = \frac{R_{al,sp} + R_{sp,gp}}{A}$ *Total Contact Resisitance*

$R_{f,total} = R_{al} + R_{sp} + R_{gp}$ *Total Thermal Resistance-Front-AL to GP*

$R_{b,total} = \frac{R_{pn,ins}}{A_{pn} \cdot 6} + R_{ins} + \frac{R_{air,ins}}{A}$ *Total Thermal Resistance-Back-PN to INS*

Factor for tuning thermal capacitance to match experimental transients

Capacitances [J/K]

$Cap_{al} = \rho_{al} \cdot A \cdot t_{al} \cdot C_{al} \cdot \lambda_1$ *Capacitance-Aluminum Base Panel Layer*

$Cap_{sp} = \rho_{sp} \cdot A \cdot t_{sp} \cdot C_{sp} \cdot \lambda_2$ *Capacitance-Support Panel Layer*

$Cap_{gp} = \rho_{gp} \cdot A \cdot t_{gp} \cdot C_{gp} \cdot \lambda_3$ *Capacitance-Gypsum Panel Layer*

Ignored

Capacitance-Heat Spreader Layer-Neglected

Insulation Surface to outdoor resistance

Call $fc_{plate,vertical}$ ($Fluid_{i\$}$, $T_{surface,C}$, $T_{Room,Air}$, 101.3 [kPa], 1.542 [m] : h_{ins})

$R_{air,ins} = \frac{1}{h_{ins}}$ *Thermal resistance-Insulation-Outdoor Air*

Overall loss coefficients

$U_F = \frac{1}{R_{f,total} + R_{contact}}$ *Front Overall loss coefficient*

$U_B = \frac{1}{R_{b,total}}$ *Back Overall loss coefficient*

Fin Efficiency Factor

$m = \sqrt{\frac{U_F}{k_{al} \cdot t_{al}}}$

$F = \tanh\left[\frac{m \cdot \left[\frac{W - OD_{tb}}{2}\right]}{m \cdot \left[\frac{W - OD_{tb}}{2}\right]}\right]$ *Fin efficiency factor*

Heat Balance

$n_t = 6$ *No. of Tubes*

$Eq_L = L_{tb} \cdot n_t$ *Tube Equivalent length*

Call $pipeflow_{local}$ ($Fluid_{o\$}$, T_{amb}, P_{atm}, $\dot{m}_{w,Int}$, ID_{tb}, Eq_L, $RelRough_{tb}$: h_{fi}) *To calculate water-tube wall convective HTC*

Call $fc_{plate,vertical}$ ($Fluid_{i\$}$, $T_{surface,C}$, $T_{Room,Air}$, 101.3 [kPa], 1.542 [m] : h_c)

$h_r = \varepsilon_{gp} \cdot 5.670E{-}08\ [W/m^2\text{-}K^4] \cdot (T_{surface}^{\ 2} + T_{ID}^{\ 2}) \cdot (T_{surface} + T_{ID})$ *Radiative heat transfer coefficient Gypsum Indoor Air*

$h_i = h_c + h_r$ *Net HTC (Convective+Radiative) between Panel Surface-Indoor Air*

$R_{air} = \frac{1}{h_i \cdot A}$ *Thermal resistance-Gypsum-Indoor Air*

$\dot{Q}_{loss} = F \cdot U_B \cdot (Temp_{pn} - T_{OD})$ *Heat Lost to Outoor*

$$\dot{Q}_{in} = Eq_L \cdot \left[\frac{T_{w,in} - Temp_{pn}}{\frac{1}{C_b} + \frac{1}{h_{fi} \cdot \pi \cdot ID_{tb}}} \right]$$ *Heat In from water to heat spreader*

$$\dot{Q}_{front} = \frac{Temp_{pn} - Temp_{al}}{\frac{R_{al}}{2}}$$

$$\dot{Q}_{edge} = h_{Edge} \cdot Edge_{SArea} \cdot (Temp_{sp} - T_{ID})$$ *Heat to Surface = Heat in-Heat Loss*

Heat Spreader Node Energy Balance

$$\dot{Q}_{in} = \dot{Q}_{front} + \dot{Q}_{loss}$$

Aluminum Node Energy Balance

$$\dot{Q}_{front} = Cap_{al} \cdot dTemp/dt_{al} \cdot \left| 0.016666667 \cdot \frac{K/s}{K/min} \right| + \frac{Temp_{al} - Temp_{sp}}{\frac{R_{al}}{2} + \frac{R_{sp}}{2} + \frac{R_{al,sp}}{A}}$$

$$Temp_{al} = T_{ID} + \int_{0\ [min]}^{EndTime} (dTemp/dt_{al})\ d\ time$$

Support Panel Node Energy Balance

$$\frac{Temp_{al} - Temp_{sp}}{\frac{R_{al}}{2} + \frac{R_{sp}}{2} + \frac{R_{al,sp}}{A}} = Cap_{sp} \cdot dTemp/dt_{sp} \cdot \left| 0.016666667 \cdot \frac{K/s}{K/min} \right| + \frac{Temp_{sp} - Temp_{gp}}{\frac{R_{sp}}{2} + \frac{R_{gp}}{2} + \frac{R_{sp,gp}}{A}} + h_{Edge} \cdot Edge_{SArea} \cdot (Temp_{sp} - T_{ID})$$

$$Temp_{sp} = T_{ID} + \int_{0\ [min]}^{EndTime} (dTemp/dt_{sp})\ d\ time$$

Gypsum Panel Energy Balance

$$\frac{Temp_{sp} - Temp_{gp}}{\frac{R_{sp}}{2} + \frac{R_{gp}}{2} + \frac{R_{sp,gp}}{A}} = Cap_{gp} \cdot dTemp/dt_{gp} \cdot \left| 0.016666667 \cdot \frac{K/s}{K/min} \right| + \frac{Temp_{gp} - T_{ID}}{\frac{R_{gp}}{2} + R_{air}}$$

$$Temp_{gp} = T_{ID} + \int_{0\ [min]}^{EndTime} (dTemp/dt_{gp})\ d\ time$$

$$Temp_{gp} = T_{surface}$$

$$T_{surface,C} = \mathbf{ConvertTemp}(K, C, T_{surface})$$

$$Temp_{al,C} = \mathbf{ConvertTemp}(K, C, Temp_{al})$$

$$\dot{Q}_{loss} = \frac{Temp_{pn} - Temp_{ins}}{\frac{R_{ins}}{2} + \frac{R_{pn,ins}}{A}}$$ *To calculate Insulation Node Temperature*

$$\dot{Q}_{in} = \dot{m}_{w,int} \cdot Cp_w \cdot (T_{w,out} - T_{w,in})$$ *To calculate Water Outlet Temperature*

$$\Delta T = T_{w,out} - T_{w,in}$$

Water inlet-outlet temperature

Call **optimizetr** ($Temp_{al,C}$, $T_{surface,C}$, time : $Error_{TR}$)

SOLUTION

Unit Settings: SI C kPa kJ mass deg

Minimization of Error_TR(Lambda_1,Lambda_2,Lambda_3) = 0 296 iterations: Genetic method (16 individuals, 16 generations)

A = 1.858 [m^2]
$AbsRough_{sp}$ = 0.000002 [m]
ACH = 10 [-]
A_{pn} = 0.1239 [m^2]
Cap_{gp} = 8985 [J/K]
Cp_{air} = 1.006 [kJ/Kg-K]
C_{al} = 951.1 [J/Kg-K]
C_{gp} = 950 [J/kg-K]
C_{pn} = 900.9 [J/kg-K]
ΔT = 0.8125 [K]
$dTemp/dt_{gp}$ = 0.002431 [K/min]
$Edge_{Base}$ = 1.219 [m]
$Edge_{SArea}$ = 0.5523 [m^2]
$EndTime$ = 139 [min]
Eq_L = 7.315 [m]
F = 0.7616 [-]
Fluido$ = 'WATER'
h_c = 3.07 [W/m^2-K]
h_n = 5150 [W/m^2-K]
h_i = 8.653 [W/m^2-K]
H_{pn} = 1.219 [m]
H_{sp} = 1.524 [m]
ID_{tb} = 0.00889 [m]
k_{gp} = 0.17 [W/m-K]
k_{pn} = 234.9 [W/m-K]
λ_1 = 1.117
λ_3 = 1.194

$AbsRough_{al}$ = 0.000002 [m]
$AbsRough_{tb}$ = 0.0000015 [m]
Alumin$ = 'Aluminum_6061'
Cap_{al} = 17599 [J/K]
Cap_{sp} = 18385 [J/K]
Cp_w = 4181 [J/Kg-K]
C_b = 4.18 [W/m-K]
C_{ins} = 1000 [J/kg-K]
C_{sp} = 951.1 [J/kg-K]
$dTemp/dt_{al}$ = -0.008049 [K/min]
$dTemp/dt_{sp}$ = 0.000008408 [K/min]
$Edge_{Height}$ = 1.499 [m]
$Edge_{Width}$ = 0.1016 [m]
ε_{gp} = 0.903 [-]
$Error_{TR}$ = 0 [C]
Fluidi$ = 'AIR_HA'
H_{al} = 1.219 [m]
h_{Edge} = 9.86 [W/m^2-K]
H_{gp} = 1.524 [m]
h_{ins} = 3.07 [W/m^2-K]
h_r = 5.584 [W/m^2-K]
IDT_{SP} = 70 [F]
k_{al} = 155.9 [W/m-K]
k_{ins} = 0.0245 [W/m-K]
k_{sp} = 155.9 [W/m-K]
λ_2 = 1.167
L_{tb} = 1.219 [m]

APPENDIX C. HBIL FACILITY PIPING SECTIONS PRESSURE DROP RESULTS

HBIL Fittings Pressure Drop Calculations

Parametric Table: P-FLoor

	Part$	Flow [GPM]	Length [ft]	$PLoss_{Factor}$ [fth2o/ft]	Dia [inch]	$PD_{Pipe,EqL}$ [psi]	$PD_{Pipe,Darcy}$ [psi]
Run 1	Main Supply Horizontal	28	5	1.6	2	*0.03468*	*0.03942*
Run 2	Main Supply Vertical-UP	28	12	1.6	2	*0.08324*	*0.0946*
Run 3	Main Supply Top Horizontal	28	40	1.6	2	*0.2775*	*0.3153*
Run 4	Floor Supply Vertical-DOWN	7	12	9.64	1	*0.5015*	*0.2243*
Run 5	Floor Supply Horizontal	7	12	6.64	1	*0.3454*	*0.2243*
Run 6	Supply 1	5	3.5	5.17	1	*0.07845*	*0.03642*
Run 7	Supply 2	3	3.5	2.01	1	*0.0305*	*0.01507*
Run 8	Supply 3	1	3.5	0.26	1	*0.003945*	*0.00233*
Run 9	Supply 4	1	5	4.79	0.5	*0.1038*	*0.08604*
Run 10	Panel Piping	1	60	2.31	0.5	*0.6009*	*1.032*
Run 11	Return 1	1	5	4.79	0.5	*0.1038*	*0.08604*
Run 12	Return 2	6	3.5	7.25	1	*0.11*	*0.05*
Run 13	Return 3	7	18	9.64	1	*0.7523*	*0.3365*
Run 14	Floor Return Horizontal	7	12	9.64	1	*0.5015*	*0.2243*
Run 15	Floor Return Vertical	7	10	9.64	1	*0.4179*	*0.1869*
Run 16	Main Return Top Horizontal	28	40	1.6	2	*0.2775*	*0.3153*
Run 17	Main Return Vertical-DOWN	28	10	1.6	2	*0.06936*	*0.07883*
Run 18	Main Return Horizontal	28	5	1.6	2	*0.03468*	*0.03942*
Sum		**221**	**260**	**81.38**	**22.5**	**4.327**	**3.388**

HBIL Fittings Pressure Drop Calculations

Parametric Table: F-Floor

	Part$	Flow [GPM]	Qty [-]	Dia [inch]	EL [ft]	$PD_{fittings,EQ}$
Run 1	Tee Through 2"	28	2	2	4.3	*0.4763*
Run 2	Reducing Adapter 2" x 1"	28	2	2	8	*0.8862*
Run 3	Flow Meter	28	1	1	1.5	*1.329*
Run 4	Gate Valve 2"	28	1	2	1.5	*0.08308*
Run 5	Union 2"	28	1	2	2	*0.1108*
Run 6	Elbows 2"	28	3	2	5.7	*0.9471*
Run 7	Tee Through 2"	21	2	2	4.3	*0.2679*
Run 8	Tee Through 2"	14	2	2	4.3	*0.1191*
Run 9	Tee Through 2"	7	2	2	4.3	*0.02977*
Run 10	Tee Branch 2" x 1"	7	1	1	12	*0.6647*
Run 11	Adapter PVC to PEX	7	1	1	1.2	*0.06647*
Run 12	PEX adapter 1"	7	1	1	1.2	*0.06647*
Run 13	Isolation Valves	7	1	1	4.3	*0.2382*
Run 14	Elbow 1"	7	2	1	11.5	*1.274*
Run 15	Reducing Tee 1x1x0.5"	7	1	1	1.2	*0.06647*
Run 16	Reducing Tee 1x1x0.5"	6	1	1	1.2	*0.04883*
Run 17	Reducing Tee 1x1x0.5"	5	1	1	1.2	*0.03391*
Run 18	Reducing Tee 1x1x0.5"	4	1	1	1.2	*0.0217*
Run 19	Reducing Tee 1x1x0.5"	3	1	1	1.2	*0.01221*
Run 20	Reducing Tee 1x0.5x1"-Branch	1	1	0.5	12.7	*0.2297*
Run 21	Reducing Tee 1x0.5x1"-Branch	1	1	0.5	12.7	*0.2297*
Run 22	Reducing Tee 1x1x0.5"	6	1	1	1.2	*0.04883*
Run 23	Reducing Tee 1x1x0.5"-Branch	7	1	1	6.5	*0.36*
Run 24	3-Way Valves (Mixing and Diverting)	1	2	0.5	262	*9.477*
Run 25	Elbow 0.5"	1	10	0.5	10.4	*1.881*
Run 26	Reducing Tee 1x0.5x1"-Branch	7	1	1	6.5	*0.36*
Run 27	Elbow 1"	7	2	1	11.5	*1.274*
Run 28	Isolation Valve	7	1	1	1.2	*0.06647*
Run 29	PEX Adapter	7	1	1	1.2	*0.06647*
Run 30	Adapter PVC to PEX	7	1	1	1.2	*0.06647*
Run 31	Tee Branch 1" x 2"	7	1	1	12	*0.6647*
Run 32	Elbows 2"	28	3	2	5.7	*0.9471*
Run 33	Union 2"	28	1	2	2	*0.1108*
Run 34	Gate Valve 2'	28	1	2	1.5	*0.08308*
Run 35	Reducing Adapter 2" x 1.5"	28	2	2	4.5	*0.4985*
Run 36	Tee Through 2"	28	2	2	4.3	*0.4763*
Sum		**469**	**59**	**47**	**429.2**	**23.58**

REFERENCES

Abdelmageed, S., & Zayed, T. (2020). A study of literature in modular integrated construction - Critical review and future directions. In *Journal of Cleaner Production* (Vol. 277). Elsevier Ltd. https://doi.org/10.1016/j.jclepro.2020.124044

Badran, A. A., Mustafa, M. F., Dawood, W. K., & Ghazzawi, Z. K. (2008). On the measurement of bond conductance in solar collector absorber plate. *Energy Conversion and Management*, *49*(11), 3305–3310. https://doi.org/10.1016/j.enconman.2008.01.041

Bergman, T. L., DeWitt, D. P., Incropera, F., & Lavine, A. S. (2011). Fundamentals of Heat and Mass Transfer. In *Publisher John Wiley & Sons* (Vol. 997).

Bhardwaj, A., Jones, S. Z., Kalantar, N., Pei, Z., Vickers, J., Wangler, T., Zavattieri, P., & Zou, N. (2019). Additive Manufacturing Processes for Infrastructure Construction: A Review. *Journal of Manufacturing Science and Engineering*, *141*(9). https://doi.org/10.1115/1.4044106

Bitter, R., & Nawrocki, M. (2006). *LabVIEW: Advanced programming techniques*. Crc. Press.

Brager, G., & Arens, E. (2015). Creating high performance buildings: Lower energy, better comfort. *AIP Conference Proceedings*, *1652*, 58–69. https://doi.org/10.1063/1.4916169

Copper Development Association Inc. (2020). *Copper Tube Handbook Industry Standard Guide for the Design and Installation of Copper Piping Systems*. www.copper.org

Dawe, M. (2019). *UC Berkeley Indoor Environmental Quality (IEQ) Title Field evaluation of occupant satisfaction and energy performance in eight LEED-certified buildings using radiant systems Publication Date*.

Delgado Camacho, D., Clayton, P., O'Brien, W. J., Seepersad, C., Juenger, M., Ferron, R., & Salamone, S. (2018). Applications of additive manufacturing in the construction industry – A forward-looking review. *Automation in Construction*, *89*, 110–119. https://doi.org/10.1016/j.autcon.2017.12.031

Deru, M., Field, K., Studer, D., Benne, K., Griffith, B., Deru, M., Studer, D., Griffith, B., Torcellini, P., Liu, B., Halverson, M., Winiarski, D., Yazdanian, M., & Crawley, J. (2011). Models of the National Building Stock Models of the National Building Stock Part of the Environmental Design Commons, Natural Resources and Conservation Commons, and the Sustainability Commons Repository Citation Repository Citation. In *U.S. Department of Energy*

Commercial Reference Building Models of the National Building Stock. https://digitalscholarship.unlv.edu/renew_pubshttps://digitalscholarship.unlv.edu/renew_pubs/44

ENERGY POLICY ACT OF 2005. (2005).

Engineering Toolbox. (2003). *Roughness & Surface Coefficients*. https://www.engineeringtoolbox.com/surface-roughness-ventilation-ducts-d_209.html

Engineering ToolBox. (2004). *PVC - Friction Loss in Fittings and Equivalent Length*. https://www.engineeringtoolbox.com/pvc-pipes-equivalent-length-fittings-d_801.html

Engineering ToolBox (2004). (2004). *PVC Pipes - Friction Loss and Flow Velocities Schedule 40*. Online. https://www.engineeringtoolbox.com/pvc-pipes-friction-loss-d_802.html

Esrafilian-Najafabadi, M., & Haghighat, F. (2021). Occupancy-based HVAC control systems in buildings: A state-of-the-art review. In *Building and Environment* (Vol. 197). Elsevier Ltd. https://doi.org/10.1016/j.buildenv.2021.107810

Fabrizio, E., Corgnati, S. P., Causone, F., & Filippi, M. (2012). Numerical comparison between energy and comfort performances of radiant heating and cooling systems versus air systems. *HVAC and R Research*, *18*(4), 692–708. https://doi.org/10.1080/10789669.2011.578700

Ferdous, W., Bai, Y., Ngo, T. D., Manalo, A., & Mendis, P. (2019). New advancements, challenges and opportunities of multi-storey modular buildings – A state-of-the-art review. In *Engineering Structures* (Vol. 183, pp. 883–893). Elsevier Ltd. https://doi.org/10.1016/j.engstruct.2019.01.061

Godithi, S. B., Sachdeva, E., Garg, V., Brown, R., Kohler, C., & Rawal, R. (2019). A review of advances for thermal and visual comfort controls in personal environmental control (PEC) systems. In *Intelligent Buildings International* (Vol. 11, Issue 2, pp. 75–104). Taylor and Francis Ltd. https://doi.org/10.1080/17508975.2018.1543179

Goldstein, K., & Novoselac, A. (2010). Convective Heat Transfer in Rooms with Ceiling Slot Diffusers (RP-1416). *HVAC&R Research*, *16*(5), 629–655. https://doi.org/10.1080/10789669.2010.10390925

Halawa, E., van Hoof, J., & Soebarto, V. (2014). The impacts of the thermal radiation field on thermal comfort, energy consumption and control - A critical overview. In *Renewable and Sustainable Energy Reviews* (Vol. 37, pp. 907–918). Elsevier Ltd. https://doi.org/10.1016/j.rser.2014.05.040

Higgins, C., & Carbonnier, K. (2017). *UC Berkeley HVAC Systems Title Energy Performance of Commercial Buildings with Radiant Heating and Cooling Permalink*. https://escholarship.org/uc/item/34f0h35q

Hu, M. (2021). Smart Technologies and Design For Healthy Built Environments. In *Smart Technologies and Design For Healthy Built Environments*. Springer International Publishing. https://doi.org/10.1007/978-3-030-51292-7

Kalogirou, S. A. (2009). Solar Energy Collectors. In *Solar Energy Engineering* (pp. 121–217). Elsevier. https://doi.org/10.1016/B978-0-12-374501-9.00003-0

Karmann, C., Schiavon, S., & Bauman, F. (2017). Thermal comfort in buildings using radiant vs. all-air systems: A critical literature review. *Building and Environment*, *111*, 123–131. https://doi.org/10.1016/j.buildenv.2016.10.020

Kim, J., Bauman, F., Raftery, P., Arens, E., Zhang, H., Fierro, G., Andersen, M., & Culler, D. (2019). Occupant comfort and behavior: High-resolution data from a 6-month field study of personal comfort systems with 37 real office workers. *Building and Environment*, *148*, 348–360. https://doi.org/10.1016/j.buildenv.2018.11.012

Klein, S. A. (2021). *EES-Engineering Equation Solver (Academic Professional V-10.834-3D [2020-05-27])*.

Koca, A., & Cetin, G. (2017). Experimental investigation on the heat transfer coefficients of radiant heating systems: Wall, ceiling and wall-ceiling integration. *Energy and Buildings*, *148*, 311–326. https://doi.org/10.1016/j.enbuild.2017.05.027

Lassen, N., Hegli, T., Dokka, T. H., Løvold, T., Edwards, K., Goia, F., & Andresen, I. (2021). Enabling holistic design for high energy efficient office buildings through the use of subjective occupant feedback. *Sustainable Cities and Society*, *69*. https://doi.org/10.1016/j.scs.2021.102867

"LEARN London Metroplitan University" "School of Planning and Architecture" "TVB School of Habitat Studies" "National Kapodestrian University of Athens." (2004). *Comfortable Low Energy Architecture*. https://www.new-learn.info/packages/clear/thermal/buildings/building_fabric/elements/cavities_and_air_spaces.html

Li, Z., Zhang, D., & Li, C. (2021). Experimental evaluation of indoor thermal environment with modularity radiant heating in low energy buildings. *International Journal of Refrigeration*, *123*, 159–168. https://doi.org/10.1016/j.ijrefrig.2020.11.018

Nellis, G., & Klein Sanford. (2009). *Heat Transfer*. Cambridge University Press.

Nellis, Gregory., & Klein, S. A. (2009). *Heat transfer*. Cambridge University Press. https://doi.org/doi:10.1017/CBO9780511841606

Rawal, R., Schweiker, M., Kazanci, O. B., Vardhan, V., Jin, Q., & Duanmu, L. (2020). Personal comfort systems: A review on comfort, energy, and economics. *Energy and Buildings*, *214*. https://doi.org/10.1016/j.enbuild.2020.109858

Rhee, K. N., & Kim, K. W. (2015). A 50 year review of basic and applied research in radiant heating and cooling systems for the built environment. *Building and Environment*, *91*, 166–190. https://doi.org/10.1016/j.buildenv.2015.03.040

Rhee, K. N., Olesen, B. W., & Kim, K. W. (2017). Ten questions about radiant heating and cooling systems. *Building and Environment*, *112*, 367–381. https://doi.org/10.1016/j.buildenv.2016.11.030

Shashi Menon, E. (2015). Fluid Flow in Pipes. In *Transmission Pipeline Calculations and Simulations Manual* (pp. 149–234). Elsevier. https://doi.org/10.1016/b978-1-85617-830-3.00005-5

U.N. Environment Program Global Alliance for Buildings and Construction. (2020). *2020 GLOBAL STATUS REPORT FOR BUILDINGS AND CONSTRUCTION*. https://globalabc.org/sites/default/files/inline-files/2020%20Buildings%20GSR_FULL%20REPORT.pdf

Uponor Inc. (2020). *Fitting equivalent length and Pressure loss charts l 1 Fitting equivalent length*. uponorpro.com

U.S. Energy Information Administration. (2020). *The Annual Energy Outlook explores long-term energy trends in the United States*. www.eia.gov/aeo

U.S. Energy Information Administration. (2021). *Monthly Energy Review – November 2021*. https://www.eia.gov/energyexplained/use-of-energy/

Zhang, C., Pomianowski, M., Heiselberg, P. K., & Yu, T. (2020). A review of integrated radiant heating/cooling with ventilation systems- Thermal comfort and indoor air quality. In *Energy and Buildings* (Vol. 223). Elsevier Ltd. https://doi.org/10.1016/j.enbuild.2020.110094

PUBLICATIONS

"Design and Development of a Human Building Interaction Laboratory"

6th International High Performance Buildings Conference - Purdue202One Conferences, Purdue University. https://docs.lib.purdue.edu/cgi/viewcontent.cgi?article=1361&context=ihpbc